Search for Exotic Processes in Events with Large Missing Transverse Momentum in ZEUS at HERA

Dissertation
zu Erlangung des Doktorgrades
des Fachbereichs Physik
der Universitaet Hamburg

vorgelegt von
Julia Furletova
aus Dubna

Hamburg
2004

Gutachter der Dissertation:	Prof. Dr. P. Schleper Prof. Dr. R. Klanner
Gutachterin/Gutachter der Disputation:	Prof. Dr. B. Naroska Prof. Dr. R.-D. Heuer
Datum der Disputation:	1 December 2004
Vorsitzender des Prüfungsausschusses:	Prof. Dr. G. Heinzelmann
Dekan des Fachbereichs Physik und Vorsitzender des Promotionsausschusses:	Prof. Dr. G. Huber

Abstract

This thesis presents a search for lepton-quark resonance events produced in ep collisions, which decay into $\nu + jet(s)$. A total of 65 pb^{-1} of e^+p and 16.7 pb^{-1} of e^-p data, collected by the ZEUS experiment at the HERA collider with center-of-mass energy $\sqrt{s} = 318$ GeV, has been analyzed. No significant signal was found using a standard cut based event selection procedure. In order to improve both leptoquark signal efficiency and background rejection a Neural Network selection was additionally implemented. Again no evidence for resonance production was found and limits have been derived on leptoquark production cross-sections and coupling constants, within the framework of the Buchmüller-Rückl-Wyler model, which extend result previously published at LEP, TEVATRON and HERA. Additionally a search for deviations between data and the Standard Model using a generalized missing transverse momentum signature have been performed. Again no signal was found. The authors contribution to the C5 detector, developed and installed during the HERA-II upgrade is described.

Zusammenfassung

Diese Arbeit präsentiert eine Suche nach Ereignissen einer Lepton-Quark Resonanz, die bei Elektron(Positron)-Proton Kollisionen erzeugt werden und in ein Neutrino und einen oder mehrere Jets zerfallen. Die Daten wurden mit dem ZEUS Detektor an dem ep Speicherring HERA bei einer Schwerpunktsenergie von $\sqrt{s} = 318$ GeV genommen. Die integrierte Luminosität betrug 65 pb^{-1} für e^+p und 16.7 pb $^{-1}$ für e-p Kollisionen. Nach einer Ereignisselektion wurde kein signifikantes Signal gefunden. Zur Verbesserung der Nachweiswahrscheinlichkeit für ein Leptoquark Signal und zur Reduktion des Untergrunds wurde zusätzlich ein auf einem neutralen Netzwerk basierender Algorithmus verwendet. Da wieder keine Evidenz für eine Resonanz gefunden wurde, wurden Grenzen für den Leptoquarkerzeugungs Wirkungsquerschnitt und Kopplungskonstanten nach dem BRW Modell bestimmt, die über die veröffentlichten Ergebnisse von LEP, TEVATRON und HERA hinausgehen. Ausserdem wurde eine Suche nach Abweichungen vom Standard Modell mit fehlendem transversalen Impuls durchgeführt. Es wurde wieder kein Signal gefunden. Der Beitrag der Autorin zur Entwicklung und zum Betrieb des C5 Detektors für den HERA II Run wird beschrieben.

"Everything is allowed that is not prohibited" L.B. Okun

Contents

1 Introduction **1**

2 Theory **3**

2.1 The Standard Model . . . 3

2.2 Deep inelastic electron-proton scattering . . . 5

2.3 *ep* background processes . . . 7

2.3.1 Neutral current and charged current DIS . . . 7

2.3.2 Photoproduction . . . 9

2.4 Theories beyond the Standard Model . . . 12

2.5 Leptoquark searches . . . 15

2.5.1 Buchmüller-Rückl-Wyler model . . . 15

2.5.2 Leptoquarks in *ep* collisions . . . 18

2.5.3 Experimental limits on leptoquarks production . . . 19

2.6 Missing transverse momentum as a signature for new physics . . . 28

2.6.1 Excited fermions . . . 28

2.6.2 Selectrons and Squarks . . . 29

2.6.3 Search for R-parity violating squarks . . . 30

2.6.4 Other exotic processes with missing transverse momentum in the final states. . . . 32

3 HERA and ZEUS **33**

3.1 The Hadron-Electron Ring Accelerator . . . 33

3.2 ZEUS detector . . . 37

3.2.1 The central tracking detector . . . 39

3.2.2 The uranium calorimeter(CAL) . . . 41

3.2.3 C5 detector . . . 42

3.2.4 The luminosity monitor . . . 42

3.2.5 Trigger and data acquisition system . . . 43

4 C5 Detector **47**

4.1 Detector setup . . . 47

4.2 Data acquisition system . . . 50

4.3 C5 data flow . . . 51

4.4 C5 detector timing resolution . . . 53

4.5 Interaction point determination using C5 time information . . . 53

4.6 Electron and proton gated rate measurements . . . 60

4.7 LeCroy TDC measurements . . . 62

4.8 C5 as VETO for GFLT . . . 62

4.9 Background studies . . . 67

5 Monte Carlo Samples **71**

5.1 The event simulation, reconstruction and analysis chain . . . 71

5.2 Event simulation . . . 71

5.2.1 Signal Simulation . . . 72

5.2.2 Background Simulation . . . 72

6 Particle Identification and Kinematic Reconstruction 75

6.1 Reconstruction of Global Quantities . . . 75

6.2 Island and Jet Finding . . . 76

6.3 Reconstruction of Neutrino Parameters in Events Without Charged Leptons 77

6.4 Reconstruction of Kinematics . . . 77

6.5 Leptoquark Mass Reconstruction . . . 81

7 Leptoquark Selection 83

7.1 Preselection . . . 85

7.2 Non-ep backgrounds . . . 86

7.2.1 Beam-gas events . . . 86

7.2.2 Cosmic muons . . . 87

7.2.3 Halo muons . . . 87

7.3 Non-ep background rejection . . . 87

7.3.1 Halo and cosmic muon rejection . . . 88

7.3.2 HAC fractions . . . 88

7.3.3 Number of firing cells in calorimeter . . . 89

7.3.4 $P_T[-1ir]$ cuts . . . 89

7.3.5 Calorimeter Timing Cuts . . . 89

7.3.6 Selection with CTD tracks . . . 90

7.3.7 Visual Scan . . . 90

7.4 Leptoquark selection cuts . . . 90

7.4.1 Vertex requirement . . . 90

7.4.2 Kinematic region . . . 91

7.4.3 P_T cuts . . . 91

7.4.4 Jet cuts . . . 91

7.5 ep background rejection . . . 92

7.5.1 Pt_H/Et_H cut . . . 92

7.5.2 Neutral current rejection for events with $\gamma_h > 0.4$ . . . 92

7.6 Search results . . . 94

7.7 Systematic uncertainty of the mass spectrum . . . 110

8 Leptoquark Coupling Limit 113

8.1 Narrow width approximation method . . . 113

8.1.1 Determination of the search window size . . . 113

8.1.2 Optimization of $\cos(\theta^*)$ cut . . . 115

8.1.3 $\sigma \cdot \beta$ and λ limit at 95% CL . . . 116

8.2 Likelihood Method . . . 123

8.3 Frequentist Likelihood Method . . . 124

8.4 Results . . . 125

9 Artificial Neural Network Selection 131

9.1 Introduction . . . 131

9.1.1 Multivariate classifiers . . . 131

9.1.2 Artificial neural network . . . 132

9.2 Background rejection . . . 133

9.3 Search results . . . 135

10 Search for Other Exotics in events with P_T^{mis} 145

10.1 Selection Cuts and Background Rejection . . . 145

10.2 Results 146

11 HERA-II Operation **157**

12 Conclusion **161**

A C5 DAQ **163**

A.1 Position of C5 detector 163

A.2 C5: readout diagram 165

A.3 Read out system 166

A.3.1 VME single board computer 166

A.3.2 VME modules 166

A.3.3 DAQ configuration files and shared memory usage 175

A.3.4 DAQ "background" and "interactive" operation modes 177

A.3.5 How to recover after power failure 177

A.4 C5 data flow 177

A.5 Energy and current of HERA beam and HERA beam-pipe vacuum information 179

A.6 Useful programs 179

B Control Plots for e^-p Data **181**

C Event display **189**

List of Figures

2.1 Neutral and charged current deep inelastic scattering. 5

2.2 Kinematic (x, Q^2) region accessible at HERA compared to fixed target experiments. 7

2.3 Electron and quark scattering in the electron-quark center of mass frame. 8

2.4 The u and d valence quark and the gluon and sea distributions extracted from ZEUS and H1 NLO fits at $Q^2 = 10$ GeV^2. 9

2.5 The differential NC and CC cross sections as a function of Q^2 measured by the ZEUS and H1 collaborations for e^-p and e^+p scattering (from [4]). . 10

2.6 Feynman diagrams representing direct (left) and resolved (right) photoproduction. 11

2.7 (a) Measured dijet cross sections $d\sigma/dQ^2$ for $x_\gamma^{obs} \geq 0.75$ (▲) $d\sigma/dQ^2$ for $x_\gamma^{obs} < 0.75$ (▼) and $d\sigma/dQ^2$ for the entire x_γ^{obs} region (•). (b) Relative difference of the measured dijet cross section $d\sigma/dQ^2$ to the DISASTER++ ($\mu^2 = Q^2 + (E_T^{jet})^2$) and of Frixione and Ridolfi ($\mu^2 = (E_T^{jet})^2$) calculations. The hatched band shows the theoretical uncertainty of the calculations. . 11

2.8 The NWA production cross-sections for four kinds of scalar resonances in e^+p collision at $\sqrt{s} = 318$ GeV. 17

2.9 Diagrams of s-channel resonant production (left) and u-channel exchange of a leptoquark (right). 18

2.10 Feynman diagram showing proton decay via X-boson (leptoquark) exchange which does not conserve baryon and lepton number. 19

2.11 Feynman diagram showing s-channel production of a leptoquark in electron-photon scattering. The photon is radiated by one of the incoming beams and fluctuates into a hadronic object. 20

2.12 Feynman diagrams showing alternative single leptoquark production mechanisms, where the photon interaction is: (**a**) a "direct" interaction with the beam electron, or (**b**) absorbed by the leptoquark "emitted" by the other beam electron. 20

2.13 OPAL measurements of the 95% confidence level upper limits on the coupling constant λ for single production of the scalar and vector leptoquark states for branching fractions $\beta_e = 0.5$. 21

2.14 Feynman diagrams for leptoquark pair production at hadron colliders. The LQ pair is produced from the gluon, which is generated through quark-antiquark fusion (a) or through gluon-gluon fusion. 22

2.15 Schematic representation of the mechanism for producing single leptoquarks in proton–(anti)proton collisions. 22

2.16 TEVATRON 95% C.L. upper limits on the production cross-section as a function of leptoquark mass, for scalar (left) and vector (right) leptoquarks, and different theoretical predictions. The LQ is assumed to decay exclusively to νq. The theoretical predictions correspond to the production of leptoquarks of a single generation, while the experimental limit corresponds to the sum of contributions from leptoquarks of all three generations. . . . 23

2.17 Limits on the coupling $\lambda_{\rm lim}$ for an S_0^L LQ in the (M_{LQ}, λ) plane. The excluded region lies above the curves for H1,L3 and ZEUS and to the left of the line for D0. 24

2.18 (a) Q_e^2 distribution of the selected NC DIS candidate events for the data (•) and for standard NC DIS expectation (histogram); the arrows indicate the Q_e^2 values for data entries with $Q_e^2 > 15000$ GeV^2 and $M_e > 180$ GeV; (b) ratio of the observed and expected number of events as a function of Q_e^2. 26

2.19 a) Comparison of observed events (•) and SM expectations (histogram) as a function of the reconstructed e^+-jet invariant mass. The inset shows the region with $M_{ej} > 180$ GeV on a linear scale. b) The ratio of the number of observed events to the Standard Model expectations and the SM uncertainty. 27

2.20 Feynman diagram for excited (a) electron, (b) neutrino and (c) quark production at HERA. 28

2.21 Selectron-squark production via neutralino exchange and the following decays to the LSP and SM partner. 29

2.22 First generation R-parity violating squark production at HERA followed by (a), (c) R-parity violating decays and (b) and (d) gauge decays. In (b) and (d) the chargino and neutralino undergo subsequent R-parity violating decays. 30

2.23 Feynman diagram with neutralino and gravitino in the final state. 31

3.1 A schematic showing the layout of HERA. 34

3.2 Integrated luminosity per running period measured by ZEUS in 1993-2000 as a function of days. 36

3.3 Integrated luminosity measured by ZEUS in 2002-2003 as a function of days of running. 36

3.4 x-z view of ZEUS detector. 38

3.5 x-y view of ZEUS detector. 38

3.6 An octant of CTD with the wire structures. 40

3.7 A side view of the calorimeter. 41

3.8 Schematic layout of the LUMI detector's γ- calorimeter and e-calorimeter. 43

3.9 Schematic of the ZEUS trigger and data acquisition system. 45

4.1 Arrangement of the 8 scintillator tiles of the C5 counter. The light from tiles are summed such that each pair of tiles 1/2, 3/4, 5/6, and 7/8 form the readout channel 4, 2, 3, and 1, respectively. 48

4.2 Diagram of C5 counter position and readout channel numbering. 48

4.3 Main C5 data flow processes. 52

4.4 Setup for measurement of C5 detector timing resolution. 54

4.5 Timing spectrum measured with the CAEN TDC for measurement of C5 detector timing resolution. 55

4.6 Mean value of the position of proton peak (upper left plot) and electron peak (upper right plot) in the time spectrum measured by C5 detector using C.A.E.N. TDC as a function of time. Position of interaction point (Z_{IP}) calculated from $T_{proton} - T_{electron}$ Z_{IP} as a function of time (lower plot). 56

4.7 Electron bunch arrival times as measured using the C5 time distributions as a function of run number (upper plot). Electron bunch arrival times distribution for 2004 running period. 57

4.8 Proton bunch arrival times as measured using the C5 time distributions as a function of run number (upper plot). Proton bunch arrival times distribution for 2004 running period. 58

4.9 Average Z-position of the interaction vertex distributions during the 2004 running period. 59

4.10 Setup for electron and proton beam gated rate measurements. 60

4.11 Timing spectrum with electron (right) and proton (left) beam. 61

4.12 LeCroy TDC histogram. a) Full HERA bunch train. b) Zoom plot with empty bunches c) zoom plot with only one bunch filled with electrons and protons. d) Plot with first HERA bunches. e) Zoom plot with ep bunch and e only bunch. In all plots 1 bin = 1 ns. 63

4.13 HERA bunch structure measured with the LeCroy TDC and summed over all bunches in linear (upper plot) and logarithmic (lower plot) scale. The electron and proton primary bunches and the satellite bunches can be clearly seen. 64

4.14 HERA bunch structure measured with the LeCroy TDC and summed over all bunches in linear (upper plot) and logarithmic (lower plot) scale. The electron and proton primary bunches and the satellite bunches as well as the plateau of unsynchronized background particles can be seen. 65

4.15 C5 timing histogram used in GFLT. All events coming from proton peak (above 7) are rejected. 66

4.16 C5 rate as a function of HERA e beam current for different p beam current. Numbers near the curves shows day and hour of the begin of ep injection in July 2002. 68

4.17 C5 rate versus e beam energy for e-only and ep run. Numbers near the curves shows day and hour of the begin of this test in August 2002. The positron beam current was $\sim$ 5 mA. 68

4.18 Electron beam current, electron beam-pipe vacuum (right and left side from the interaction point) and C5 rate as a function of time (left column) and versus rate in C5 detector. 69

4.19 Proton beam energy (upper plot) and C5 rate (lower plot) as a function of time during proton only energy scans. 70

4.20 C5 time distribution measured by the LeCroy TDC for bad background condition at HERA. 70

6.1 Relationships between measured hadronic kinematic variables for CC interactions. The upper left plot shows the lines of constant γ_h, the upper right plot shows the lines of constant hadronic energy E_h, the lower right plot shows lines of constant hadronic transverse momentum P_T^h, and the lower left plot shows lines of constant $E - p_z$ on the $x - Q^2$ kinematic plane. 79

7.1 A typical high-gamma event. 83

7.2 A typical low-gamma event. 84

7.3 Beam-gas event. 86

7.4 Cosmic shower. 87

7.5 Halo muon. 88

7.6 γ_h, P_T, $E-P_z$ and $\frac{P_T}{E_T}$ for low gamma events (left column) and high gamma events (right column) for e^+p data after all cuts are applied. 95

7.7 The distribution of the $z-$ position of the vertex measured using FCAL timing (upper left plot) and Z-vertex measured by CTD tracking (upper right plot) for low and high gamma events, respectively. $P_T[-1ir]$ distribution for low and high gamma events are shown in lower left and lower right plots. 96

7.8 Distributions of N_{trk} (upper left), N_{Good} (upper right) and N_{trk} vs N_{Good} (lower left), where N_{trk} is the total number of CTD tracks and N_{good} is the number of "good" CTD tracks. For these plots only high gamma events are selected. The N_{cells} distribution (lower right) for e^+p data and MC after all other cuts have been applied except the cut on $N_{cells} > 50$. 99

7.9 The E_{Bemc}/E_{Bcal}, E_{Bhac1}/E_{Bcal} and E_{Bhac2}/E_{Bcal} distributions for all selected events in e^+p data and Monte Carlo samples and the E_{Femc}/E_{Fcal}, E_{Fhac1}/E_{Fcal}, E_{Fhac2}/E_{Fcal} distribution for e^+p data and MC only for events selected in low gamma region. 100

7.10 The Y_{JB}, X_{JB}, $\log_{10}(Q^2_{JB})$ distributions for e^+p data and Monte Carlo samples. 101

7.11 Jet variables for e^+p data after all cuts are applied. 102

7.12 Neutrino variables (total energy E_ν, P_T^ν and θ_ν) for selected events in e^+p data after all selection cuts are applied. 103

7.13 Mass spectrums for e^+p data for four different methods of mass reconstruction. 104

7.14 The upper plot shows a comparison of the observed e^+p samples (dots) and the CC SM expectations (yellow histogram) for the reconstructed invariant mass $M_{\nu j}$. The lower plot shows the ratio between the data and the SM expectation for e^+p data. 105

7.15 The upper plot shows a comparison of the observed e^-p samples (dots) and the CC SM expectations (yellow histogram) for the reconstructed invariant mass $M_{\nu j}$. The lower plot shows the ratio between the data and the SM expectation (N_{obs}/N_{exp}) for e^-p data. 106

7.16 Invariant mass $M_{\nu j}$ versus $\cos\theta^*$ for e^+p data (upper plot), for leptoquark Monte Carlo (middle plot) and for Charged Current Monte Carlo (lower plot). 107

7.17 The $\cos\theta^*$ distributions for all e^+p data passing the event selection (upper plot). The $\cos\theta^*$ spectrum for data and MC events with $M_{\nu j} > 180$ GeV (lower plot). 108

7.18 The $\cos\theta^*$ distributions for all e^-p data passing the event selection (upper plot). The $\cos\theta^*$ spectrum for data and MC events with $M_{\nu j} > 180$ GeV (lower plot). 109

7.19 The fractional uncertainty, $(N - N_{nom})/N_{nom}$, from each systematic effect in the measurement of $M_{\nu jets}$ spectrum. 111

8.1 Reconstructed mass spectrum for different M_{true} numbers using four different reconstruction methods M_x (left column), $M_{\nu had}$ (middle left column), $M_{\nu j}$ (middle right column), and $M_{\nu js}$ (right column). 114

8.2 Distribution of fitting parameters (μ and σ/μ) of reconstructed mass spectra using four methods (M_x, $M_{\nu had}$, $M_{\nu j}$, and $M_{\nu js}$) of mass reconstruction as a function of true leptoquark mass. 117

8.3 Distribution of fitting parameters (μ and σ) of reconstructed mass spectra using $M_{\nu js}$ method vs the true leptoquark mass. 118

8.4 Example distributions of $< \sigma_{lim} >$ as a function of $\cos\theta^*$ cut for different LQ Monte Carlo samples (e^+p sample). The minimum $< \sigma_{lim} >$ on this plot determines the final optimized cut for each LQ mass. 119

8.5 Optimized $\cos\theta^*$ cut for e^+p sample (upper left) and e^-p sample (upper right). Leptoquark efficiency after applying additional mass window and optimized $\cos\theta^*$ cut for e^+p leptoquark Monte Carlo sample (lower left) and e^-p leptoquark Monte Carlo sample (lower right). 120

8.6 The distributions of P_T^{mis}, $M_{\nu j}$, and $\cos\theta^*$ after applying mass window and $\cos\theta^*$ cuts for the e^+p data. The lower figure shows the $\cos\theta^*$ distribution for $M_{\nu j} > 180\ GeV$. 121

8.7 $\sigma \cdot \beta$ 95% CL limits for scalar (upper left) and vector (upper right) leptoquarks as a function of LQ mass. Limits on λ for scalar (lower left) and vector (lower right) leptoquarks as a function of LQ mass. 122

8.8 Number of data (large digits) and Standard Model expected events (small digits) in the plane $M_{\nu js}$ vs $\cos\theta^*$. 126

8.9 The full probability $P(\lambda)$ as a function of λ at two different masses is shown in the two upper plots. The full integral of probability $F(\lambda) = \int_0^\lambda P(\lambda_0)d\lambda_0$ as a function of λ for BRW leptoquark S_0^L at two different masses (lower plots). The vertical lines on the plots show the limit on λ, where $F(\lambda) = 0.95$. 127

8.10 The comparison of NWA, Likelihood and Frequentist limits for S0 (left plot) and V0 (right plot) leptoquarks using e^-p data and e^+p data. Limits reported by the D0 experiment at the Tevatron and from OPAL and L3 experiments at LEP are also shown. 128

8.11 Coupling limits as a function of leptoquark mass for S0, V0,S1 and V1 leptoquarks for e^-p and e^+p data using Frequentist method. Limits reported by the D0 experiment at the Tevatron and from OPAL and L3 experiments at LEP are also shown. 129

9.1 A feed-forward Neural Network with one hidden layer. 132

9.2 Distribution of input variables which was used for Neural Network training (E_T^H ,E_T^{jet}/E_T^H, $P_T^H/\sqrt{(}E_T^H)$, $(E-P_z)^H$, Q_H^2, Y_{JB}, θ_ν, and γ_h) for different MC samples. 137

9.3 Distribution of output values of the Neural Network after training on all LQ masses. 138

9.4 Input train variables after Neural Network selection and non-ep background cuts are applied. 139

9.5 The Y_{JB}, X_{JB}, and $\log_{10}(Q^2)$ distributions for data and MC after Neural Network selection and all non-ep background cuts are applied. 140

9.6 Mass spectra for e^+p data for different methods of mass reconstruction after Neural Network selection and all non-ep background cuts are applied. 141

9.7 The $\cos\theta^*$ distributions for e^+p data passing the Neural Network selection and non-ep background cuts and MC predictions. Upper and lower plots show all data and events with $M_{\nu j} > 180\ GeV$, respectively. 142

9.8 LQ efficiency after Neural Network selection and charged current cut selection. 143

9.9 Coupling limits as a function of leptoquark mass for BRW LQ V_0^L, BRW LQ V_1^L, BRW LQ S_0^L and BRW LQ S_1^L, derived from e^-p and e^+p data samples. The ANN selection is used together with the Frequentist method. 144

10.1 All possible combinations of invariant mass distribution of the final state $\nu + e + e$. Symbols denote P_T^{mis} (ν), first electron and second electron, respectively. 147

10.2 All possible combinations of invariant mass spectra of the final state ν+e+j. Symbols ν, e, j denote P_T^{mis} (ν), electron and jet, respectively. 148

10.3 All possible combinations of invariant mass spectra of the final state $\nu + j + j$. Symbols denote P_T^{mis} (ν), first jet and second jet, respectively. . . . 149

10.4 All possible combinations of invariant mass spectra of the final state $\nu + e + j + j$. Symbols denote P_T^{mis} (ν), electron, first jet and second jet, respectively. 150

10.5 All possible combinations of invariant mass spectra of the final state $\nu + e + e + j$. Symbols denote P_T^{mis} (ν), first electron, second electron and jet, respectively. 151

10.6 All possible combinations of invariant mass spectra of the final state $\nu + e+e+e$. Symbols denote P_T^{mis} (ν), first electron, second electron and third electron, respectively. 152

10.7 All possible combinations of invariant mass spectra of the final state $\nu + j + j + j$. Symbols denote P_T^{mis} (ν), first, second and third jet, respectively. 153

10.8 All possible combinations of invariant mass spectra of the final state $\nu + e + e + j + j$. Symbols denote P_T^{mis} (ν), first electron, second electron, first jet and second jet, respectively. 154

10.9 All possible combinations of invariant mass spectra of the final state $\nu + e + j + j + j$. Symbols denote P_T^{mis} (ν), electron, first jet, second jet, third jet, respectively. 155

11.1 The distribution of γ_h and $E-P_z$ of the hadronic system for 2002 data, for 99-00 data and charged current Monte Carlo for all data (right), for high γ_h events (middle) and for low γ_h events (left). 159

11.2 The distribution of vertex position and number of tracks compared to MC for 2003 and 99-00 e^+p data sets. 159

11.3 The distribution of P_T of the hadronic system and Q^2_{JB} for 2002 and $99-00$ e^+p data compared to charged current Monte Carlo for all data samples (right), for high γ_h events (middle) and for low γ_h events (left). 160

11.4 The distribution of X_{JB} and Y_{JB} for 2002 and $99-00$ e^+p data compared to charged current Monte Carlo for all data samples (right), for high γ_h events (middle) and for low γ_h events (left). 160

A.1 Various views of the C5 detector. 163

A.2 Configuration of the beamline region in the ZEUS detector. The new position of the C5 detector is near the front face of RCAL. 164

A.3 Readout diagram. 165

A.4 Racks with C5 front-end and DAQ electronics. 166

A.5 Hardware setup. 168

A.6 Setup for ADC. 170

A.7 ADC spectrum from one of the scintillator plates of C5 detector. 171

A.8 C.A.E.N. TDC setup. 172

A.9 Measurements of time using the C.A.E.N. TDC in C5 readout system. . . 173

A.10 LeCroy TDC setup. 174

B.1 The distribution of the $z-$ position of the vertex measured using FCAL timing (upper left plot) and Z-vertex measured by CTD tracking (upper right plot) for low and high gamma events respectively. $P_T[-1ir]$ distributions for low and high gamma events are shown in the lower left and lower right plots. 181

B.2 γ^h, P_T^{mis}, $E-P_z$ and $\frac{P_T^{mis}}{E_T}$ for only low gamma events (left column) and only high gamma events (right column) for e^-p data after all cuts are applied. 182

B.3 Distributions of N_{trk} (upper left), N_{Good} (upper right) and N_{trk} vs N_{Good} (lower left), where N_{trk} is the total number of CTD tracks and N_{good} is the number of "good" CTD tracks. For these plots only high gamma events are selected. The N_{cells} distribution (lower right) for e^-p data and MC after all other cuts have been applied except the cut on $N_{cells} > 50$. 183

B.4 The E_{Bemc}/E_{Bcal},E_{Bhac1}/E_{Bcal}, E_{Bhac2}/E_{Bcal} , E_{Femc}/E_{Fcal},E_{Fhac1}/E_{Fcal} and E_{Fhac2}/E_{Fcal} distributions for e^-p data and MC only for low gamma events after all cuts are applied. 184

B.5 The Y_{JB},X_{JB},$log_{10}(Q^2_{JB})$ distributions for e^-p data and Monte Carlo samples. 185

B.6 Jet variables for only low gamma events (left column) and only high gamma events (right column) in e^-p data after all cuts are applied. 186

B.7 Neutrino variables total energy E_ν, P_T^ν and θ_ν for selected events in e^-p data sample after all selection cuts are applied. 187

B.8 Mass spectra for e^-p data for four different methods of mass reconstruction. 188

C.1 One interesting event was found in e^+p data. This event has $Q^2 \sim 50166.5\,\mathrm{GeV}^2$ and $\cos\theta^* \sim -0.49$. The invariant mass of ν and jet gives the value $M_{\nu j} \sim 246$ GeV. 189

C.2 This event found in e^+p data and has $M_{\nu j} > 250$ GeV ($Q^2 \sim 13500$ GeV^2 and $\cos\theta^* \sim 0.567$). 190

C.3 A typical high-$M_{\nu j}$ event with $M_{\nu j} = 247$ GeV. 190

C.4 Example of an event with P_T^{mis} + 3(4) jets in the final state. 191

C.5 Example of an event with P_T^{mis} + electron + two jets in the final state. . 191

C.6 Example of an event with P_T^{mis} + two electrons + jet in the final state. . 192

C.7 High mass event selected with the signature $\nu+e+j+j$, $\nu+e+e+j$ or $\nu+e+e+e$. 192

List of Tables

2.1 Three generation of quarks and leptons (half-integer spin). 3

2.2 SM fundamental forces. 4

2.3 Quantum numbers of scalar and vector leptoquarks with $SU(3) \times SU(2) \times U(1)$ invariant couplings to quark-lepton pairs. 15

2.4 The $F = 0$ and $F = 2$ leptoquarks in the Buchmüller-Rückl-Wyler model that can be produced at HERA. 16

2.5 Leptoquarks angular spectrum. 19

2.6 Lower limits on M_{LQ}/λ (TeV^{-1}). 24

2.7 Number of observed and expected events from H1 and ZEUS. The last column gives the probability that the expected NC DIS signal fluctuates to values equal to or larger than the number of observed events. 25

2.8 The f^* decay modes and subsequent final states. 29

3.1 HERA design parameters and performance evolution as a function of running period. 35

3.2 HERA luminosity written to tape at ZEUS. 35

3.3 The acronyms used for the different component of the ZEUS detector. . . . 37

3.4 The Central Tracking Detector. 39

3.5 Parameters of the uranium calorimeter. 42

4.1 High voltage setting for photo multiplier in Aug 2001. 49

5.1 The CC DIS MC samples for e^+p and e^-p simulation. 72

5.2 The PhP MC samples. 73

7.1 Summary of calorimeter timing cuts. 89

7.2 Cumulative efficiency for MC samples and e^+p data are shown. Group 1 includes only events from the high gamma sample. Group 2 includes only low gamma events. The total efficiency is summarized in group 3. 98

8.1 Mass limit of the 4 BRW LQs at $\lambda = 0.1$ and $\lambda = 0.31$. 125

9.1 Background and signal samples used for training. 134

9.2 Comprasion of standard cut selection and Neural Network selection 135

9.3 Comparison of standard cut selection and Neural Network selection. Efficiency and number of observed events are normalized to the luminosity of data. 136

10.1 The data and Standard Model expectation for all event classes with data events. 146

A.1 Discriminator thresholds. 167

A.2 Scaler inputs (see Fig. A.5). 169

A.3 ADC inputs. 170

A.4 TDC C.A.E.N. inputs. 171

A.5 LeCroy TDC inputs. 172

A.6 Defined parameters for LeCroy TDC. 173

A.7 Input-Output Register. 173

A.8 Configuration file “vme.conf”. 175

A.9 Configuration file “C5config.conf”. 176

A.10 Main processes which have to be started on zenc5.desy.de. 178

Chapter 1

Introduction

The HERA *ep* collider offers unique possibilities to search for resonant production of new particles which couple to lepton-quark pairs. Many extensions of the Standard Model (SM) predict the existence of particles carrying both baryon and lepton number, such as leptoquarks or squarks. In *ep* collisions, such states may be produced directly through electron-quark fusion,

$$e^{\pm} + p \rightarrow LQ + X \rightarrow e(\nu) + jet(s) + X, \tag{1.1}$$

with subsequent decays into electron and quark or neutrino and quark, yielding peaks in the spectra of final-state lepton-jet invariant mass.

This thesis describes a search for lepton-quark resonant states that decay to neutrino (antineutrino) and a quark using $e^{-}p$ and $e^{+}p$ data collected by the ZEUS detector at HERA. The authors contribution to the C5 detector, an essential part of the ZEUS detector, is also described.

The thesis is organized as follows.

Chapter Two contains a brief overview of the theoretical concepts on which the Standard Model is based. The kinematic variables used to describe DIS process and processes beyond the Standard Model, including leptoquarks, are then derived. The differential cross-sections for backgrounds to the leptoquark process from charged current (CC) DIS events, predicted by the Standard Model and characterized by the "missing" transverse momentum P_T^{mis} carried off by the undetected neutrino, and photoproduction events are stated. Theories beyond the Standard Model with lepto-quarks are described followed by a review of searches and existing experimental limits of the production of leptoquarks using the Buchmüller-Rückl-Wyler model. The missing P_T^{mis} signature is then generalized to other exotic physics, e.g. excited fermions.

Chapter Three describes the experimental setup, focusing on the relevant aspects of the

HERA collider and on the ZEUS detector, used to perform the analysis presented.

Chapter Four contains a detailed description of the C5 counter installed during the HERA 2000-2001 shutdown into ZEUS. The C5 counter is essential to ZEUS data taking providing background event rejection and monitoring of beam conditions. Realtime analysis of beam conditions are used by HERA to optimize and maintain stable data taking conditions at ZEUS.

Chapter Five outlines the Monte Carlo simulation techniques and datasets generated for use in this analysis.

Chapter Six defines the reconstruction quantities used in the leptoquark analysis and describes the various techniques available for reconstructing the kinematic properties of an event, including the mass of a hypothetical leptoquark, using experimentally measured properties.

Chapter Seven reviews the selection criteria applied to the data during the selection of events used in the leptoquark analysis.

Chapter Eight describes how, in the absence of a significant leptoquark signal, limit on leptoquark production cross-section and coupling constant are derived within the framework of the Buchmüller-Rückl-Wyler model using the Narrow Width Approximation, Likelihood and Frequentist methods.

Chapter Nine details the implementation of a Artificial Neural Network analysis designed to improve the signal and suppress background.

Chapter Ten generalize the missing transverse momentum signature used previously, in *Chapter Seven*, to allow rudimentary searches for additional exotics physics beyond the Standard Model.

Chapter Eleven describes a first look at the post HERA-II upgrade data.

Finally in *Chapter Twelve* conclusions are drawn.

Chapter 2

Theory

2.1 The Standard Model

The Standard Model (SM) of particle physics describes the behavior of the subatomic world in the framework of renormalizable gauge theories whose elementary particles are spin $\frac{1}{2}\hbar$ fermions and spin 0 or $\hbar$ bosons, where h is the Planck constant $\hbar \equiv h/2\pi = 1.05 \cdot 10^{-34}$ J s. Fermions are either leptons or quarks which enter the model as left-handed douplets or right-handed singlets, respectively.

According to the Standard Model the physical world is constructed from three generations of leptons and three generations of quarks as shown in Table 2.1.

Table 2.1: Three generation of quarks and leptons (half-integer spin).

	Quarks			Leptons		
		Mass	q (e)		Mass	q (e)
1	up (u) down (d)	$\sim 4\ MeV$ $\sim 7\ MeV$	$+2/3$ $-1/3$	electron (e) electron neutrino (ν_e)	$\sim 0.51\ MeV$ $< 3\ eV$	-1 0
2	charm (c) strange (s)	$\sim 1.2\ GeV$ $\sim 150\ MeV$	$+2/3$ $-1/3$	muon (μ) muon neutrino (ν_μ)	$\sim 105.7\ MeV$ $< 0.19\ MeV$	-1 0
3	top (t) bottom (b)	$\sim 175\ GeV$ $\sim 4\ GeV$	$+2/3$ $-1/3$	tau (τ) tau neutrino (ν_τ)	$\sim 1777\ MeV$ $< 18.2\ MeV$	-1 0

In the Standard Model fermions interact by the exchange of field quanta (bosons) which determine the properties of the interaction. The three fundamental interactions, or forces, needed within the SM to explain experimental results are listed in Table 2.2.

Table 2.2: SM fundamental forces.

interaction	theory	gauge bosons	charge / e	mass
strong	quantum chromodynamic (QCD)	gluons g_i $(i = 1...8)$	0	0
weak	electroweak	W Z	$+1, -1$ 0	80.4 GeV 91.2 GeV
electromagnetic	electroweak	gamma	0	0

The gauge transformations of the gauge bosons can be exactly described using a unitary group called a "gauge group". The gauge group of the strong interaction is $SU(3)$, the gauge group of the weak interaction is $SU(2)$ and $U(1)$ describes hypercharge (the gauge group of the electroweak interaction is $SU(2) \times U(1)$). The Standard Model is often referred to as $SU(3) \times SU(2) \times U(1)$ [1].

2.2 Deep inelastic electron-proton scattering

High energy ep-collisions are described in the Standard Model by the exchange of a virtual boson between the electron (positron) and the proton. If the ep-collision is sufficiently energetic, so that the momentum transfer is large and the interaction is highly inelastic, the electron will collide directly with a single quark. This process is called Deep Inelastic Scattering (DIS). An event is called neutral current (NC) if the initial state electron or positron scatters into the final state (γ/Z-boson exchange) and charged current (CC) if a neutrino derived from the initial state lepton appears in the final state (W-boson exchange).

$$e^{\pm} + p \xrightarrow{\gamma/Z^0} e^{\pm} + jet(s) + X \tag{2.1}$$

$$e^{\pm} + p \xrightarrow{W^{\pm}} \nu(\bar{\nu}) + jet(s) + X \tag{2.2}$$

The kinematics of neutral and charged current DIS processes are defined in the Feynman diagrams of Fig. 2.1,

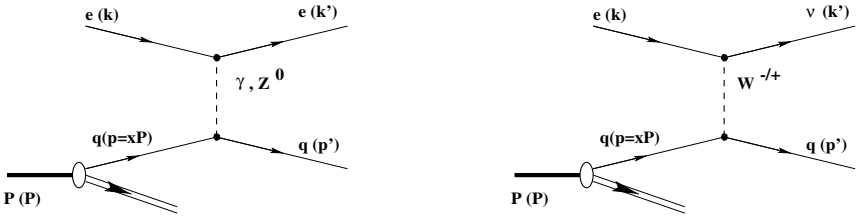

Figure 2.1: Neutral and charged current deep inelastic scattering.

where:

E_e^{beam} = electron (positron) beam energy
E_P^{beam} = proton beam energy
$k = (\overrightarrow{k}, E_e^{beam})$ = four momentum of incoming electron
$P = (\overrightarrow{P}, E_P^{beam})$ = four momentum of incoming proton
$k' = (\overrightarrow{k'}, E_l')$ = four momentum of scattered lepton
θ_l = the measured angle between the scattered electron trajectory and the incoming proton direction.
$P^h = (\overrightarrow{p^h}, E^h)$ = four momentum of hadronic final state.

The center of mass energy at HERA, 318 GeV, is sufficiently large that individual fermion masses may be neglected. The four-momentum of the exchanged gauge boson, q, i.e. the

four-momentum transfer of the reaction, is given by

$$q \equiv k - k' \tag{2.3}$$

The negative of the four-momentum transfer squared, Q^2, is often used to describe the DIS kinematics,

$$Q^2 \equiv -q^2 = -(k - k')^2 \tag{2.4}$$

In the quark parton model (QPM) [2] the Bjorken scaling variable, x, is the fraction of the proton momentum carried by the struck parton in the frame where the momentum of the proton is much larger than the proton mass,

$$x \equiv \frac{Q^2}{2P \cdot q} \tag{2.5}$$

where x lies in the range from 0 to 1.

The inelasticity of the lepton, y, is defined as

$$y \equiv \frac{P \cdot q}{P \cdot k} \tag{2.6}$$

The meaning of y is straightforward in the proton rest frame where it corresponds to the fractional energy transfer. By definition y lies in the range 0 to 1.

The variables Q^2, x and y are related to each other by a simple formula when the masses of the lepton and nucleon are neglected,

$$Q^2 = x \cdot y \cdot s, \tag{2.7}$$

where s is the square of the center-of-mass energy of the interaction.

$$s \equiv (P + k)^2 \tag{2.8}$$

Fig. 2.2 shows the x, Q^2 kinematic region covered by the HERA experiments, ZEUS and H1, and by other fixed target DIS experiments. Below $y = 0.005$, corresponding to small s, fixed target experiment measurements are significant, above results from HERA are significant.

In the electron-quark rest frame (see Fig. 2.3) the lepton scattering angle, θ^*, is related to y via,

$$\cos\theta^* = 1 - 2y \tag{2.9}$$

The invariant mass of the electron-quark system M_{lq} is related to x by

$$M_{lq} = \sqrt{xs} \tag{2.10}$$

Color confinement requires that the outgoing struck quark undergoes color flow with the proton remnant and hadronizes into hadrons. Measurement of the hadronized energy deposits in the detector, followed by clustering into a so called jet, allow the energy and angle of the outgoing quark to be reconstructed.

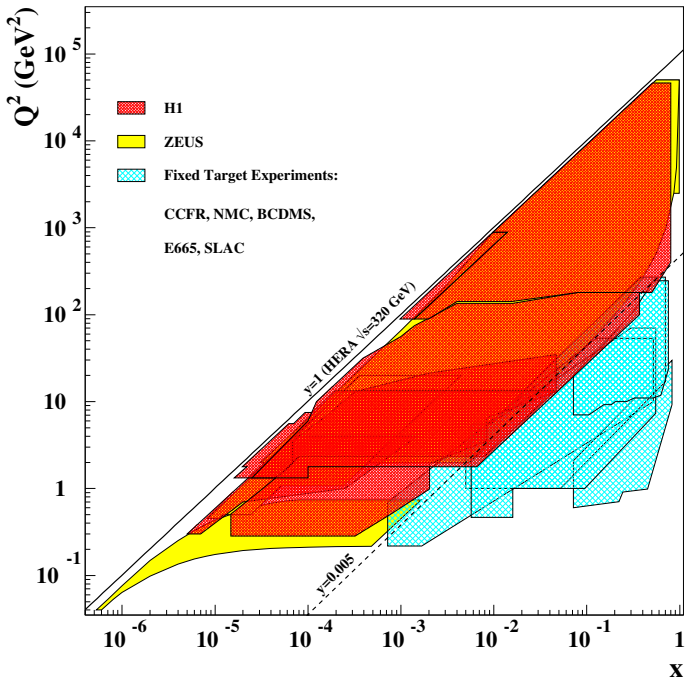

Figure 2.2: Kinematic (x, Q^2) region accessible at HERA compared to fixed target experiments.

2.3 *ep* background processes

All events with missing P_T^{mis} are potential background candidates to the searches presented in this thesis. In this section the production kinematics, including cross-sections, of the CC primary background and NC DIS and photoproduction backgrounds, are reviewed.

2.3.1 Neutral current and charged current DIS

The cross section for the charged current Deep Inelastic Scattering processes (CC DIS) [3] is given by:

$$\frac{d^2\sigma(ep)}{dx\,dy} = \frac{G_F^2(s-M^2)}{2\pi}\frac{M_W^4}{(Q^2+M_W^2)^2}\times F \tag{2.11}$$

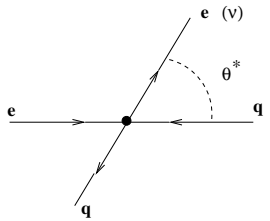

Figure 2.3: Electron and quark scattering in the electron-quark center of mass frame.

where G_F denotes the Fermi constant, M is the mass of incoming proton, M_W is the mass of the W boson, and F is:

$$F = \left\{\left[1-y-\frac{M^2xy}{(s-M^2)}\right]\ F_2^{CC} + \frac{y^2}{2}2xF_1^{CC} + (y-\frac{y^2}{2})xF_3^{CC}\right\},$$

where F_1^{CC}, F_2^{CC} and F_3^{CC} are the three charged current structure functions in the quark parton model. For e^-p scattering these are:

$$F_2^{CC} = 2xF_1^{CC} = 2x\left[\sum_{q=u,c,t} q(x,Q^2) + \sum_{q=\bar{d},\bar{s},\bar{b}} \bar{q}(x,Q^2)\right] \tag{2.12}$$

$$F_3^{CC} = 2\left[\sum_{q=u,c,t} q(x,Q^2) - \sum_{q=\bar{d},\bar{s},\bar{b}} \bar{q}(x,Q^2)\right] \tag{2.13}$$

and for e^+p scattering:

$$F_2^{CC} = 2xF_1^{CC} = 2x\left[\sum_{q=d,s,b} q(x,Q^2) + \sum_{q=\bar{u},\bar{c},\bar{t}} \bar{q}(x,Q^2)\right] \tag{2.14}$$

$$F_3^{CC} = 2\left[\sum_{q=d,s,b} q(x,Q^2) - \sum_{q=\bar{u},\bar{c},\bar{t}} \bar{q}(x,Q^2)\right] \tag{2.15}$$

The parton density functions (PDFs), $q(x, Q^2)$, give the probability to find a quark, q, with momentum fraction x at a given Q^2. Fig. 2.4 shows, as an example, the PDFs extracted from the ZEUS and H1 next-to-leading order QCD analysis of data on deep inelastic scattering [4]. As can be seen from the plots, the u and d valence quark densities dominate at large values of x ($x \gtrsim 0.3$), while sea-quarks and gluons are only important at low values of x.

The cross section for neutral current DIS processes can be written in terms of two electromagnetic structure functions F_1^{em} and F_2^{em}:

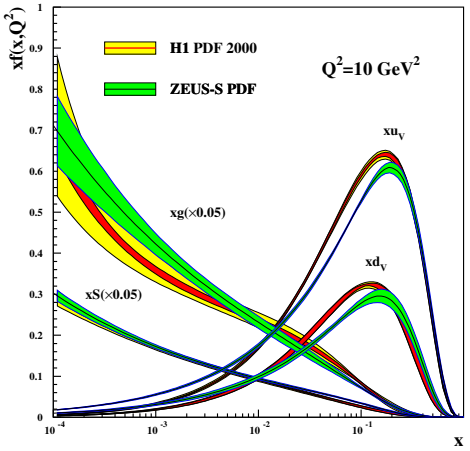

Figure 2.4: The u and d valence quark and the gluon and sea distributions extracted from ZEUS and H1 NLO fits at $Q^2 = 10$ GeV^2.

$$\frac{d^2\sigma(ep)}{dx\ dy} = \frac{4\pi\alpha^2(s-M^2)}{Q^4}\left[(1-y)F_2^{em} + y^2 xF_1^{em} - \frac{M^2}{(s-M^2)}xyF_2^{em}\right] \qquad (2.16)$$

where α denotes the fine structure constant. The full neutral current cross section, including electroweak contributions, can be found in [5].

Fig. 2.5 shows the differential NC and CC cross sections measured by the ZEUS and H1 collaborations as a function of Q^2 for e^-p and e^+p scattering. The charged current cross section is suppressed with respect to the neutral current cross section until Q^2 reaches the value of the vector boson masses squared ($\sim 10^4$ GeV).

2.3.2 Photoproduction

In the photoproduction process (PhP) a quasi-real photon is exchanged between the electron and proton. Interactions involving quasi-real photons ($Q^2 \approx 0$, where Q^2 is the virtuality of the photon) are well described by calculations that use a partonic structure for the photon [6], [7]. As the exchange momentum is small the outgoing electron is practically undeflected, remaining close to the beamline, and is not detected in the experiment. The detection of hadronic remnants produces a P_T^{mis} event signature.

PhP is separated into two subprocesses, called direct and resolved photoproduction. In

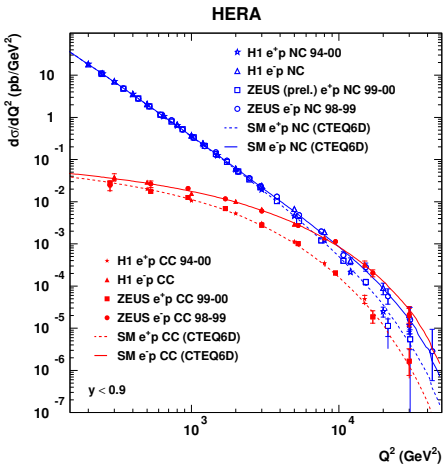

Figure 2.5: The differential NC and CC cross sections as a function of Q^2 measured by the ZEUS and H1 collaborations for e^-p and e^+p scattering (from [4]).

direct photoproduction the exchanged photon participates in hard scattering. In resolved PhP the photon fluctuates into a hadronic system, which acts as a source of partons that interact with the proton. The Feynman diagrams for the two subprocesses are shown in Fig. 2.6. As can be seen from these diagrams both processes can lead to two jets in the final state.

The ZEUS [8] and H1 [9] collaborations, at HERA, have studied dijet and inclusive jet production over large ranges of incident photon virtualities, including photoproduction, DIS, and the transition region between them. Figure 2.7 shows the differential dijet cross section, $d\sigma/dQ^2$, for $E_T^{\mathrm{jet1}} > 7.5$ GeV, $E_T^{\mathrm{jet2}} > 6.5$ GeV, $-3 < \eta^{\mathrm{jet}} < 0$, $0.2 < y < 0.55$ and $0.1 < Q^2 < 2000$ GeV^2 together with the photoproduction measurement. Contributions to the PhP cross-section from the direct-enhanced region ($x_\gamma^{obs} \geq 0.75$) and the resolved-enhanced region ($x_\gamma^{obs} < 0.75$) are also shown.

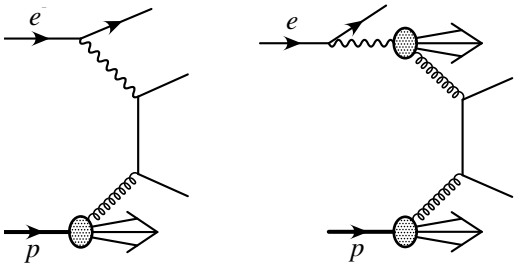

Figure 2.6: Feynman diagrams representing direct (left) and resolved (right) photoproduction.

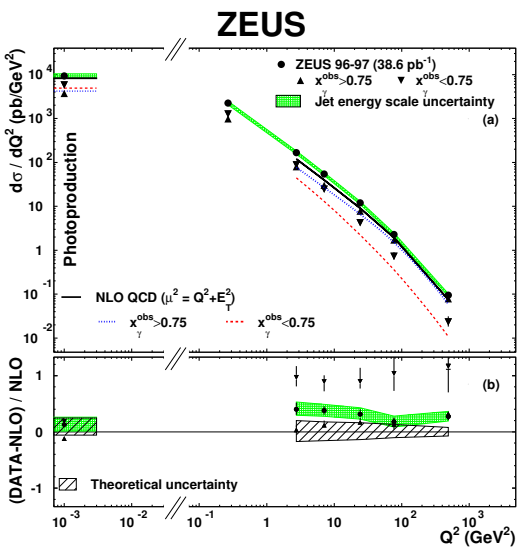

Figure 2.7: (a) Measured dijet cross sections $d\sigma/dQ^2$ for $x_\gamma^{obs} \geq 0.75$ (▲) $d\sigma/dQ^2$ for $x_\gamma^{obs} < 0.75$ (▼) and $d\sigma/dQ^2$ for the entire x_γ^{obs} region (•). (b) Relative difference of the measured dijet cross section $d\sigma/dQ^2$ to the DISASTER++ ($\mu^2 = Q^2 + (E_T^{jet})^2$) and of Frixione and Ridolfi ($\mu^2 = (E_T^{jet})^2$) calculations. The hatched band shows the theoretical uncertainty of the calculations.

2.4 Theories beyond the Standard Model

Although the Standard Model has been tested repeatedly and found to be in good agreement with experimental evidence, there are reasons to believe that it is not the ultimate theory of fundamental particles and their interactions. Many open questions and problems exist:

Gravity. The Standard Model does not embrace the gravitational force and it is not understood why the strength of gravity is 36 orders of magnitude weaker then that of the electroweak force.

Higgs Boson and particle masses. The Higgs boson is introduced into the Standard Model to explain the generation of particle masses. Gauge bosons and fermions are assumed to obtain their masses through interaction with the Higgs field. The Higgs boson has not, yet, been observed.

Generation problem. The Standard Model contains no explanation for the apparent symmetry between quark and lepton sectors. The Standard Model does not predict the number of generations.

The many gauge theories which attempt to unify the fundamental forces are referred to collectively as Grand Unification Theories (GUT) [60]. A viable grand unification theory group, G, is expected to contain the experimentally verified Standard Model symmetry group $SU(3) \times SU(2) \times U(1)$. The result of such higher dimensional unification is the introduction of new particles and forces not contained within the Standard Model. Some of these forces lead to transitions between leptons and quarks mediated by leptoquark gauge bosons which carry both baryon number (B) and lepton number (L). Some of the Grand Unified theories which predict the existence of leptoquarks are listed below.

- *Pati-Salam $SU(4)$ model*
  Leptoquarks were first introduced by the Pati-Salam model. The Pati-Salam $SU(4)$ [10] model predicts vector gauge bosons with masses of $\sim 50 - 100$ TeV and incorporates quark and lepton number non-conservation as well as proton decay.

- *Georgi and Glashow $SU(5)$ model*

  In 1974, Howard Georgi and Sheldon Glashow proposed the $SU(5)$ model, which is the simplest possible grand unified theory and contains the Standard Model (SU(3) x SU(2) x U(1)) [11]. An $SU(N)$ gauge theory has $N^2 - 1$ gauge bosons. For the $SU(5)$ model these are:

$$24 = (8,1) + \underbrace{(1,3) + (1,1)}_{W^\pm, Z, \gamma} + \underbrace{(3,2) + (\bar{3},2)}_{X, Y bosons} \qquad (2.17)$$

  gluons

where X and Y are a new pair of superheavy gauge bosons, which mediate interactions turning quarks into leptons:

$$(u,d)_L \rightarrow e_L^+ + (\bar{Y},\bar{X}) \tag{2.18}$$

The X and Y gauge bosons do not conserve quark and lepton number and allow forbidden processes such as proton decay. The resulting proton lifetime can be estimated as

$$\tau_p \simeq \frac{M_X^4}{m_p^5}, \tag{2.19}$$

where m_p is proton mass and M_X is the mass of the X boson [11].

- *Buchmüller -Rückl-Wyler model*
  A consistent classification of leptoquarks under the gauge symmetries of the Standard Model ($SU(3) \times SU(2) \times U(1)$) is defined by Buchmüller, Rückl and Wyler [12]. A detailed description of this model is given in section 2.5.1.

- *Supersymmetric models*
  Supersymmetric models (SUSY) [16] attempt to unify fermions and bosons by assigning each fermion a supersymmetric boson partner and each boson a supersymmetric fermion partner. Thus there are two new families of so called sparticles. These theories also assert that particles and their superpartners are symmetric in a superspace. No such sparticles have yet been observed experimentally, which requires that the symmetry is not exact, allowing sparticles to have larger masses than their Standard Model partners.

  The minimal supersymmetric extension of the Standard Model (MSSM) conserves a quantity known as R-parity, defined as $R_P = (-1)^{2S+3B+L}$, where S denotes spin, B baryon number, and L lepton number. R_P is equal to $+1$ for all particles in the Standard Model and -1 for their supersymmetric partners. Supersymmetric theories with broken R-parity may also exist. In such models the heavy supersymmetric partner of the quarks may couple to a lepton-quark pairs.

- *Compositeness theories*
  Compositeness theories [14] predict that leptons and quarks as well as $W^{\pm}$ and Z bosons are made of more fundamental particles called preons. Preons can also compose fractionally charged color triplet bosons, such as leptoquarks.

- *Technicolor theories*
  Technicolor theories [15] attempt to improve the Higgs mechanism, by predicting the existence of spin 1/2 technifermions whose interactions are governed by technicolor symmetry. The technifermions can constitute bound states with the characteristics of leptoquarks.

- *Superstring theories*
  Superstring theories [13] attempt to describe all particles as 11-dimensional strings which vibrate at different resonant frequencies. Superstring models based on the E_6 grand unified group lead to a number of low-energy predictions including the existence of leptoquarks with low masses ($\lesssim 1$ TeV) which are accessible for discovery

at existing particle colliders. Besides quark-lepton Yukawa couplings these theories also have quark-quark couplings fixed by gauge symmetries requiring leptoquark masses to be very heavy if ($\gtrsim 10^{11-12}$ GeV) fast proton decay is to be avoided.

2.5 Leptoquark searches

In this chapter the theoretical concepts of Buchmüller, Rückl and Wyler [12], which provide a consistent classification of leptoquarks under the gauge symmetries of the Standard Model ($SU(3) \times SU(2) \times U(1)$), are presented. BRW leptoquarks that can be produced at HERA are also discussed in this chapter. Limits on resonant-state production from other experiments are also reviewed.

2.5.1 Buchmüller-Rückl-Wyler model

The Buchmüller-Rückl-Wyler model assumes the existence of a higher symmetry that connects quarks to leptons. This models predicts the existence of chiral leptoquark species with baryon and lepton number conservation in order to avoid limits set by experiments. The leptoquarks defined are required to couple to the same generations of leptons and quarks. An effective lagrangian with the most general dimensionless $SU(3)\times SU(2)\times U(1)$ invariant couplings of scalar and vector leptoquarks satisfying baryon and lepton number conservation can be written as:

$$\mathcal{L} = \mathcal{L}_{F=2} + \mathcal{L}_{F=0}, \tag{2.20}$$

where the fermion number F is related to baryon and lepton numbers by $F = 3B + L$. The full effective lagrangian can be found in [17].

The possible quantum numbers of leptoquark states can be restricted by assuming that their direct interactions with Standard Model fermions are dimensionless and invariant under the SM gauge group. Table 2.3 shows the QCD representation, weak isospin representation, and weak hypercharge, respectively. The spin of a leptoquark state is taken to be 1 (vector leptoquark) or 0 (scalar leptoquark) (Table 2.4)

Table 2.3: Quantum numbers of scalar and vector leptoquarks with $SU(3)\times SU(2)\times U(1)$ invariant couplings to quark-lepton pairs.

Spin	3B+L	$SU(3)_C$	$SU(2)_W$	$U(1)_Y$
0	-2	3	1	1/3
0	-2	3	1	4/3
0	-2	3	3	1/3
1	-2	3	2	5/6
1	-2	3	2	-1/6
0	0	3	2	7/6
0	0	3	2	1/6
1	0	3	1	2/3
1	0	3	1	5/3
1	0	3	3	2/3

Table 2.4: The $F = 0$ and $F = 2$ leptoquarks in the Buchmüller-Rückl-Wyler model that can be produced at HERA.

LQ species	Charge	Production	Decay	Branching ratio	Coupling
$S^L_{1/2}$	5/3	$e^+_R u_R$	e^+u	1	λ_L
$S^R_{1/2}$	5/3	$e^+_L u_L$	e^+u	1	λ_R
	2/3	$e^+_L d_L$	e^+d	1	$-\lambda_R$
$S\ ^L_{1/2}$	$-2/3$	$e^+_R d_R$	e^+d	1	λ_L
V^L_0	2/3	$e^+_R d_L$	e^+d	1/2	λ_L
			$\nu^-_e u$	1/2	λ_L
V^R_0	2/3	$e^+_L d_R$	e^+d	1	λ_R
$V\ ^R_0$	5/3	$e^+_L u_R$	e^+u	1	λ_R
V^L_1	5/3	$e^+_R u_L$	e^+u	1	$\sqrt{2}\lambda_L$
	2/3	$e^+_R d_L$	e^+d	1/2	$-\lambda_L$
			$\nu^-_e d$	1/2	λ_L
S^L_0	$-1/3$	$e^-_L u_L$	e^-u	1/2	λ_L
			$\nu_e d$	1/2	$-\lambda_L$
S^R_0	$-1/3$	$e^-_R u_R$	e^-u	1	λ_R
$S\ ^R_0$	$-4/3$	$e^-_R d_R$	e^-d	1	λ_R
S^L_1	$-1/3$	$e^-_L u_L$	e^-u	1/2	$-\lambda_L$
			$\nu_e d$	1/2	$-\lambda_L$
	$-4/3$	$e^-_L d_L$	e^-d	1	$-\sqrt{2}\lambda_L$
$V^L_{1/2}$	$-4/3$	$e^-_L d_R$	e^-d	1	λ_L
$V^R_{1/2}$	$-4/3$	$e^-_R d_L$	e^-d	1	λ_R
	$-1/3$	$e^-_R u_L$	e^-u	1	λ_R
$V\ ^L_{1/2}$	$-1/3$	$e^-_L u_R$	e^-u	1	λ_L

From the effective lagrangian, Eq. 2.20, leptoquark partial decay widths can be calculated. For scalar ($J = 0$) and vector ($J = 1$) leptoquarks the decay widths are:

$$\Gamma_{J=0} = \frac{\lambda^2 M_{LQ}}{(16\pi)} \tag{2.21}$$

$$\Gamma_{J=1} = \frac{\lambda^2 M_{LQ}}{(24\pi)}, \tag{2.22}$$

where λ denotes the leptoquark couplings to the particular final state given in the Tab. 2.4. Note that for leptoquarks with masses of 200 GeV and couplings ~ 1.0 the width will be $\Gamma \sim 4$ GeV and for couplings of 0.01 the width will be of the order of a MeV.

The leptoquark eq-fusion production cross-section for the production of scalar ($J = 0$) and vector ($J = 1$) leptoquarks in the narrow-width approximation (NWA) is given by:

$$\sigma(ep \to LQ) = (J+1)\frac{\pi}{4s}\lambda^2 q\left(\frac{M^2_{LQ}}{s}\right), \tag{2.23}$$

where $q(x)$ is the probability of finding a quark (antiquark) with momentum fraction $x = \frac{M^2_{LQ}}{s}$ inside a proton and $\sqrt{s}$ is the total ep center-of-mass energy (at HERA $\sqrt{s} \simeq$

318 GeV). For small lepton-quark couplings ($\lambda < 0.3$) and $M_{eq} < \sqrt{s}$, a narrow resonance produced through the s-channel provides the dominant contribution over the Standard Model background. The numerical calculations of the NWA cross-section are shown in Fig. 2.8 for $\lambda = 0.1$.

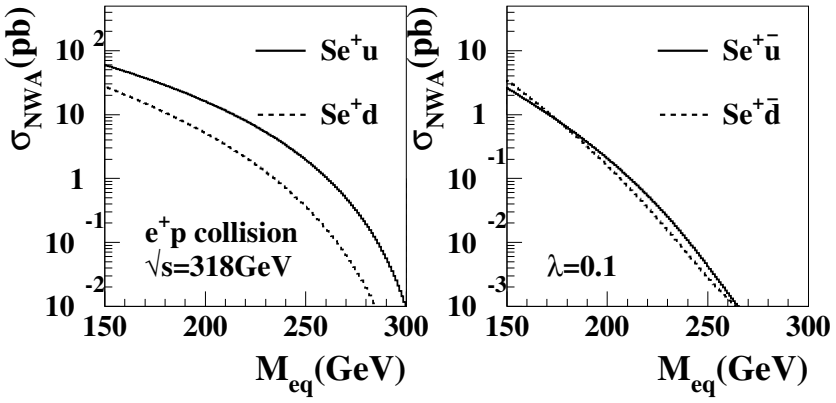

Figure 2.8: The NWA production cross-sections for four kinds of scalar resonances in e^+p collision at $\sqrt{s} = 318$ GeV.

In the Buchmüller-Rückl-Wyler model fourteen possible LQ species are classified as shown in Tab. 2.4. For each of the possible leptoquarks the branching ratio to eq and νq decays, $\beta(eq)$ and $\beta(\nu q)$ respectively, are fixed. Most of the LQs decay through the eq channel with branching ratio $\beta(eq) = 1$ and only four kinds of leptoquarks have $\beta(\nu q) = \beta(eq) = 1/2$. Although the most studied decay mode of leptoquarks has been the eq channel, the four kinds of leptoquarks which decay into νq are also interesting.

2.5.2 Leptoquarks in ep collisions

In ep-collisions leptoquarks can be resonantly produced in the s-channel or exchanged in the u-channel between the incoming lepton and a quark coming from the proton. This is illustrated in Feynman diagrams Fig. 2.9. The leptoquark decay processes

$$e^{\pm} + p \rightarrow LQ + X \rightarrow e^{\pm} + jet(s) + X, \tag{2.24}$$

$$e^{\pm} + p \rightarrow LQ + X \rightarrow \nu(\bar{\nu}) + jet(s) + X \tag{2.25}$$

are similar to those of deep inelastic neutral and charged current interactions (see Eq. 2.1, 2.2). The amplitudes for both processes interfere with those from DIS.

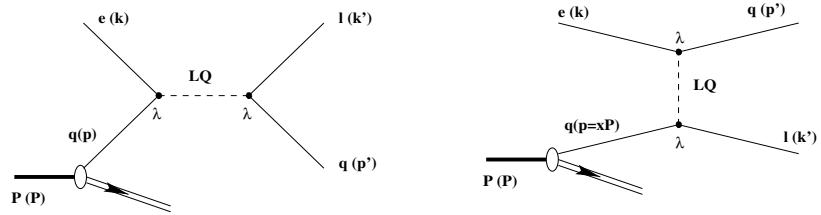

Figure 2.9: Diagrams of s-channel resonant production (left) and u-channel exchange of a leptoquark (right).

The full double differential cross-section formula can be written as

$$\frac{d^2\sigma}{dxdQ^2} = \frac{d^2\sigma_{SM}}{dxdQ^2} + \frac{d^2\sigma^{Int}_{u/SM}}{dxdQ^2} + \frac{d^2\sigma^{Int}_{s/SM}}{dxdQ^2} + \frac{d^2\sigma_u}{dxdQ^2} + \frac{d^2\sigma_s}{dxdQ^2}, \tag{2.26}$$

where the first term represents the Standard Model contribution, the second (third) term is the interference term between the Standard Model and the u-channel (s-channel) leptoquark exchange, and the fourth (fifth) term is the u-channel (s-channel) leptoquark exchange contribution.

Scalar leptoquarks produced in the s-channel decay isotropically in their rest frame and consequently the $\cos\theta^*$ or y dependence of the leptoquark cross section is flat [24]. In contrast, the leptoquark cross section has a $(1 + \cos\theta^*)^2$ dependence for vector s-channel production and scalar u-channel exchange. Since the DIS cross-section contains a $1/y^2$ dependence these characteristics can be used to distinguish leptoquark from Standard Model DIS events, see Table 2.5.

Leptoquarks with masses smaller than the center-of-mass energy ($\sqrt{s} < M_{LQ}$) are expected to produce Breit-Wigner resonances in the x distributions ($M^2_{LQ} = xs$).

Table 2.5: Leptoquarks angular spectrum.

	Angular Spectrum y Shape	
	Scalar	Vector
s-channel	flat	$(1 - y)^2$
u-channel	$(1 - y)^2$	flat

2.5.3 Experimental limits on leptoquarks production

The results of searches for any resonant state that couples leptons and quarks (not necessarily the leptoquarks from BRW model) from previous experiments are summarized below.

Proton decay

Leptoquarks in $SU(5)$ theory which do not conserve baryon and lepton number are expected to allow the proton decay process $p \rightarrow \pi^0 + e^+$, see Fig. 2.10.

The measured proton lifetime lower limit of 0.6×10^{30} years [11] requires that leptoquarks masses are larger than 10^{14} GeV/c^2.

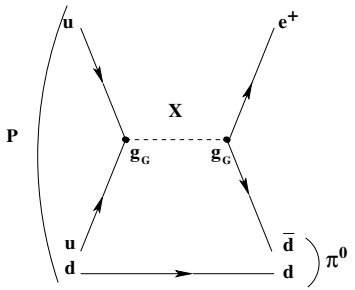

Figure 2.10: Feynman diagram showing proton decay via X-boson (leptoquark) exchange which does not conserve baryon and lepton number.

e^+e^- limits

Many Feynman diagrams are expected to contribute to single leptoquark production in electron-positron collisions. The dominant diagram is $eq \rightarrow LQ$ (Fig. 2.11), where a

photon, radiated from the incoming beam, serves as a source of quarks through fluctuations into hadronic states. The electron-quark interaction produces a leptoquark which is assumed to subsequently decay into an electron, or neutrino, and a quark. The diagrams shown in Fig. 2.12 are also relevant. Note that e^+e^- annihilation diagrams with a single leptoquark radiated in the final state and diagrams with quark and/or leptoquark exchange in the t-channel but without photon exchange are suppressed. The signature of single leptoquark events is one hadronic jet with high transverse momentum balanced either by one isolated electron or by missing transverse energy due to the neutrino.

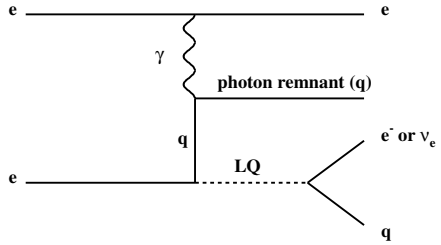

Figure 2.11: Feynman diagram showing s-channel production of a leptoquark in electron-photon scattering. The photon is radiated by one of the incoming beams and fluctuates into a hadronic object.

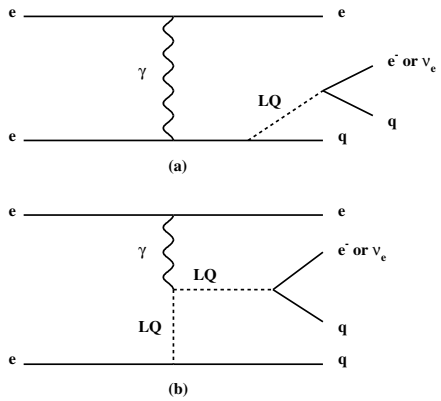

Figure 2.12: Feynman diagrams showing alternative single leptoquark production mechanisms, where the photon interaction is: (**a**) a "direct" interaction with the beam electron, or (**b**) absorbed by the leptoquark "emitted" by the other beam electron.

The OPAL collaboration at LEP has used e^+e^- data at center-of-mass energy $\sqrt{s_{ee}}$ between 189 GeV and 209 GeV to set limits on the production of eq-resonant states [18]. The cross-section excluded at the 95% confidence level, σ_{95}, resulting from these calculations is shown in Fig. 2.13 for scalar and for vector leptoquarks.

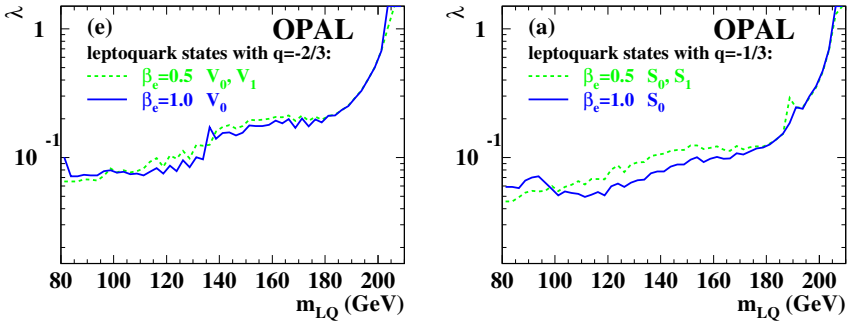

Figure 2.13: OPAL measurements of the 95% confidence level upper limits on the coupling constant λ for single production of the scalar and vector leptoquark states for branching fractions $\beta_e = 0.5$.

$p\bar{p}$ limits

At hadron colliders leptoquarks can be produced in pairs by gluon–gluon fusion and quark–antiquark annihilation, as shown in Fig. 2.14, or singly from photons radiated from the (anti)proton beam when a virtual lepton interacts with a quark from the other beam, see Fig. 2.15.

The CDF and DØ experiments at the TEVATRON proton-antiproton collider have searched for LQ pair production through $eejj$ [19], $e\nu jj$ [20] and $\nu\nu jj$ [21] channels, where j represents the hadron jet of the quark from leptoquark decay. The measured 95% C.L. upper limits for production cross-sections in the $\nu\nu + jets$ channel as a function of leptoquark mass for scalar and vector leptoquarks are shown in Fig. 2.16.

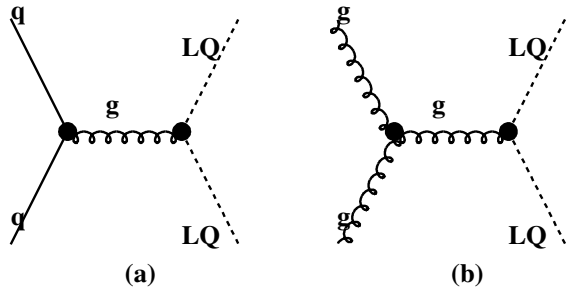

Figure 2.14: Feynman diagrams for leptoquark pair production at hadron colliders. The LQ pair is produced from the gluon, which is generated through quark-antiquark fusion (a) or through gluon-gluon fusion.

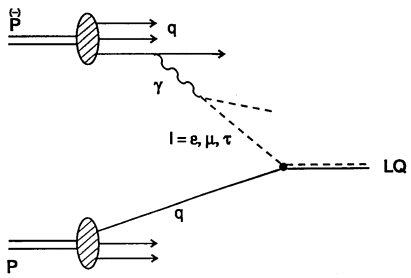

Figure 2.15: Schematic representation of the mechanism for producing single leptoquarks in proton–(anti)proton collisions.

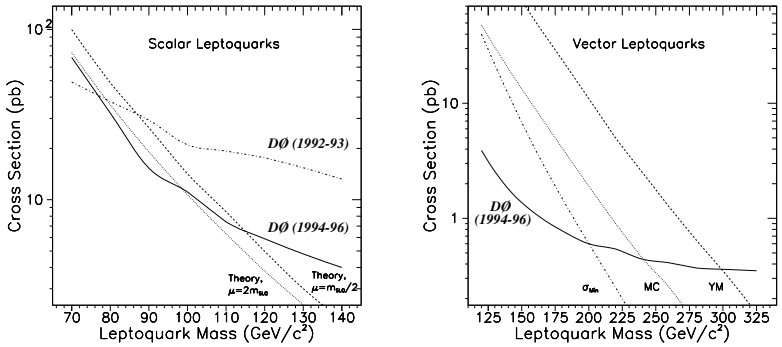

Figure 2.16: TEVATRON 95% C.L. upper limits on the production cross-section as a function of leptoquark mass, for scalar (left) and vector (right) leptoquarks, and different theoretical predictions. The LQ is assumed to decay exclusively to νq. The theoretical predictions correspond to the production of leptoquarks of a single generation, while the experimental limit corresponds to the sum of contributions from leptoquarks of all three generations.

ep limits

Leptoquark searches at HERA have been performed previously by ZEUS and H1. With ~ 130 pb^{-1} ep data collected from 1994 to 2000 ZEUS [23] and H1 [24] have studied the final state ej and νj invariant mass spectra. No resonant states were found and both collaborations set similar limits on the coupling constant λ as a function of leptoquark mass as shown in Fig. 2.17

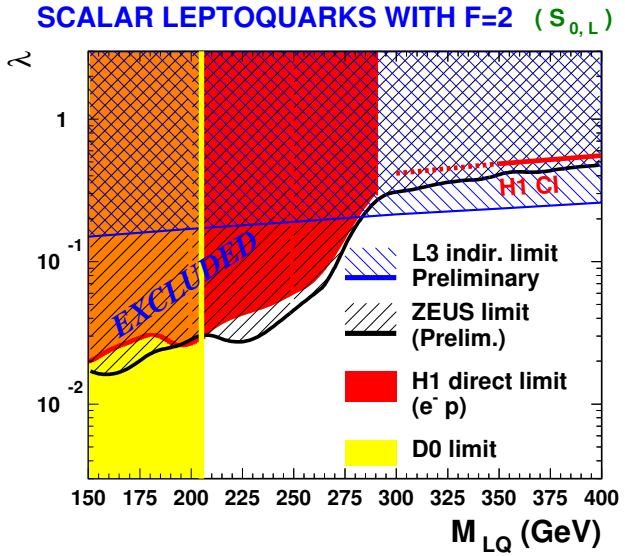

Figure 2.17: Limits on the coupling $\lambda_{\rm lim}$ for an S_0^L LQ in the (M_{LQ}, λ) plane. The excluded region lies above the curves for H1,L3 and ZEUS and to the left of the line for D0.

Table 2.6 shows combined LEP limits together with H1 and ZEUS limits for S_0^L, S_1^L, V_0^L, V_1^L BRW leptoquarks [27] in the limit of large LQ masses, $M_{LQ} \gg \sqrt{s}$.

Table 2.6: Lower limits on M_{LQ}/λ (TeV^{-1}).

LQ type	LEP	L3	H1	ZEUS
S_0^L	2.09	1.20	0.72	0.75
S_1^L	1.15	0.86	0.48	0.55
V_0^L	2.93	1.78	0.77	0.69
V_1^L	2.10	1.67	1.38	1.42

Anomalies in the 94-97 HERA data

In 1997, ZEUS and H1 reported an excesses of high Q^2 ($\gtrsim$ 10000 GeV^2) neutral current events with respect to SM expectations as shown in Table 2.7.

Table 2.7: Number of observed and expected events from H1 and ZEUS. The last column gives the probability that the expected NC DIS signal fluctuates to values equal to or larger than the number of observed events.

Q^2 cut (GeV^2)	H1 data	H1 NC_{exp}	ZEUS data	ZEUS NC_{exp}	H1 + ZEUS data	H1 + ZEUS NC_{exp}	P N > N_{obs}
$Q^2 > 10000$	20	18.3± 2.4	33	32.2 ± 2.0	53	50.5 ± 3.1	0.37
$Q^2 > 15000$	12	4.71± 0.76	12	8.66 ± 0.66	24	13.4 ± 1.0	0.0074
$Q^2 > 20000$	5	1.32± 0.27	5	2.76 ± 0.24	10	4.08 ± 0.36	0.010
$Q^2 > 25000$	3	0.51± 0.16	3	1.01 ± 0.09	6	1.52 ± 0.18	0.0053
$Q^2 > 30000$	2	0.23± 0.05	2	0.37 ± 0.04	4	0.60 ± 0.06	0.0035
$Q^2 > 35000$	0	0.08± 0.04	2	0.15 ± 0.01	2	0.23 ± 0.04	0.023

During the running period 1994-1997 at HERA, the H1 collaboration collected ~ 37 pb^{-1} of e^+p data. A slight excess was found in the H1 data in neutral current channel at mass ~ 200 GeV (or $x \sim 0.45$) [28]. Within the mass window of 200 ± 12.5 GeV, 8 events were observed while 2.87 ± 0.48 are expected from the Standard Model. Fig. 2.18 shows for the H1 NC selection the measured Q_e^2 distribution in comparison with the expectation from standard NC DIS processes. Also shown is the ratio of the Q_e^2 distribution to the NC DIS expectation. H1 has announced its findings in the 94-97 $e^+p \to \nu X$ charged current channel, where 3 events at $Q^2 > 20000$ GeV^2 with an expectation of 0.74 ± 0.39, but no events with $Q^2 > 25000$ GeV^2, were found.

During the same running period, the ZEUS collaboration collected ~ 47.7 pb^{-1} of e^+p data. A small excess was found in neutral current channel at $M_{ej} \sim 230$ GeV. Above $M_{ej} = 210$ GeV, 49 events were observed while 24.7 ± 5.6 were expected from the SM. The M_{ej} spectrum for events with $M_{ej} > 100$ GeV and predicted number of events (N^{pred}) from NC processes is also shown in Fig. 2.19. The ratio of the measured mass spectrum to the expectation is shown in Fig. 2.19 (b). The shaded band indicates the systematic uncertainty on the expectations. It was concluded that this excess was not due to any effect of the detector response or Monte Carlo simulation. No excess was observed by ZEUS collaboration in the charged current $e^+p \to \nu X$ channel.

In the more recent $ep \to eX$ data no similar excess is seen and the excess in the earlier data sample is attributed to a statistical fluctuation. The increase in the proton beam energy from 820 to 920 GeV in 1998 had no significant effect on the mass reconstruction.

Additional $ep \to \nu X$ data at high $\sqrt{s}$ will allow any excess in the charged current channel to be revisited.

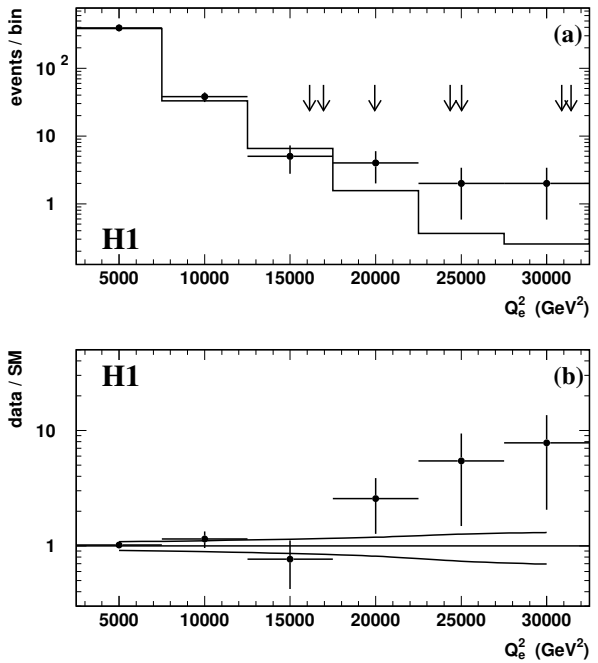

Figure 2.18: (a) Q_e^2 distribution of the selected NC DIS candidate events for the data (•) and for standard NC DIS expectation (histogram); the arrows indicate the Q_e^2 values for data entries with $Q_e^2 > 15000$ GeV^2 and $M_e > 180$ GeV; (b) ratio of the observed and expected number of events as a function of Q_e^2.

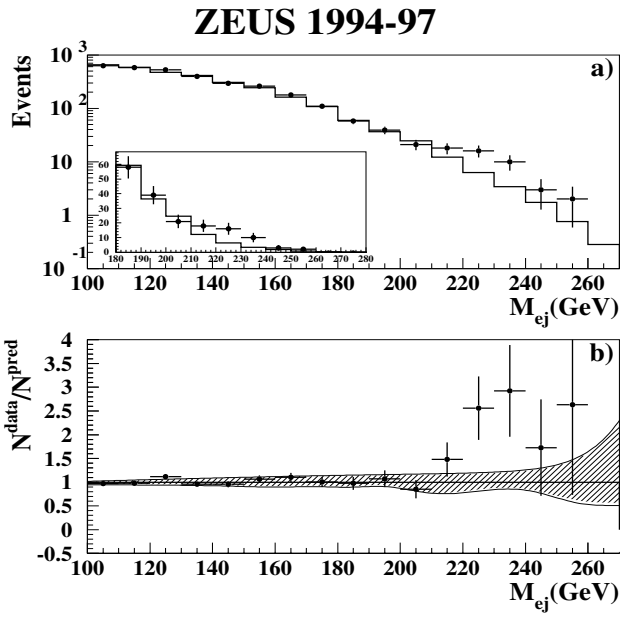

Figure 2.19: a) Comparison of observed events (•) and SM expectations (histogram) as a function of the reconstructed e^+-jet invariant mass. The inset shows the region with $M_{ej} > 180$ GeV on a linear scale. b) The ratio of the number of observed events to the Standard Model expectations and the SM uncertainty.

2.6 Missing transverse momentum as a signature for new physics

One important goal of the HERA collider is the search for new physics beyond the Standard Model. There are predictions by a large variety of extensions to the SM which are expected to be observable in large momentum transfer events. Events with large missing transverse momenta (P_T^{mis}) in the final state appear in many theories beyond the Standard Model, e.g LQ with $LQ \to \nu q$. Some of them are briefly described below:

2.6.1 Excited fermions

The existence of exited leptons or quarks would provide compelling evidence for a new layer of fermion structure predicted within theories of compositeness. At HERA single excited electrons, quarks and neutrinos can be produced via processes $ep \to f^*X$, $f^* \to fV$ shown in Fig. 2.20. They have a neutrino in the final state. The f^* decay modes which have been studied by ZEUS and the subsequent decay channels of the heavy boson are listed in Table 2.8. A detailed description of the analysis is given in [32].

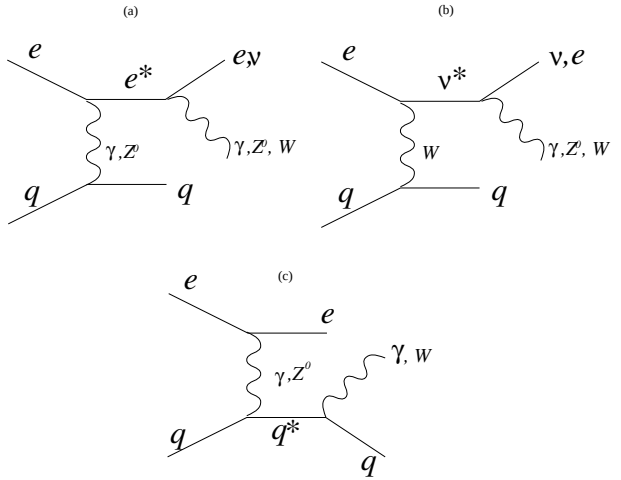

Figure 2.20: Feynman diagram for excited (a) electron, (b) neutrino and (c) quark production at HERA.

f^*	Final states		
e^*	$e\gamma$	eZ^0 $\rightarrow eq\bar{q}$ $\rightarrow e\nu\bar{\nu}$	νW $\rightarrow \nu q\bar{q}$ $\rightarrow \nu e\nu$
ν^*	$\nu\gamma$	νZ^0 $\rightarrow \nu q\bar{q}$	eW $\rightarrow eq\bar{q}$ $\rightarrow ee\nu$
q^*	$q\gamma$	qW $\rightarrow qe\nu$	

Table 2.8: The f^* decay modes and subsequent final states.

2.6.2 Selectrons and Squarks

Supersymmetry (SUSY) is presently considered to be a promising candidate for a theory beyond the standard model. While there is strong theoretical motivation for its existence, there is currently no experimental evidence to support its prediction that each SM particle has a supersymmetric partner differing by a half-unit of spin.

Within the minimal supersymmetric standard model (MSSM) it is assumed that R-parity is conserved. This implies that SUSY particles can only be produced in pairs and that the lightest SUSY particle (LSP), taken here to be the lightest neutralino χ_1^0 is stable and weakly interacting thereby escaping detection.

At HERA the dominant MSSM process is the production of a selectron and squark via t channel neutralino exchange $ep \rightarrow \tilde{e}\tilde{q}X$ as shown in Fig. 2.21. Although the $\tilde{e}$ and $\tilde{q}$ can decay into any lighter gaugino and their SM partners, the cleanest experimental signature involves both the $\tilde{e} \rightarrow e\chi_1^0$ and $\tilde{q} \rightarrow q\chi_1^0$ decays and is the one considered here. The final state topology consists therefore of an electron which is acoplanar to the hadronic system and missing momentum. Limits from a earlier search using the ZEUS detector and an

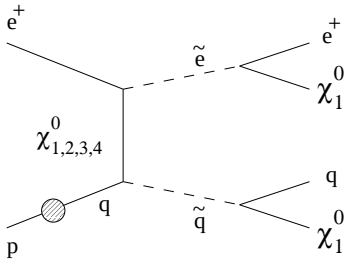

Figure 2.21: Selectron-squark production via neutralino exchange and the following decays to the LSP and SM partner.

integrated luminosity of 46.6 pb^{-1} have been published [34].

2.6.3 Search for R-parity violating squarks

R-parity violating squarks can be singly produced as an s channel resonance up to the kinematic limit of $\sqrt{s}$ via positron-quark fusion. The squarks subsequently decay into fermions, or quark and neutralino, or a chargino as shown in Fig. 2.22.

In the first case where the squarks decay into fermions the final state signature consist of a lepton and a jet and are indistinguishable from standard neutral and charged current deep inelastic scattering on an event-by-event basis. The strategy then involves searching for a resonance at high mass ($M_{\tilde{q}} = \sqrt{xs}$) where x is the Bjorken scaling variable.

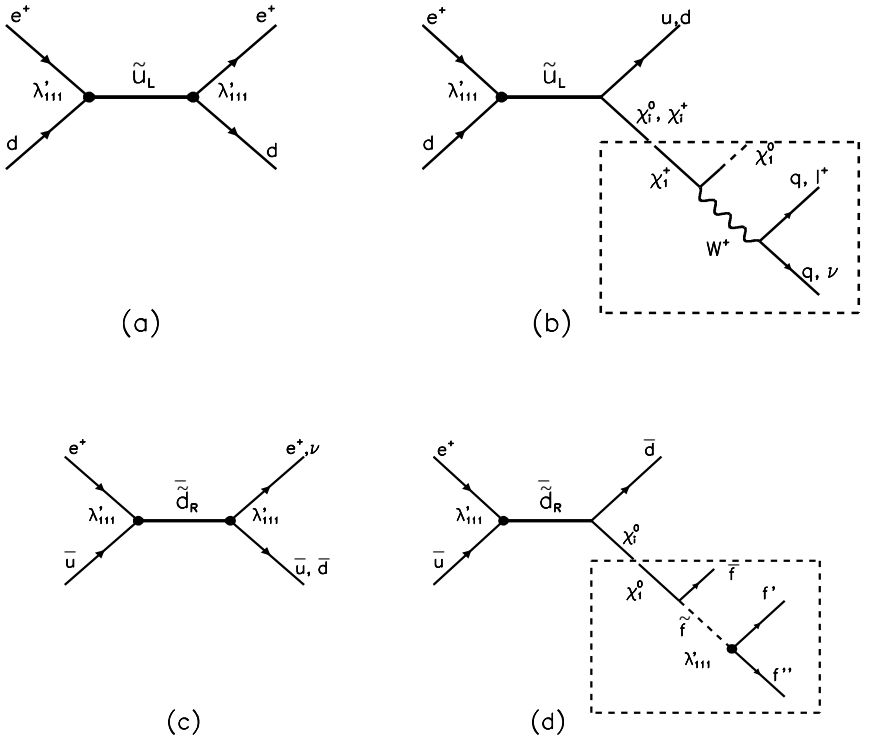

Figure 2.22: First generation R-parity violating squark production at HERA followed by (a), (c) R-parity violating decays and (b) and (d) gauge decays. In (b) and (d) the chargino and neutralino undergo subsequent R-parity violating decays.

Squark decays via gauge couplings $\tilde{u}_L \rightarrow u\chi_i^0$ or $d\chi_j^+$ and $\bar{\tilde{d}}_R \rightarrow \bar{d}\chi_i^0$ have also been

considered, see Fig. 2.22 (b) and (d). The final state of the process (b) would consist of (P_T^{mis}+ multiple jets) or (electron + jets) depending on the W^+ decay mode. They could also have (P_T^{mis} + two electrons + multiple jets) or (P_T^{mis} + electron + multiple jets) depending on the W^+ and χ_1^0 decay mode. The final state signatures of the process (d) might consist of (P_T^{mis} + electrons + jet) or (P_T^{mis} + two electron + jet) or (P_T^{mis} + 3 jets) depending on the χ_1^0 decay mode, full details are given in [35].

Possible processes containing a neutralino (χ^0) or gravitino ($\tilde{G}$) in the final state are shown in Fig. 2.23. Neutralinos and gravitinos are particles which could be stable and could traverse the detector without interaction. Fig. 2.23 (a) and (b) show the R-parity violating processes of selectron exchange. The signature of both processes is the existence of a jet and P_T^{mis}. The invariant mass of jet and χ^0 will not give a resonant peak at the position of the selectron mass because of u-channel selectron exchange, but a tail in the mass spectrum or in the missing P_T spectrum will appear.

The signature of the processes (c) and (d) is an electron and P_T^{mis}. In process (d) a resonant peak at the position of selectron mass in the invariant mass spectrum of electron and one of the two gravitinos would be expected. This peak cannot be reconstructed directly because a second gravitino also escapes detection. Instead a tail in the large mass region of the invariant mass spectrum and in the P_T^{mis} distribution should be visible.

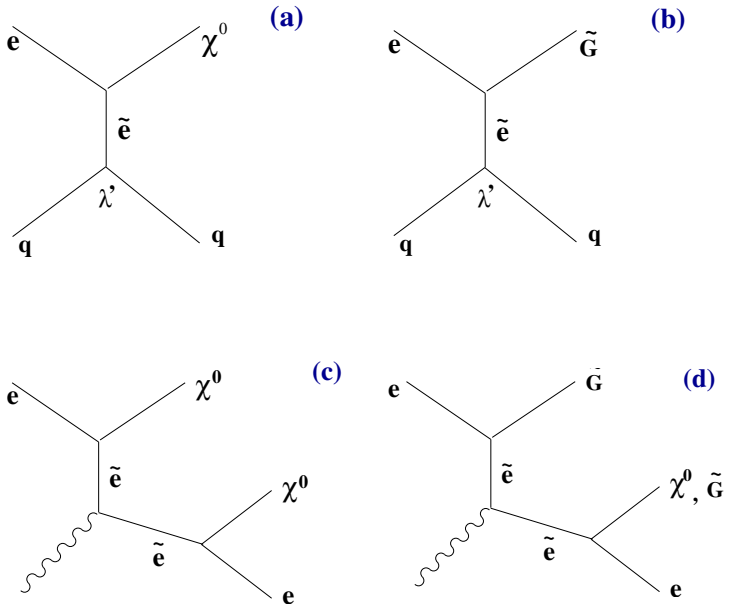

Figure 2.23: Feynman diagram with neutralino and gravitino in the final state.

2.6.4 Other exotic processes with missing transverse momentum in the final states.

A model-independent search might be able to discover unexpected manifestations of new physics and give an answer to the important question if new physics signal might be hidden in HERA data. Such a model independent search was presented earlier by the D0 collaboration [30] and H1 collaboration [31]. All possible event topologies involving electrons, neutrino and jets with high transverse momenta have been investigated. Events are classified into exclusive channels according to their final state. To search for deviations between data and SM expectation the invariant mass distributions were investigated.

Chapter 3

HERA and ZEUS

3.1 The Hadron-Electron Ring Accelerator

The Hadron-Electron Ring Accelerator (HERA) is the first collider designed to collide protons and electrons. It was built at the Deutsches Electronen-Synchrotron (DESY) in Hamburg, Germany, during the years 1984-91 and started luminosity running in 1992.

Two separate storage rings for protons and electrons are placed in a 6.34 km long tunnel 10 to 25 meters underground. The proton and electron (or positron) bunches are accelerated to 920 GeV and 27.5 GeV, respectively, and circulate in opposite directions.

Protons are produced by stripping electrons from hydrogen and are accelerated up to 50 MeV in the Linear Accelerator (LINAC). They are then injected into the DESY-III accelerator ring and accelerated up to 7.5 GeV. Before being transfered to the HERA ring, protons are injected into PETRA (Positron-Electron Tandem Ring Anlage), where they are accumulated in 60 bunches and accelerated to 40 GeV. In HERA proton bunches are accelerated to their final energy up to 920 GeV with a beam lifetime of several days.

Electrons, produced at a cathode, are injected in to the LINAC-I and then passed into LINAC-II where they are accelerated first up to 220 MeV and then to 450 MeV. Positron Intensity Accumulator (PIA) is then filled with a single bunch with electron current up to 60 mA. The bunch is transfered to DESY-II and accelerated up to 7.5 GeV. Then PETRA-II is filled with 42 bunches of electrons with 96 ns spacing. After accelerating the electrons up to 11 GeV they are transfered to HERA, where they are accelerated up to 27.5 GeV with a typical beam lifetime of $\sim$ 15 hours.

HERA beam optics foresees 220 e and p bunch slots. During normal operation 180 bunches are filled and collide producing ep luminosity. The remaining 30 bunches are empty or filled with e or p, which allows empty or single beam type investigations of trigger rates, etc. to be performed.

The principle HERA design parameters and machine performance as a function of running period are shown in Table 3.1.

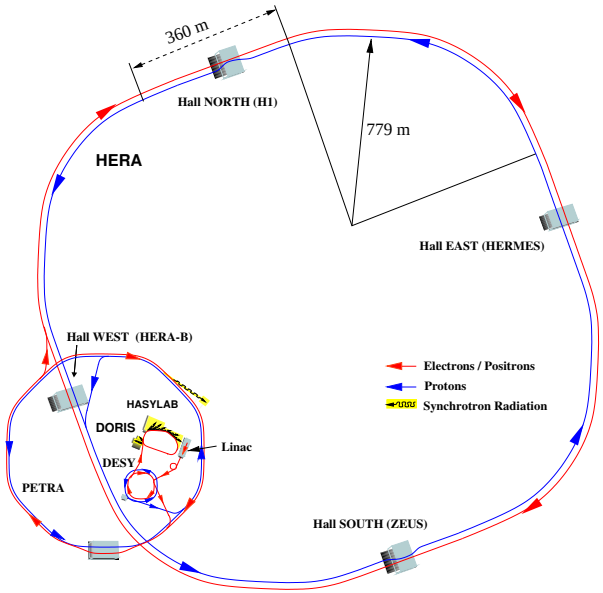

Figure 3.1: A schematic showing the layout of HERA.

Four experiments are installed in the HERA ring. For two of these experiments, H1 in the north and ZEUS in the south halls, proton and electron beams are brought into collision at zero crossing angle. The HERMES experiment uses electrons and HERA-B uses protons only. The integrated luminosity measured by ZEUS as a function of days of running are shown in Figs. 3.2- 3.3.

Table 3.1: HERA design parameters and performance evolution as a function of running period.

HERA parameters	Design values		1994-1997 running period		1998-2000 running period		2002-present running period	
	p	e^-	p	$e^\pm$	p	$e^\pm$	p	e^+
Energy (GeV)	820	30	820	27.5	920	27.5	920	27.5
Instantaneous luminosity ($cm^{-2}s^{-1}$)	$1.5 \cdot 10^{31}$		$1.4 \cdot 10^{31}$		$9.9 \cdot 10^{29}$		$2.5 \cdot 10^{31}$	
Specific luminosity ($cm^{-2}s^{-1}(mA)^{-2}$)	$3.4 \cdot 10^{29}$		$7.6 \cdot 10^{29}$		$1.8 \cdot 10^{30}$		$1.6 \cdot 10^{30}$	
Integrated luminosity (pb^{-1})	–		48.6		83.01		24.5	
Current (mA)	160	58	105	43	99	48	100	43
Number of bunches	210		176 + 5	176 + 20	174 + 6	174 + 15	173 + 7	173 + 7
Beam σ_x (mm) at IP	0.27	0.25	0.2	0.2	0.2	0.2	0.11	0.11
Beam σ_y (mm) at IP	0.08	0.08	0.05	0.05	0.05	0.05	0.03	0.03
Beam σ_z (mm) at IP	110	8	110	8	110	8	110	8
Center-of-mass energy, GeV	314		300		318		318	

Table 3.2: HERA luminosity written to tape at ZEUS.

Year	Mode	E_e (GeV)	E_p (GeV)	$\mathcal{L}(pb^{-1})$	$\delta\mathcal{L}/\mathcal{L}(\%)$
1993	e^-p	26.7	820	0.55	-
1994	e^-p	27.5	820	0.28	1.5
1994-1997	e^+p	27.5	820	48.32	1.5
1998-1999	e^-p	27.5	920	16.71	1.8
1999-2000	e^+p	27.5	920	66.30	2.25
2002-now	e^+p	27.5	920	15.	3.

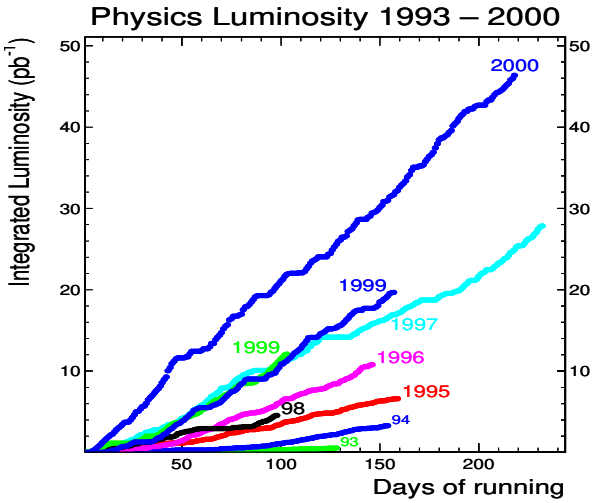

Figure 3.2: Integrated luminosity per running period measured by ZEUS in 1993-2000 as a function of days.

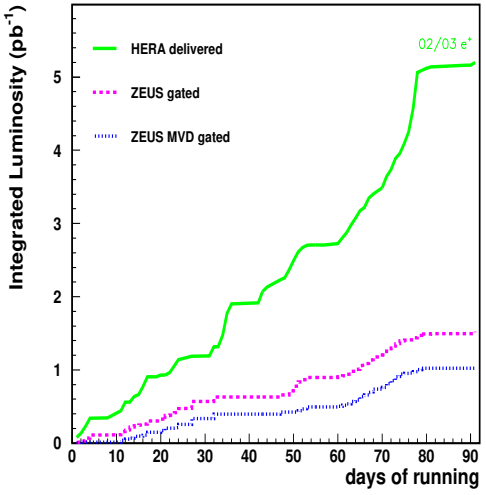

Figure 3.3: Integrated luminosity measured by ZEUS in 2002-2003 as a function of days of running.

3.2 ZEUS detector

The ZEUS collaboration consists of approximately 350 physicists from 55 institutes in 13 countries.

The experiment [36] is a general purpose detector designed to study all aspects of lepton-proton scattering. The detector is essentially hermetic covering almost the entire 4π solid angle with the exception of small regions around the beampipe. Longitudinal and transverse sections of the detector are shown in Figures 3.4 and 3.5, where Table 3.3 defines the acronyms used for the different components of the detector.

Table 3.3: The acronyms used for the different component of the ZEUS detector.

BAC	Backing Calorimeter
BCAL	Barel Calorimeter
BMUON	Barel Muon Chambers
CTD	Central Tracking Detector
FCAL	Forward Calorimeter
FDET	Forward Tracking Detector
FMUON	Forward Muon Chambers
RCAL	Rear Calorimeter
RMUON	Rear Muon Chambers
RTD	Rear Tracking Detector
UCAL	Uranium Calorimeter

The ZEUS coordinate system is defined as a right handed orthogonal system with origin ($x = y = z = 0$) at the nominal interaction point (IP). The X-axis points towards the center of the HERA ring, the Y-axis points upwards and the Z-axis is given by the proton beam direction. For analysis a polar coordinate system (R, θ, ϕ) is used, where R is the distance to the nominal interaction point, θ is the polar angle measured with respect to the z-axis and ϕ is the azimuthal angle measured with respect to the x-axis. Kinematically the forward region of the detector is at low θ. For analysis the pseudorapidity η defined by:

$$\eta = -\log\left(\tan\frac{\theta}{2}\right) \tag{3.1}$$

is usually used instead of the polar angle θ.

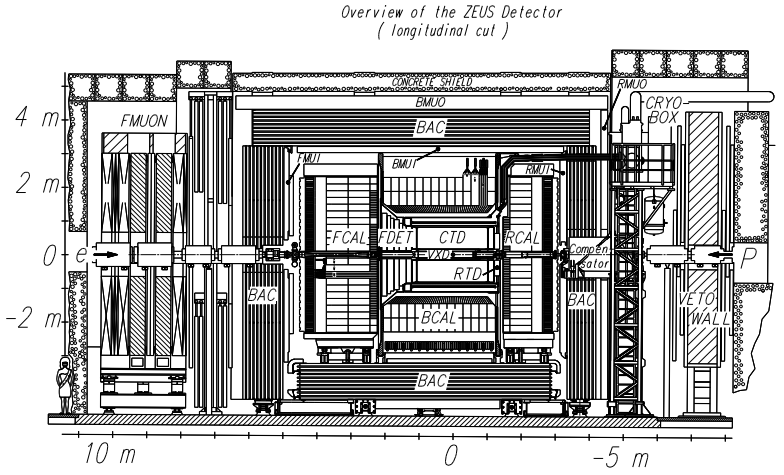

Figure 3.4: x-z view of ZEUS detector.

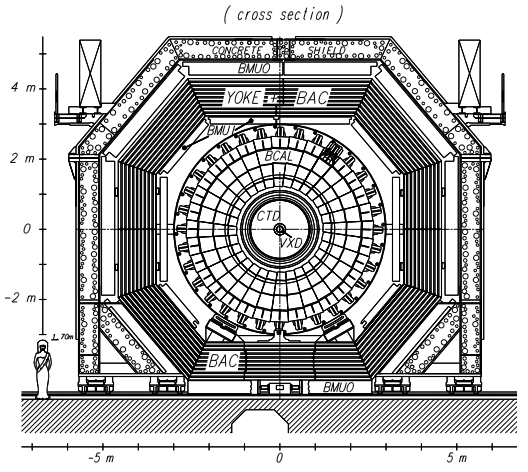

Figure 3.5: x-y view of ZEUS detector.

Starting from the interaction point and moving radially outwards the major ZEUS detector components are described briefly as follows. The innermost component in the ZEUS detector was a Vertex Detector (VXD), removed during the 1995/1996 shutdown and replaced by the silicon Micro Vertex Detector (MVD) installed in spring 2001. Therefore, in the period 1996-2000, the Central Tracking Detector (CTD) was the nearest component to the IP. It is complemented by Forward and Rear Tracking Detectors (FTD,RTD). To allow charge and momentum determination the tracking detectors are surrounded by a super-conducting solenoid providing a magnetic field of 1.43 T. Outside the superconducting magnet lies the ZEUS calorimeter system used for energy measurements. The system consist of two parts, a depleted uranium scintillator calorimeter (UCAL) installed inside the iron of the field return yoke and a chamber based Backing Calorimeter (BAC) installed inside the segmented iron return yoke. Muon identification chambers (limited streamer tubes) are mounted inside (FMUI, BMUI, RMUI) and outside (FMUON, BMUON, RMUON) the BAC.

The detector components most relevant to this analysis are described in detail below.

3.2.1 The central tracking detector

The Central Tracking Detector (CTD) is a cylindrical wire drift chamber used to measure the direction and momentum of charged particles and estimates their energy loss dE/dx for particle identification. The chamber has an overall length of 241 cm, an outer radius of 85 cm and an inner radius of 16 *cm*. The active volume ranges from $Z = -100$ cm to $Z = 105$ cm with inner and outer radii of 18.2 cm and 79.4 cm, resulting in a polar angular coverage of $15^o < \theta < 164^o$. The CTD consists of 72 radial layers of sense wires which

Table 3.4: The Central Tracking Detector.

	Theta	η
CTD	$15 < \theta < 164$	$2.04 > \eta > -1.96$

are arranged into 9 superlayers (SL) with 576 drift cells. Each cell has 8 sense wires. The odd superlayers have wires parallel to the beam axis while the even superlayers have small angle ($\pm 5^o$) stereo wires allowing the determination of the z-position of the hits. Fig. 3.6 shows the layout of one of the CTD octants. The three inner axial layers are equipped with z-by-timing electronics which determine the z-position of a hit from the difference in arrival times of a pulse at both ends of the chamber. This is used for trigger purposes. The CTD has a total of 4608 sense wires (30 μm thick) and 19584 field wires and is filled with an argon (Ar), carbon dioxide (CO_2) and ethane (C_2H_6) gas mixture in the ratio $83 : 5 : 12$. Before injection into the chamber the gas mixture is bubbled through ethanol.

A charged particle, traversing the CTD, ionizes the gas, creating electron-ion pairs along its trajectory. Avalanche multiplication occurs in the field of sense wires with an amplification factor of $\sim 10^4$.

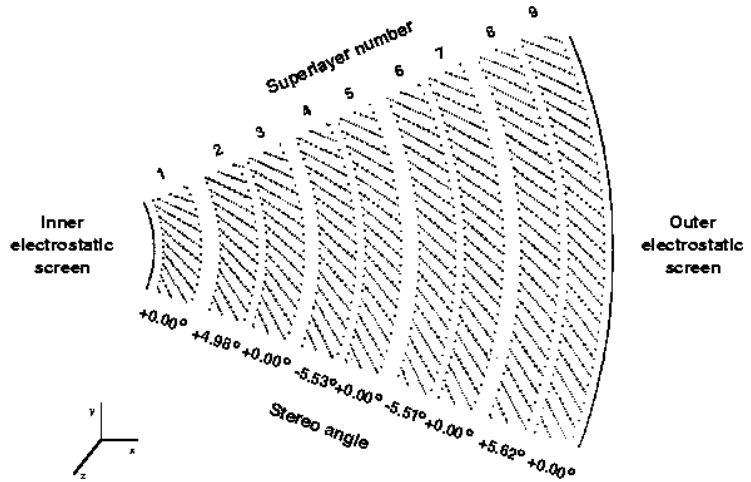

Figure 3.6: An octant of CTD with the wire structures.

The transverse momentum of the track is measured using its curvature:

$$p_T[GeV] = 0.2998 \cdot B[T] \cdot r[m] \tag{3.2}$$

together with the z position, derived from the stereo wire measurements, allows the total momentum to be determined:

$$p = p_T / \sin\theta. \tag{3.3}$$

The resolution of the measurements depends on the number and precision of hits, and on the contribution from multiple scattering. For tracks which traverse all superlayers the resolution is:

$$\frac{\Delta p_T}{p_T} = 0.58\% \cdot p_T[GeV] \oplus 0.65\% \oplus \frac{0.14}{p_T}[GeV]. \tag{3.4}$$

The first term accounts for the position resolution of the hits, the second term for the multiple scattering particles suffers inside the CTD, and the last for the scattering before the particle enters the CTD. The position resolution for a single track is $\sim 200\mu$m in the $r\phi$-direction and depends on the polar angle of the track. In the z-direction, the position resolution measured by the stereo wires is $1.0 - 1.4$ mm.

3.2.2 The uranium calorimeter(CAL)

The calorimeter is designed to be hermetic, to cover as much of the solid angle as possible, and to be compensating, i.e. have equal signal response to electromagnetic and hadronic particles ($e/h = 1$). Figure 3.7 shows a side view of CAL together with the CTD and SOLENOID.

The ZEUS calorimeter is divided into three part: Barrel Calorimeter (BCAL), Forward Calorimeter (FCAL) and Rear Calorimeter (RCAL) whereby the longitudinal segmentation of the parts is identical. The inner segment, closest to the IP, constitutes the Electro-Magnetic Calorimeter (FEMC, BEMC, REMC) with a depth of $\sim 25X_0$ ($\sim 1\lambda$) and the outer part is called the Hadronic Calorimeter (HAC). The hadronic section in FCAL and BCAL is further subdivided into the HAC1 and HAC2 sections (depths 2 and 3λ). In the RCAL there is only one hadronic section with depth 3λ. The forward-backward asymmetry of the calorimeter was chosen to account for the large forward-backward asymmetry of the ep final state due to the different energies of the incoming electrons and protons. Details of the calorimeter are given in Table. 3.5. Each calorimeter cell is read out

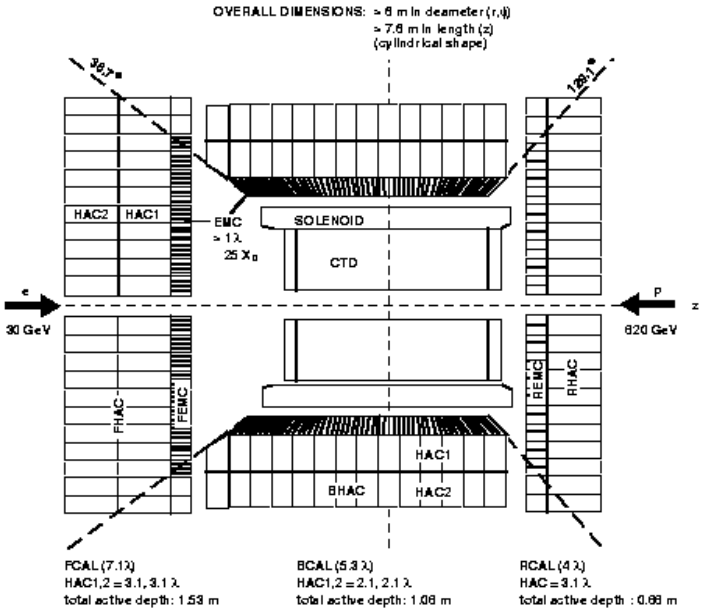

Figure 3.7: A side view of the calorimeter.

on opposite sides by two Photomultiplier Tubes (PMTs) coupled to the scintillators via wavelength shifters. Comparison of the two PMT signals allows the determination of the

Table 3.5: Parameters of the uranium calorimeter.

	FCAL	BCAL	RCAL
Theta	$2.2 < \theta < 39.9$	$36.7 < \theta < 129.1$	$128.1 < \theta < 176.5$
η	$4.0 > \eta > 1.0$	$1.1 > \eta > -0.74$	$-0.72 > \eta > -3.49$
Number of modules	23	32	23
Number of towers per module	11-23	14	11-23
Number of cells	2172	2592	1152
Length cm	152.5	105.9	87.0
Radiation length X_0	25.9	24.6	24.3
Absorption lengths λ	7.14	4.92	3.99

impact point of the particle within a cell.

The calorimeter performance measured in test beam is for hadrons:

$$\frac{\sigma_h(E)}{E} = \frac{35\%}{\sqrt{E}} \oplus 2\% \tag{3.5}$$

and for electrons:

$$\frac{\sigma_e(E)}{E} = \frac{18\%}{\sqrt{E}} \oplus 1\% \tag{3.6}$$

where E is the incident beam energy in GeV. The ratio between pulse heights of electrons and of hadrons, e/h, is measured to be

$$e/h = 1.00 \pm 0.03 \tag{3.7}$$

The timing resolution is less then 1 ns for energy deposits greater than 4.5 GeV.

The analysis presented in this thesis does not use results from the backing calorimeter.

3.2.3 C5 detector

A large number of background events in the ZEUS detector come from interactions of beam particles with gas molecules within the beam pipe. The C5 detector is a set of scintillation counters placed very close to the beam pipe which allows the rate and arrival times of halo particles accompanying both beams to be measured. This information is essential to the operation of ZEUS and is described in detail in the next chapter.

3.2.4 The luminosity monitor

The luminosity is defined as:

$$L = \frac{N}{A\sigma}, \tag{3.8}$$

where N is the event rate of a process, A is acceptance and σ its cross section. For the luminosity determination N is measured and σ has to be known very precisely from theory. The process should be chosen such that its detection is easy and the rate is high. At the HERA collider, the process used by ZEUS and H1 for luminosity measurement is the bremsstrahlung process:

$$ep- > e'p\gamma. \tag{3.9}$$

The cross-section of this processes is given by the Bethe-Heitler formula [59]:

$$\frac{d\sigma_{BH}}{dk} = 4\alpha r^2{}_e \frac{E'}{kE}\left(\frac{E}{E'} + \frac{E'}{E} - \frac{2}{3}\right)\left[\ln\left(\frac{4E_pEE'}{m_pm_ek}\right) - \frac{1}{2}\right], \tag{3.10}$$

where:
k -photon energy,
E, E'- primary and secondary electron energy,
E_p- proton energy,
m_p, m_e- mass of proton and electron,
α - fine structure constant, and
r_e-classical radius of electron.

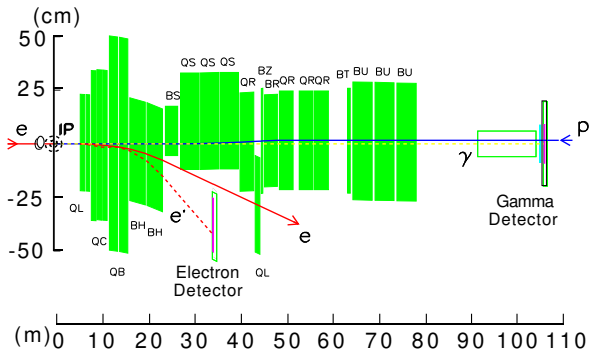

Figure 3.8: Schematic layout of the LUMI detector's γ- calorimeter and e-calorimeter.

The layout of the luminosity monitor is shown schematically in Fig. 3.8 [37]. The lead/scintillator sandwich γ and e calorimeters are located 108 m and 35 m, respectively, away from the ZEUS experiment in the HERA tunnel. The statistical error on the luminosity measurement is negligible, the systematic error is typically $\sim 2\%$.

3.2.5 Trigger and data acquisition system

The short repetition time ($\sim$ 96 ns) between bunch crossings at HERA (equivalent to a rate of approximately 10 MHz) defines the requirements for the trigger and data acquisition system. The rate of ep events is the order of few Hz, while the background

rate exceeds the rate of physics events by several orders of magnitude. The interactions of electrons or protons of the beam with the gas or elements from the beamline occur typically at a rate of $10 - 100$ kHz and the cosmic muon rate is approximately 0.5 Hz.

A three level trigger system is used to select ep physics events efficiently while reducing the rate to a few Hz. A schematic diagram of the ZEUS trigger system is shown in Fig. 3.9.

The First Level Trigger (FLT) is a hardware trigger, designed to reduce the input rate below 1 kHz. Each detector component has its own FLT interface, which stores the data in a pipeline, and makes a trigger decision within 2 μs after the bunch crossing. The decision from the local FLTs are passed to the Global First Level Trigger (GFLT), which decides whether to accept or reject the event and returns the decision within 4.4 μs. At the 1 kHz GFLT rate the GFLT dead time is $\sim 4\%$.

If the event is accepted, the data are transfered to the Second Level Trigger (SLT), which is software-based and runs on a network of Transputers. It is designed to reduce the rate from 1 kHz to 80 Hz. Each component can also have its own SLT, which passes a trigger decision to the Global Second Level Trigger (GSLT). The GSLT then decides whether to accept or reject the event. If the GSLT accepts the event it is then passed to the Event Builder.

The Event Builder collects data from all detector components into a single ADAMO [38] formatted event and transfers it to the Third Level Trigger (TLT), which makes a decision based on the complete information. The TLT is software-based and includes parts of the offline reconstruction code. The output rate of the TLT is between 5 and 20 Hz.

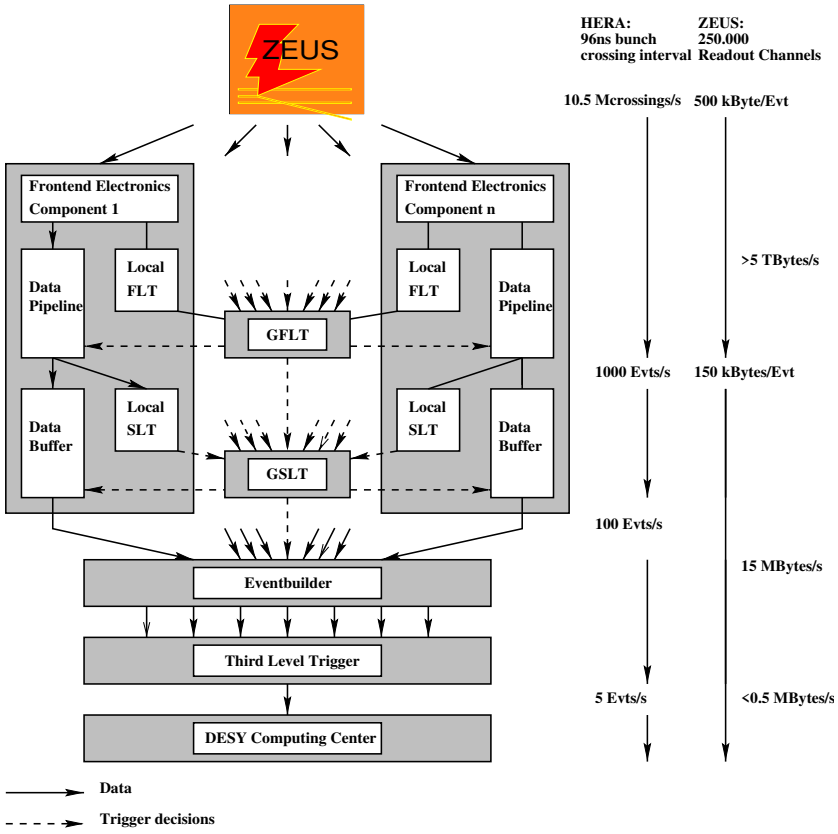

Figure 3.9: Schematic of the ZEUS trigger and data acquisition system.

Chapter 4

C5 Detector

In this chapter the C5 detector as implemented in August 2001 is described. The C5 detector is a scintillator tungsten sandwich counter positioned next to the beampipe with the task of measuring rate and arrival times of halo particles accompanying the beams. The primary use of the C5 detector is:

- to provide hit information indicating the presence of halo particles which provides an indispensable VETO at the ZEUS GFLT to reduce background event rates.
- to provide rate and arrival time measurements (bunch occupancy, satellite bunch intensity, etc.) essential for monitoring and controlling HERA beam conditions at ZEUS.
- for calculating the Z-vertex position.

The C5 detector setup and data acquisition system are described followed by a review of important rate and time measurement calculations. The chapter is concluded by a description of C5 background studies. More detailed information can be found in Appendix A.

4.1 Detector setup

The C5 counter consists of eight ~ 3 mm thick SCFN36 [39] scintillator tiles mounted in pairs above ($X > 0$) and below and orthogonal to the beampipe (see Fig. 4.1). Each pair is located in a half octogonal tungsten housing which provides the necessary support for the scintillator and mounting profile to the beampipe. The inner position profile of the scintillator follows the beampipe cross-section and the outer profile is a 20 cm $\times$20 cm octagon as shown in Fig. 4.1, which also shows the tile numbering scheme. The light from tiles are summed such that each pair of tiles 1/2, 3/4, 5/6, and 7/8 form the readout

channel 2, 4, 1, and 3, respectively. The C5 detector is mounted at $Z = -1240$ mm with the scintillator tiles at offset ± 10 mm (see Fig. 4.2).

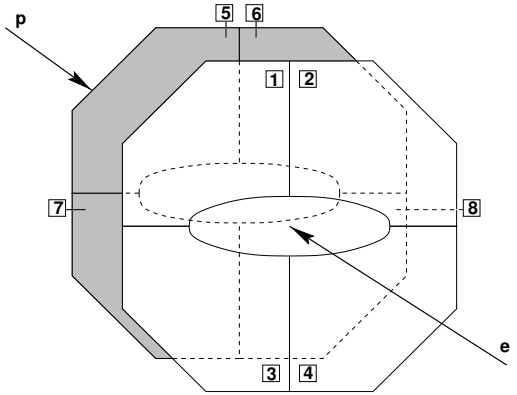

Figure 4.1: Arrangement of the 8 scintillator tiles of the C5 counter. The light from tiles are summed such that each pair of tiles 1/2, 3/4, 5/6, and 7/8 form the readout channel 4, 2, 3, and 1, respectively.

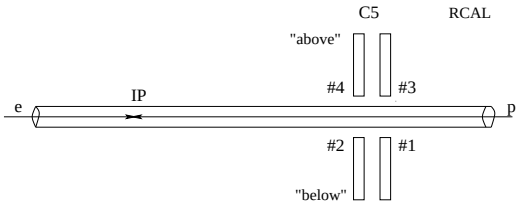

Figure 4.2: Diagram of C5 counter position and readout channel numbering.

Each scintillator tile is read out by seven wavelength shifter fibres stuck to the scintillator and optically coupled to light-guide fibers of length 2 m. Hamamatsu (R647) photomultipliers (PMTs), located on the bottom north yoke in front of RCAL, are used to readout the light signal.

The signals derived from the PMTs drive 58 m of RG58 coax cable to arrive at the signal distribution board in rack C-3-10 of the ZEUS experiment's electronics rucksack. Fig. A.4 details he allocation of space within the C5 readout racks.

Each PMT analog signal is faned out by a NIM/LeCroy 428F module to three signal processing branches:

1. Signal amplitude measurements (by Analog-to-Digital Converter C.A.E.N. V265).
2. Time and rate measurements (by Time-to-Digital Converters C.A.E.N. V488 and LeCroy 1176 and Scaler C.A.E.N. V260).
3. Signal for GFLT logic.

PMT high voltage is supplied by a Wenzel power supply located in Rack c-3-10 via 58 m coax cables. The high voltage settings used in 2001 are shown in Tab. 4.1.

Table 4.1: High voltage setting for photo multiplier in Aug 2001.

Channel	position	HV setting in Volt	Amplitude of signal at scope	Width of signal at scope
PMT1	p,below	1080	∼125 mV	∼50 ns
PMT2	e,below	1100	∼124 mV	∼50 ns
PMT3	p,above	1060	∼200 mV	∼50 ns
PMT4	e,above	1250	∼60 mV	∼75 ns

4.2 Data acquisition system

The C5 data acquisition system is based on commercial NIM (logic) and VME (TDC, ADC, etc. digitization) crate mounted modules detailed in A.3. A Motorolla VME single board computer (SCB) running LynxOS (Real Time operating System) is used to control and readout the DAQ system in polling mode. The information about hit rates, timing and pulse heights are filled into histograms which are available to users via histogram presenter tools (gplotter, hip, etc.) and the ZEUS online luminosity presenter (lumi-display). The histograms are also stored for further offline analysis.

The DAQ system is required to provide information continuously to HERA and other users, consequently it has been designed as standalone system running independently of the ZEUS experiments central DAQ. As a result of this the C5 system has its own data flow, described later, for recording measurements and only a summary of C5 information is appended to the ZEUS run summary.

The data acquisition program is written in C++. The general purpose library for VME modules are based on C++ object descriptions. This library with a uniform interface to modules helps to operate with the hardware VME modules in the main data taking program.

The main C5 Data Acquisition program consists of three independent tasks, implemented as threads.

The first thread reads scaler rates. The C5 detector provides background rates every 0.2 s. This process also sends all information (rates, ADC and TDCs histograms) to a DAQ server, running on Linux PC, over the network.

The second thread reads out C.A.E.N. ADC and 8-channel TDC modules, the later has a programmable full range between $90-770$ ns corresponding to resolution of $25-200$ psec. On receiving valid data the ADC or TDC modules are readout and the information is used to fill histograms.

The third thread reads out the 16-channels multihit LeCroy Time-to-Digital Converter (LeCroy TDC), which has a range of 65 μs with $1ns$ resolution, and stores timing information into the histograms. In order to measure short spikes of high rate the number of LeCroy TDC hits during one HERA revolution are counted. This method can provide measurements of rates up to 10 MHz (every HERA bunch crossing). The minimum rate which can be measured using this method is 40 kHz.

All histograms, except those with LeCroy TDC information, are reset after 10000 events or after 30 minutes (if small rates or no beam). Histograms with LeCroy TDC information are reset every 5 minutes. It is also possible to reset all histograms manually (see A.3.3).

4.3 C5 data flow

C5 measurements are permanently transferred to many end users (HERA, ZEUS, archive, etc) as shown schematically in Fig. 4.3. The dataflow and the processes used to control this are described below.

The C5 data flow consists of several processes (see Fig. 4.3):

- The DAQ program (process **"run.exe"**) runs on a LynxOS/Power PC. It collects C5 timing and amplitude information as well as rates for C5 and other components (CTD, RCAL, FCAL) and sends all histograms and rates to the DAQ-server over the network using TCP/IP communication protocol.
- The DAQ server program (**"c5daq-srv.exe"**) runs on a Linux/PC. It receives all ADC, TDC histograms and rates from the DAQ program and stores all information into shared memory.
- Independent programs running on the Linux/PC read data from the shared memory and, using client-server communication, send it to different clients like ZEUS histogram presenter for displaying histograms, to gplotter, NETMEX and others.

All TDCs and ADC histograms are sent every 30 s. The rate information is sent every 0.2 s.

Offloading data processing onto PCs allows the tight readout time requirements on the LynxOS machine to be performed.

More detailed information about the processes can be found in Appendix A.4.

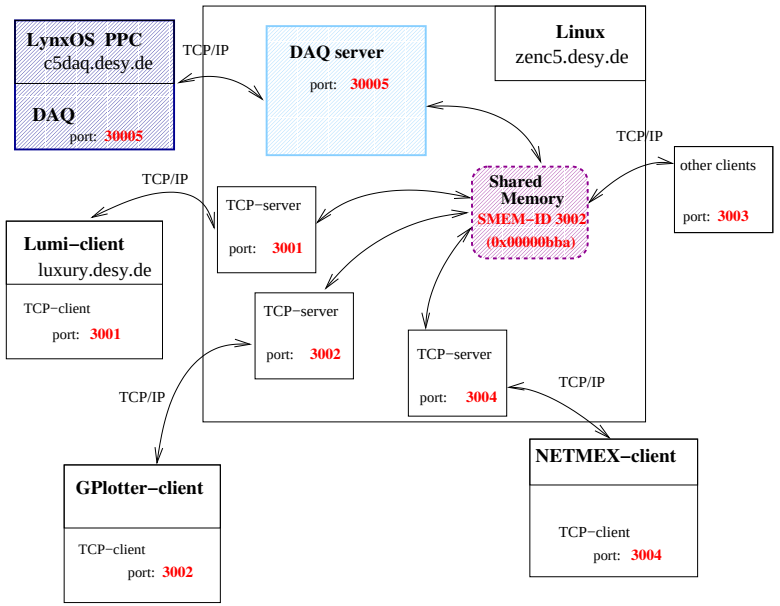

Figure 4.3: Main C5 data flow processes.

4.4 C5 detector timing resolution

A special logic chain is used to define C5 detector timing resolution. In this measurement a C.A.E.N. TDC works in common STOP mode using a coincidence of signals from photomultipliers 1 and 2 as the STOP signal. The START signal is provided by PMT1 and PMT2. By introducing the delay Δt_1 between PMT1 and PMT2 signals, (see Fig. 4.4) the coincidence signal from PMT1 and PMT2 will be produced at the same time as signal from PMT2. In the output TDC histograms from PMT2 a spike (delta-function) is seen in the position (Δt_2), where Δt_2 is a delay for the STOP signal. In the output TDC histogram from PMT1 the time distribution due to the jitter in the signals from PMT1 and PMT2 is seen. Additionally a delta-function, at position (Δt_2) is seen corresponding to the case when, delayed by Δt_1, the PMT2 signal arrives earlier than the signal from PMT1. The sigma of the distribution can be used to calculate the time resolution of the C5 detector:

$$\sigma_\Sigma \;=\; \sqrt{\sigma^2_{PMT1} \;+\sigma^2_{PMT2}} \tag{4.1}$$

From the measured distribution Fig. 4.5 one can see that FWHM $\sim$ 15 TDC counts or 2.64 ns (1 ns$\sim$ 5.68 counts or 1 count $\sim$ 0.178 ns).

$$\sigma_\Sigma \;=\; \frac{FWHM}{\sqrt{8\cdot\ln(2)}} \sim \frac{2.64}{2.35} \sim 1.1 \text{ ns} \tag{4.2}$$

$$\sigma_{PMT1} \;\sim \sigma_{PMT2} \sim \;\frac{\sigma_\Sigma}{\sqrt{2}} \sim \;\frac{1.1}{\sqrt{2}} \sim 0.8 \text{ ns} \tag{4.3}$$

For the timing measurements (see Appendix A.3.2 Fig. A.9) the time difference between the HERA 96 ns clock and the signal from the coincidence of PMT1 and PMT2 is used. The time resolution of the coincidence of two channels is slightly better than the resolution of the single channel. As an upper limit of the C5 resolution a single channel resolution can be used.

The length of e bunch $\sim$ 10 mm ($\sim$ 0.033 ns) is much smaller then the estimated C5 timing resolution. Therefore the e beam histogram can also be used to measure C5 timing resolution.

4.5 Interaction point determination using C5 time information

The difference in arrival time from the electron and proton HERA bunches at the position of the C5 detector can be estimated from:

$$T_{proton} - T_{electron} = \Delta T = \frac{2 \;\mid Z_{C5} \mid}{v} \simeq 8.3 \text{ ns}, \tag{4.4}$$

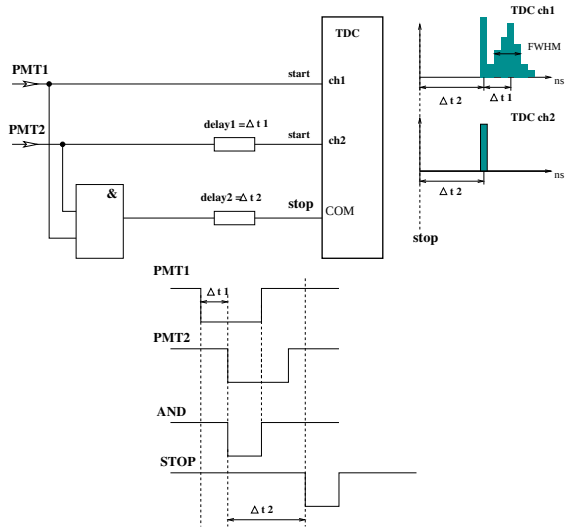

Figure 4.4: Setup for measurement of C5 detector timing resolution.

where $v \simeq c$ is velocity of the particles, which is approximately equal to the speed of light, and Z_{C5} is the Z position of the C5 detector in the ZEUS coordinate system. The value for the Z-position of the C5 detector is ~ -1240 mm with an uncertainty of 10 mm [39]. Here we assume that the e and p beam collide at the nominal interaction point $Z_{IP} = 0$.

The actual interaction region extends into both forward and rear directions from $Z_{IP} = 0$. Using timing information from the C5 detector we can estimate the real position of Z_{IP}.

The Z-position of electron-proton interactions in the ZEUS detector can be calculated from C5 times as follows:

$$Z_{IP} = \frac{(T_{proton} - T_{electron}) \cdot c}{2} - \mid Z_{C5} \mid \tag{4.5}$$

Using the C.A.E.N TDC the C5 detector can provide average time spectrum and the average position of Z_{IP}. Using the LeCroy TDC the C5 detector can provide timing and position of Z_{IP} for each bunch of particle at HERA cycle. The mean time value of the proton peak and the electron peak measured with the C.A.E.N. TDC as a function of time are shown in Fig. 4.6 upper left and right, respectively. The lower plot of Fig. 4.6 shows the interaction point position measured by the C5 detector using C.A.E.N TDC timing information as a function of time.

Figs. 4.7 and 4.8 indicate the variation of the proton and electron bunch arrival times

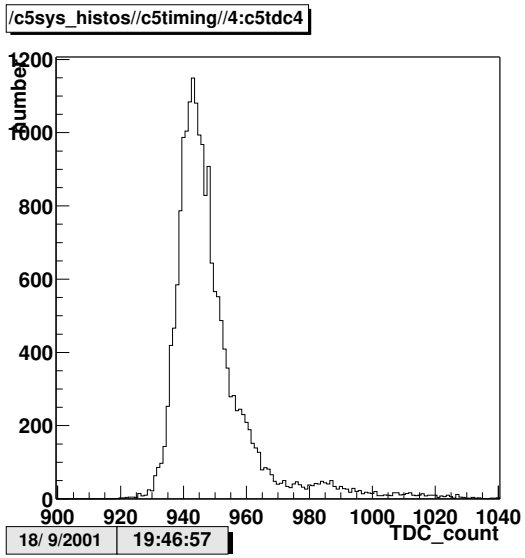

Figure 4.5: Timing spectrum measured with the CAEN TDC for measurement of C5 detector timing resolution.

averaged over all interacting bunches as a function of run number. All physics runs are shown and a total integrated luminosity 42.30 pb^{-1} in 2116 runs is represented in the plot. Fill-to-fill jumps of 1.5 ns can be seen.

Fig. 4.9 shows the distributions of average Z positions for all luminosity runs for which C5 data was available. The position of Z-vertex measured by C5 has to be within the range 0.0 ± 15.0 cm. If the Z-vertex position is outside this range beams have to be adjusted.

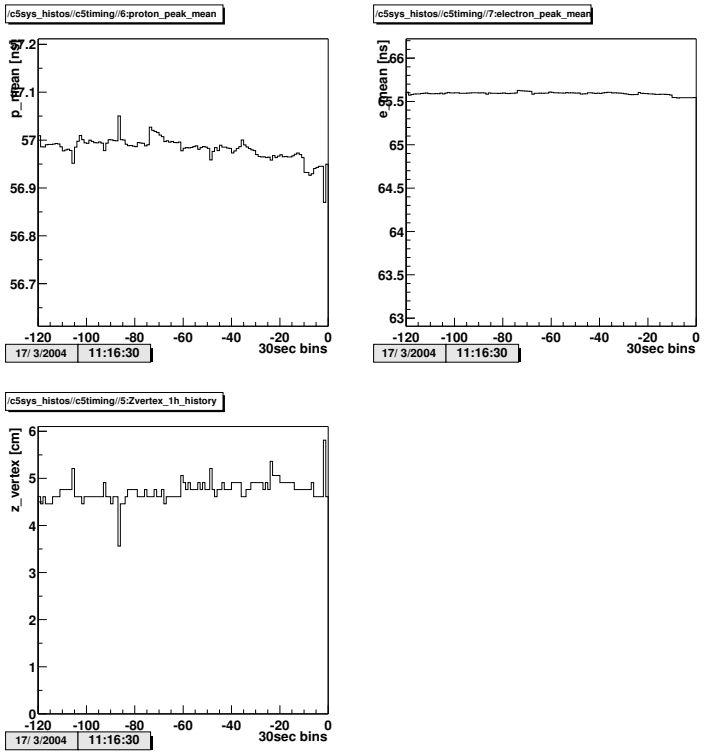

Figure 4.6: Mean value of the position of proton peak (upper left plot) and electron peak (upper right plot) in the time spectrum measured by C5 detector using C.A.E.N. TDC as a function of time. Position of interaction point (Z_{IP}) calculated from $T_{proton} - T_{electron}$ Z_{IP} as a function of time (lower plot).

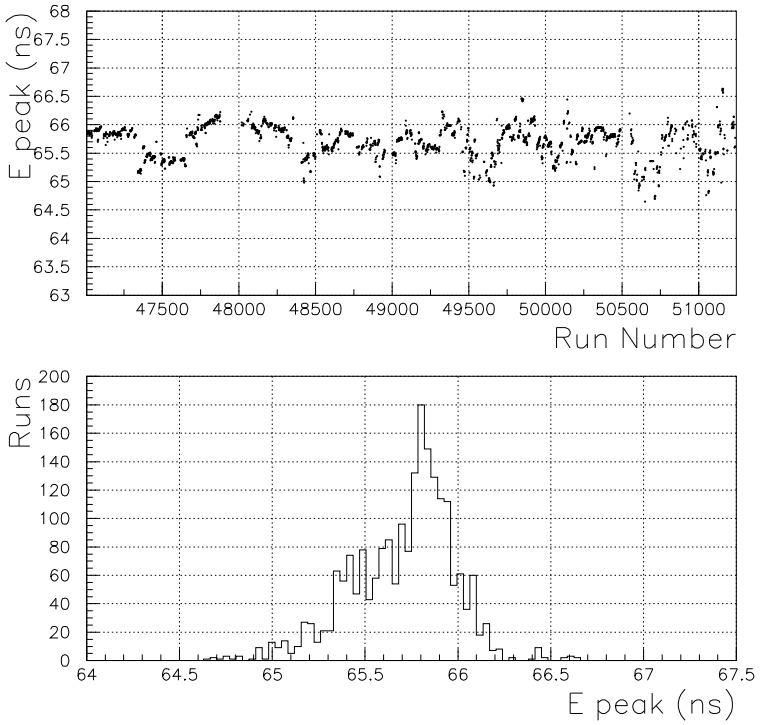

Figure 4.7: Electron bunch arrival times as measured using the C5 time distributions as a function of run number (upper plot). Electron bunch arrival times distribution for 2004 running period.

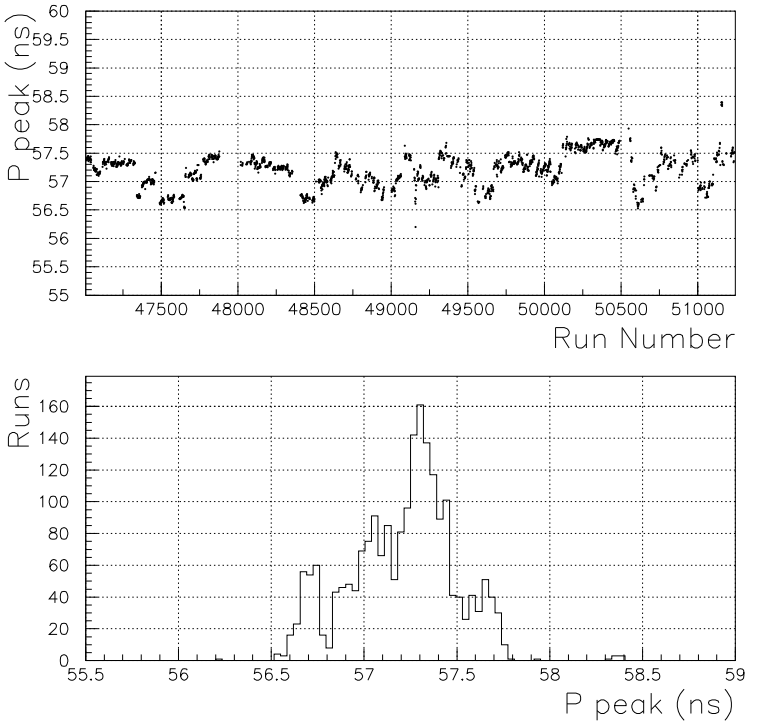

Figure 4.8: Proton bunch arrival times as measured using the C5 time distributions as a function of run number (upper plot). Proton bunch arrival times distribution for 2004 running period.

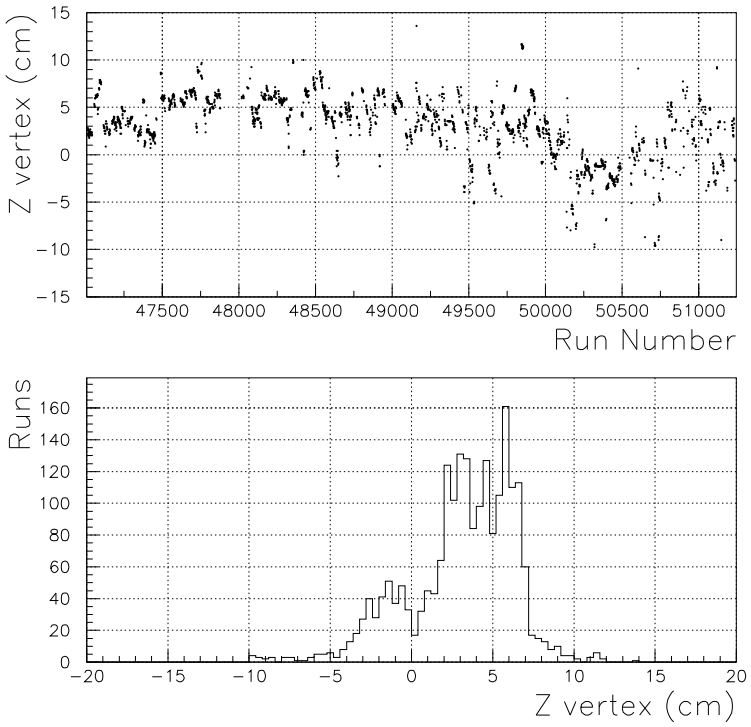

Figure 4.9: Average Z-position of the interaction vertex distributions during the 2004 running period.

4.6 Electron and proton gated rate measurements

The logic used to measure electron and proton gated rates is shown in Fig. 4.10. The measurements exploits the $\sim$ 8.3 ns, see Fig. 4.11, time difference of the electron and proton signals at the C5 detector, which is large compared to the C5 signal time resolution ($\sim$ 0.8 ns). Typical HERA electron and proton bunch lengths are $\sim$ 10 mm ($\sim$ 0.033 ns) and $\sim$ 100 mm ($\sim$ 0.33 ns), respectively, which are small w.r.t. the C5 timing resolution.

The proton gate, see Fig. 4.10, is derived by belaying the HERA clock timing signal. The electron gate is also derived from the HERA clock but with an increased delay due to the 8 ns time delay expected for the later arrival of electrons at the C5 counter. The delay used for the e gate is optimized by maximizing coincidence rate in the expected range. The 10 ns gate widths is the maximum value which does not introduce additional non type specific signal. The measured rates are used to optimize and monitor backgrounds at

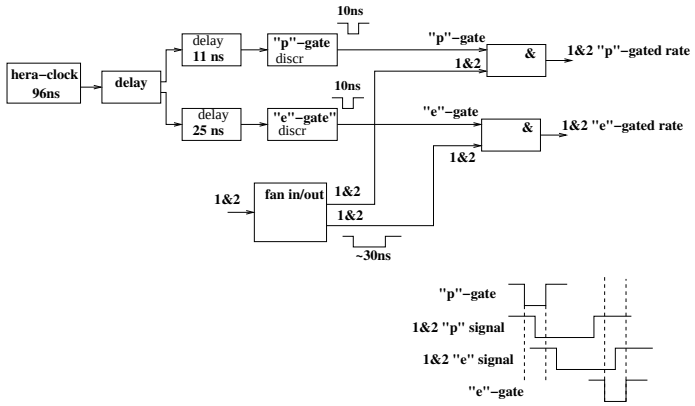

Figure 4.10: Setup for electron and proton beam gated rate measurements.

ZEUS. The C5 electron and proton gated rates are used to predict CTD currents. As the C5 detector is sensitive to charged particles and not to synchrotron radiation, whereas the CTD is sensitive to both, the C5 electron and proton gated rates can be used to predict CTD electron induced and proton induced currents, but not the synchrotron rate. In cases where the measured CTD current is higher than the C5 prediction it is assumed that the excess is due to synchrotron radiation [40], [41].

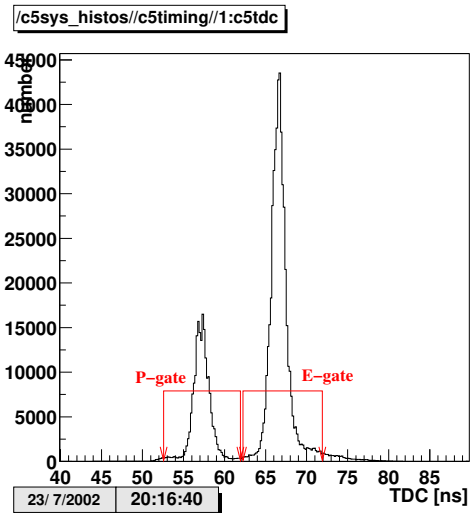

Figure 4.11: Timing spectrum with electron (right) and proton (left) beam.

4.7 LeCroy TDC measurements

As previously mentioned the LeCroy TDC allows measurements of per bunch crossing electron and proton hit occupancy in the C5 detector. This section briefly reviews initial results.

Typical LeCroy TDC histograms are shown in Fig. 4.12. In plot a) measurements corresponding to the entire HERA bunch train (bunches $0-219$) are shown, where bunch 0 has a TDC value of 2488 ns. From this plot the occupancy of each bunch in the HERA bunch train can be estimated. Plot b) shows the region around bunch 60, separate electron and proton hit occupancies are visible as are empty bunch positions in the HERA train. Plot c) shows the occupancy around a single bunch crossing, both electron and proton occupancy can be seen. Plots d) and e) shows various zooms of the region around bunch crossing Zero. Note that bunch 11 has only an electron contribution, such bunches are used for electron only background studies. In all plots the resolution of 1 bin is 1 ns.

Fig. 4.13 shows the C5 time distribution of electron and proton primary bunches and the satellite bunches measured by the LeCroy TDC and summed over all bunches. The plateau of unsynchronized background particles due to the badly tuned beams can be seen on Fig. 4.14.

4.8 C5 as VETO for GFLT

As mentioned previously C5 hit information indicates the presence of halo particles accompanying the beams.

This information is an indispensable VETO at the ZEUS GFLT allowing the removal of background events. Fig. 4.15 shows the C5 timing results at the GFLT. Vetoed events lie to the right of the blue line corresponding to the cut greater than 7 bins on the histogram. The histogram was filled during run 50531 for which the total C5 background rate was 4.23 kHz and the veto rate was 0.249 kHz.

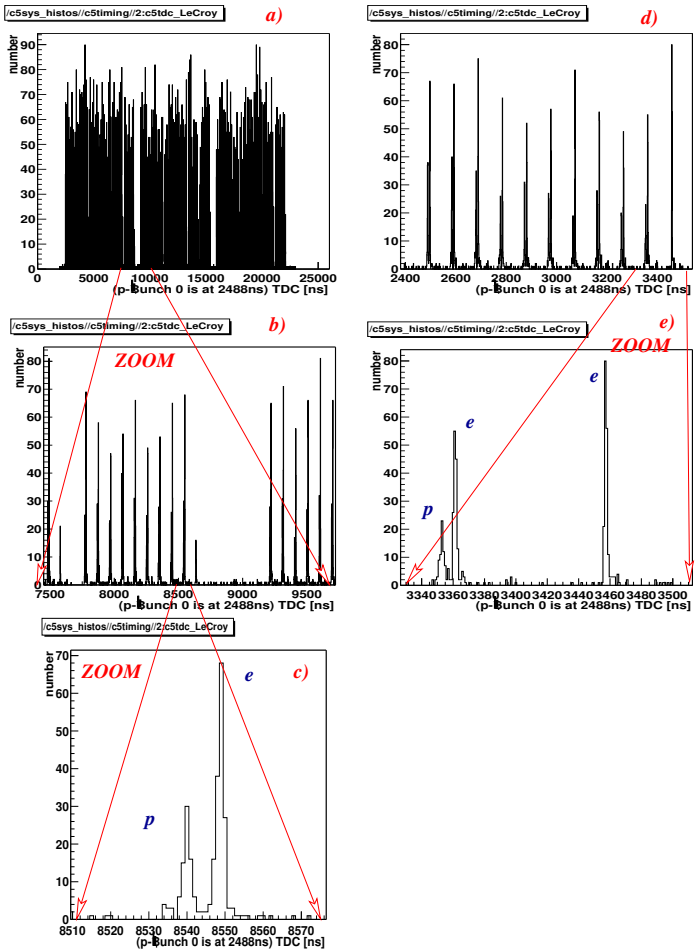

Figure 4.12: LeCroy TDC histogram. a) Full HERA bunch train. b) Zoom plot with empty bunches c) zoom plot with only one bunch filled with electrons and protons. d) Plot with first HERA bunches. e) Zoom plot with *ep* bunch and *e* only bunch. In all plots 1 bin = 1 ns.

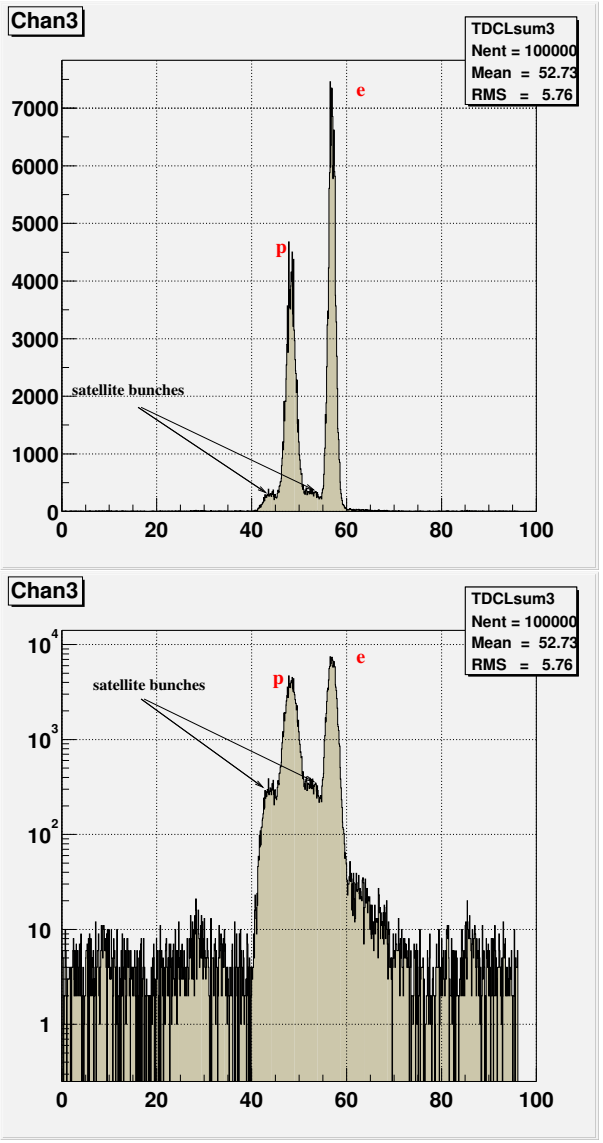

Figure 4.13: HERA bunch structure measured with the LeCroy TDC and summed over all bunches in linear (upper plot) and logarithmic (lower plot) scale. The electron and proton primary bunches and the satellite bunches can be clearly seen.

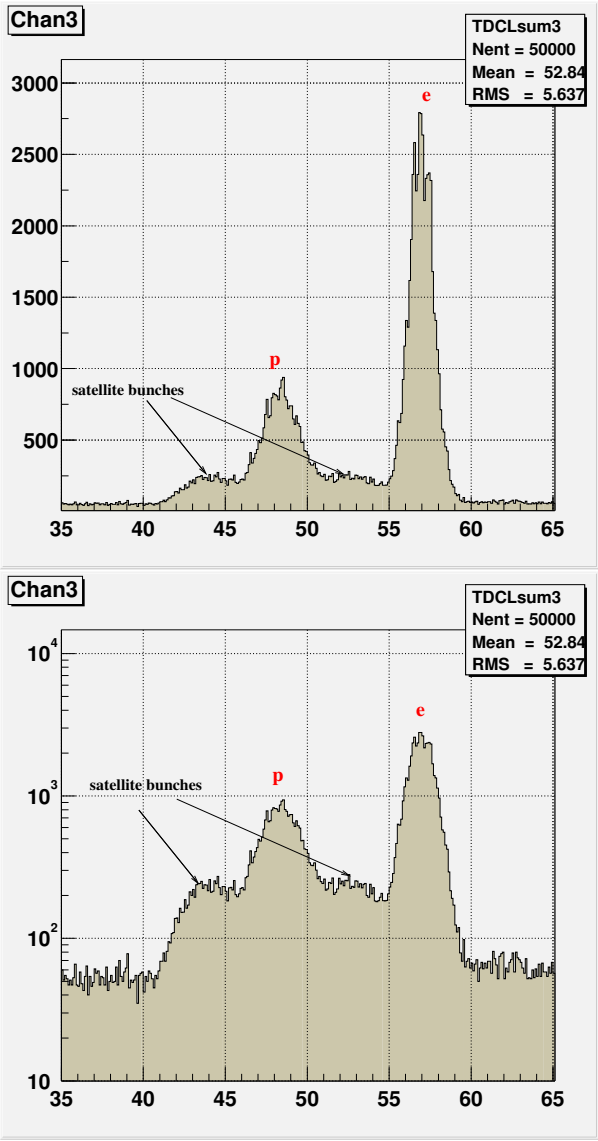

Figure 4.14: HERA bunch structure measured with the LeCroy TDC and summed over all bunches in linear (upper plot) and logarithmic (lower plot) scale. The electron and proton primary bunches and the satellite bunches as well as the plateau of unsynchronized background particles can be seen.

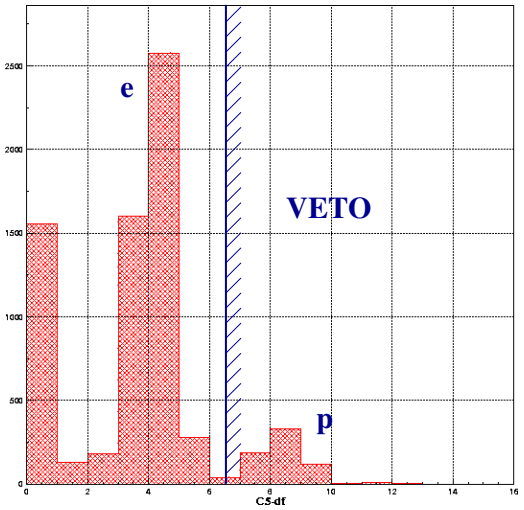

Figure 4.15: C5 timing histogram used in GFLT. All events coming from proton peak (above 7) are rejected.

4.9 Background studies

A number of measurements have been performed with the C5 detector for understanding the background conditions at HERA [40]. Fig. 4.16 shows C5 rates as a function of HERA electron beam current for different proton beam currents. In August 2002 an electron beam energy scan was performed for electron beam only in HERA and during *ep* run. Note that intermediate HERA energies are intrinsically unstable in the sense that it is difficult to tune the beam to optimum conditions. Fig. 4.17 shows the C5 rate versus the e beam energy. Shown are the data for two energy scan runs with positrons only. The first clearly exhibits a very high rate at the lower energy which falls steeply to a minimum at 21 GeV. In contrast, the second scan has a much lower rate at low beam energies, but, even so, does not exhibit a monotonic increase with the beam energy, which illustrates a systematic dependence on the beam tune. From those plots one can see that the C5 rate depends not only on the beam energy and current.

Systematic scans of both the horizontal and vertical beam tilts and positions at the ZEUS IP have been performed. The study was performed with positron beam only and beam currents of 2.5 mA (vertical scan) and 8 mA (horizontal scan). These studies show that the C5 detector is sensitive only to the particle background (not to synchrotron radiation) and that the C5 rate is independent of the beam tilt [40].

In order to look at the correlations between the C5 rate and beam-pipe vacuum (and other HERA variables) the NETMEX program [42] was integrated into the system. Using information about the HERA status the C5 rate dependence was investigated as a function of the following HERA parameters: beam energy, beam current, and beam-pipe vacuum information (see A.5). Fig. 4.18 shows electron beam current, electron beam-pipe vacuum (right and left side from the interaction point) and C5 rate as a function of time (left column) and these parameters versus rate in the C5 detector (right column). Note that HERA was filled with only e beam.

Fig. 4.19 shows proton beam energy and C5 rate as a function of time during proton beam only HERA operation. The C5 rate clearly depends on proton beam parameters, a marked increase in rate is seen during the beam ramp from 150 to 300 GeV.

Fig. 4.20 shows an example of bad background conditions measured by C5 detector using the LeCroy TDC. Large inter bunch background rates are clearly visible.

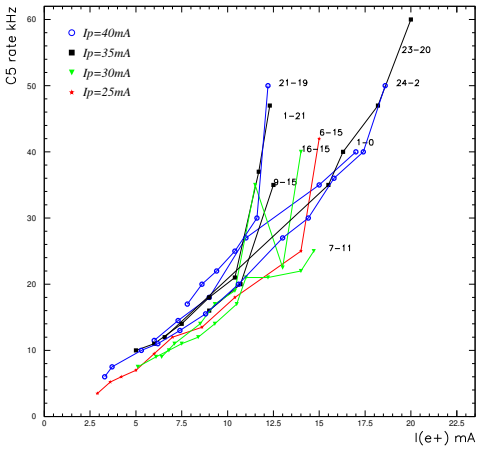

Figure 4.16: C5 rate as a function of HERA e beam current for different p beam current. Numbers near the curves shows day and hour of the begin of *ep* injection in July 2002.

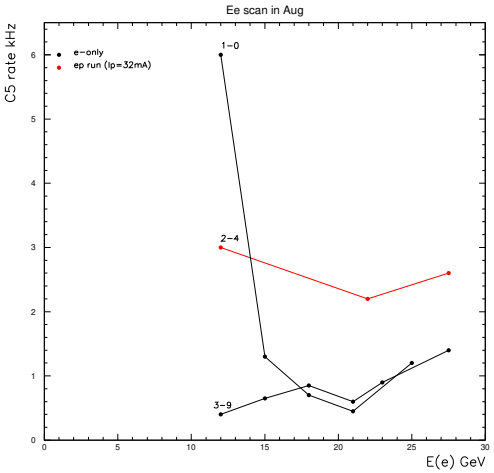

Figure 4.17: C5 rate versus e beam energy for e-only and *ep* run. Numbers near the curves shows day and hour of the begin of this test in August 2002. The positron beam current was ~ 5 mA.

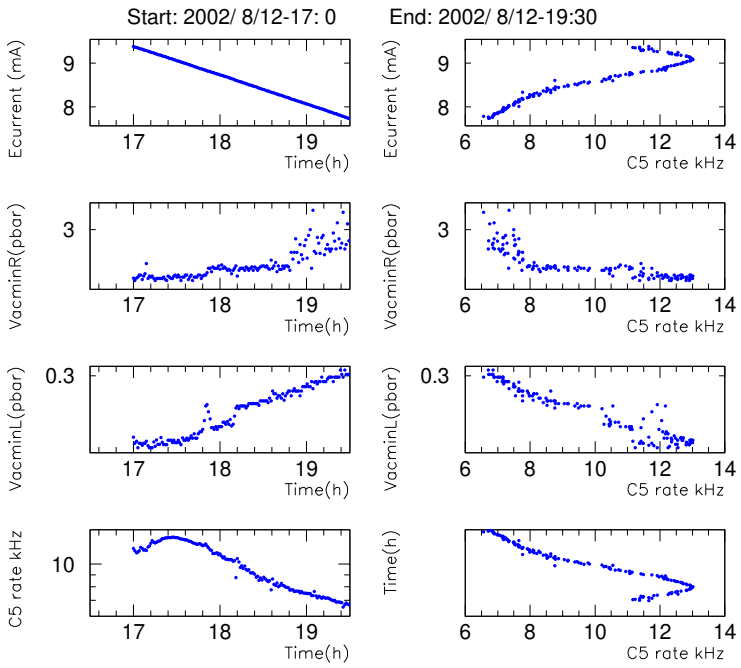

Figure 4.18: Electron beam current, electron beam-pipe vacuum (right and left side from the interaction point) and C5 rate as a function of time (left column) and versus rate in C5 detector.

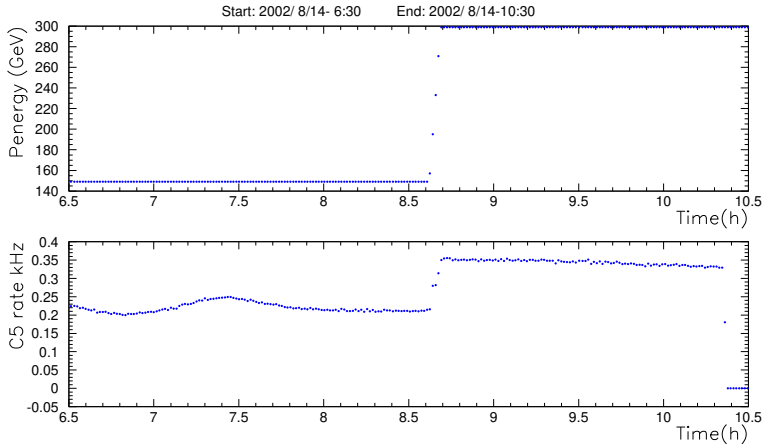

Figure 4.19: Proton beam energy (upper plot) and C5 rate (lower plot) as a function of time during proton only energy scans.

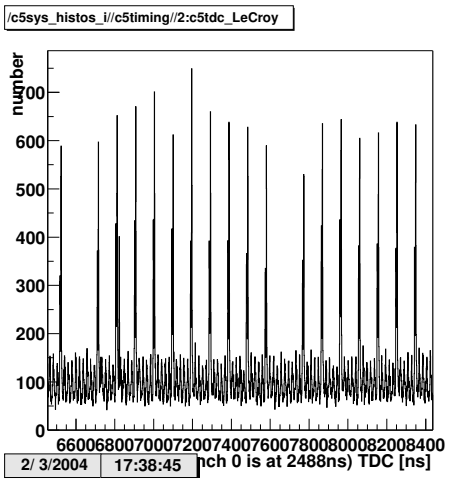

Figure 4.20: C5 time distribution measured by the LeCroy TDC for bad background condition at HERA.

Chapter 5

Monte Carlo Samples

5.1 The event simulation, reconstruction and analysis chain

Detailed information about the reconstruction and offline analysis can be found elsewhere [43]. Only a very general overview of event simulation, reconstruction and analysis is given here together with a discussion of the models and code used for simulating signal and background events relevant for this analysis.

Events generated by different physics generators are fed into a detector simulation program based on GEANT 3 [45]. This program, called MOZART ("Monte Carlo for ZEUS Analysis, Reconstruction and Trigger"), calculates the expected detector response and produces events in a format identical to that of real detector raw data. Simulated events, after passing a trigger simulation step, are then fed to the reconstruction program, ZEPHYR ("ZEUS Physics Reconstruction"). ZEPHYR produces preselected samples of events in the socalled MDST format containing calibrated detector quantities such as calorimeter energies, tracks, vertices, etc..

Starting from the MDST samples, further selection can be performed and more elaborate algorithms can be applied depending on the requirements of a specific analysis topic.

5.2 Event simulation

In order to calculate the detector efficiencies, to evaluate the sensitivity to certain physics processes and to test analysis methods both signal and background samples need to be simulated. In the following, descriptions of the models and code used for signal and background simulation are given.

5.2.1 Signal Simulation

Leptoquark production and decay were simulated with the program PYTHIA 6.17 [50]. This program simulates the s-channel diagrams in a narrow-width approximation for the resonant state. Initial and final state QCD radiation is included in a parton shower model. The coupling strength at the eq vertex is set to 0.01. The leptoquark mass was chosen in the range 100 GeV $< m_{LQ} <$ 290 GeV in 10 GeV steps. The total number of signal events generated was $\sim$ 4000 for each leptoquark mass.

5.2.2 Background Simulation

Both charged current and neutral current deep inelastic scattering processes are backgrounds to the signal being investigated. These processes were simulated using the program DJANGO 1.1 [46]. DJANGO 1.1 interfaces the programs HERACLES 4.6 [49] to both LEPTO 6.5[47] and ARIADNE [48]. This allows the different hadronization models implemented in LEPTO 6.5 and ARIADNE to be used with the same treatment of electroweak radiative corrections in HERACLES 4.6.

The electroweak parameters used in the programs were taken from the particle data group (PDG) [3] and the parton density functions in the proton were taken from the CTEQ collaboration's parametrisation CTEQ5D [51].

Charged current deep inelastic scattering is the dominant source of background. Therefore a simulated sample with very high statistics for this process is required. For reasons of efficiency, several samples with different lower bounds on x and Q^2 were generated, merged and properly normalized. Details are given in table 5.1. In total 350k simulated charged current events were used to be compared to ca. 1200 data events in the preselection.

Table 5.1: The CC DIS MC samples for e^+p and e^-p simulation.

Q^2_{gen} cut (GeV^2)	x_{gen} cut	$\sigma(e^-,p)$ (pb)	$N_{evt}(e^-,p)$ (kEvts)	$\sigma(e^+,p)$ (pb)	$N_{evt}(e^+,p)$ (kEvts)
100	-	72.8132	50	39.7454	50
100	0.1	28.2086	25	9.6438	25
100	0.3	5.6556	25	1.2712	25
100	0.5	0.8332	25	0.1258	25
100	0.7	0.0523	25	0.0046	25
400	-	60.2151	50	29.5768	50
5000	-	14.4462	50	3.1996	50
10000	-	5.3839	50	0.6827	50
20000	-	1.1339	50	0.0618	50

Poorly measured neutral current deep inelastic scattering events also contribute to the background, though at a much smaller rate. The simulated background sample therefore contains 200k events generated using DJANGO 1.1 and the MEPS option in LEPTO 6.5.

Finally, poorly measured photoproduction events may also contribute to the background. In order to evaluate this contribution 100k photoproduction events were simulated using the program HERWIG 6.1 [52] both in the socalled "direct" as well as in the "resolved" channel. These events were required to have a hadronic transverse energy $E_T^{had} > 40$ GeV. Details are given in Table 5.2.

Table 5.2: The PhP MC samples.

Process	N of gen. events	Cuts	Lumi pb^{-1}
Direct PhP	~ 100000	$E_T > 40$ GeV	352.846
Resolved PhP	~ 100000	$E_T > 40$ GeV	167.12

Chapter 6

Particle Identification and Kinematic Reconstruction

This chapter defines the kinematic quantities used in the leptoquark analysis and describes techniques available for reconstructing the kinematic properties of an event including the mass of a hypothetical leptoquark.

6.1 Reconstruction of Global Quantities

The following global event quantities, derived from calorimeter energy deposits, have been used in the event selection.

The missing transverse momentum

$$P_T = \sqrt{\left(\sum_i^{all\ cells} p_x^i\right)^2 + \left(\sum_i^{all\ cells} p_y^i\right)^2} \tag{6.1}$$

The longitudinal energy sum

$$\delta = (E - P_z) = \sum_i^{all\ cells} (E^i - P_z^i) \tag{6.2}$$

The scalar sum of the transverse energy

$$E_T = \sum_i^{all\ cells} \sqrt{(p_x^i)^2 + (p_y^i)^2}. \tag{6.3}$$

The angle of the hadronic (h) system derived from the transverse momentum and longitudinal energy sum of the hadronic energy deposits

$$\cos\gamma_h = \frac{(P_T^h)^2 - \delta_h^2}{(P_T^h)^2 + \delta_h^2} \tag{6.4}$$

where the transverse momentum and the longitudinal energy sum of the hadronic system is defined as:

$$P_T^h = \sqrt{\left(\sum_j^{all\ hadrons} p_x^{j,h}\right)^2 + \left(\sum_j^{all\ hadrons} p_y^{j,h}\right)^2} \tag{6.5}$$

$$\delta_h = (E - p_z)^h = \sum_j^{all\ hadrons} (E^{j,h} - p_z^{j,h}) \tag{6.6}$$

In the equations above the labels i and j run over calorimeter cells and hadronic energy deposits, respectively. P^h is the four-momenta $(p_x^h, p_y^h, p_z^h, E^h)$ of the hadronic final state.

6.2 Island and Jet Finding

Energy deposits in calorimeter cells are clustered into islands using the software package CORANDCUT [53], which applies calorimeter energy calibrations, dead-material correction and corrections for hadrons scattering (back-splash) into the calorimeter from non-calorimeter material.

Jets of particles are identified using the longitudinally-invariant k_T-clustering algorithm [54], in inclusive mode [55], using the four-momenta of found islands as input. The kinematics of the jets are then defined by the following equations:

$$E_T^{jet} = \sum_i E_T^i, \tag{6.7}$$

$$\eta^{jet} = \frac{\sum_i E_T^i \eta^i}{E_T^{jet}}, \tag{6.8}$$

$$\phi^{jet} = \frac{\sum_i E_T^i \phi^i}{E_T^{jet}}, \tag{6.9}$$

where E_T^{jet}, η^{jet} and ϕ^{jet} are the transverse energy, pseudorapidity and azimuthal angle of the jet, respectively. The sums run over the calorimeter cells belonging to the jet.

6.3 Reconstruction of Neutrino Parameters in Events Without Charged Leptons

As the neutrino is not detected its momentum is deduced from the hadronic system by assuming four-momentum conservation. In the limit of a massless neutrino the following equations are defined:

$$p_x^\nu = -p_x^h \tag{6.10}$$

$$p_y^\nu = -p_y^h \tag{6.11}$$

$$(p_T^\nu)^2 = (p_T^h)^2 \tag{6.12}$$

$$E_T^\nu = E_T^h \tag{6.13}$$

$$E^\nu - p_z^\nu = 2E_e^{beam} - (E^h - p_z^h) \tag{6.14}$$

$$p_z^\nu = \frac{P_{T,\nu}^2 - (E^\nu - p_z^\nu)^2}{2(E^\nu - p_z^\nu)} \tag{6.15}$$

$$E_\nu = \sqrt{(P_T^\nu)^2 + (p_z^\nu)^2} \tag{6.16}$$

6.4 Reconstruction of Kinematics

Several methods exist for determining the kinematics (x, y, Q^2) of an event from its reconstructed quantities. These are described in the following sections.

Four-Momentum

The kinematic variables of an event can be most easily derived from the four-momenta of incoming and outgoing particles using the relationships defined in Section 2.2. The resulting equations are:

$$p = E_p^{beam}(0, 0, 1, 1) \tag{6.17}$$

$$k = E_e^{beam}(0, 0, -1, 1) \tag{6.18}$$

$$k' = (k'_l \cdot \sin\theta_l \cdot \cos\phi_l, k'_l \cdot \sin\theta_l \cdot \sin\phi_l, k'_l \cdot \cos\theta_l, E'_l) \tag{6.19}$$

$$P_h = (p_h \cdot \sin\gamma_h \cos\phi_h, p_h \cdot \sin\gamma_h \sin\phi_h, p_h \cdot \cos\gamma_h, E_h), \tag{6.20}$$

where particle masses are neglected, and θ_l and θ_h (ϕ_l and ϕ_h) are the polar (azimuthal) angles of the outgoing lepton and hadronic systems, respectively.

The Jacquet-Blondel Method

It is also possible to fully determine the event kinematics from the hadronic energy flow in the event. For charged current events this method, developed by Jacquet and Blondel [57], is the only available reconstruction method. In this thesis the Jacquet and Blondel method is used to measure the kinematic variables of charged current events.

The determination of x and Q^2 is based on two assumptions:

- x and Q^2 measurement from the outgoing hadronic flow only is possible without any jet identification algorithm or proton structure hypothesis.
- For HERA kinematics, it is more suitable to express y and Q^2 in terms of laboratory variables using the energy-momentum balance between lepton and hadronic system and then to deduce x.

The expressions for the kinematic variables become:

$$y_{JB} = \frac{\delta_h}{2E_e^{beam}} \tag{6.21}$$

$$Q^2_{JB} = \frac{P_T^2}{1 - y_{JB}} \tag{6.22}$$

$$x_{JB} = \frac{Q^2_{JB}}{s \cdot y_{JB}} \tag{6.23}$$

The uncertainties of the measurement for x_{JB} and Q^2_{JB} are:

$$\frac{\Delta x_{JB}}{x_{JB}} = \sqrt{\left(\frac{1}{1-y}\right)^2 \left(\frac{\Delta E_h}{E_h}\right)^2 + \left[-\tan\frac{\gamma_h}{2} + \frac{y}{1-y}\cot\frac{\gamma_h}{2}\right]^2 (\Delta y)^2} \tag{6.24}$$

$$\frac{\Delta Q^2_{JB}}{Q^2_{JB}} = \sqrt{\left(\frac{2-y}{1-y}\right)^2 \left(\frac{\Delta E_h}{E_h}\right)^2 + \left[2\cot\gamma_h + \frac{y}{1-y}\cot\frac{\gamma_h}{2}\right]^2 (\Delta\gamma_h)^2} \tag{6.25}$$

Fig. 6.1 shows contours of constant γ_h, E_h, P_T^h, $(E-p_z)^h$ in the x, Q^2 plane. For $y_{JB} < 0.1$ contours of constant P_T^h are parallel to the x_{JB} axis which means constant P_T^h is equivalent to constant Q^2_{JB}. For $y_{JB} \approx 1$ the isolines of P_T^h merge to one line and the sensitivity to x_{JB} and Q^2_{JB} is lost.

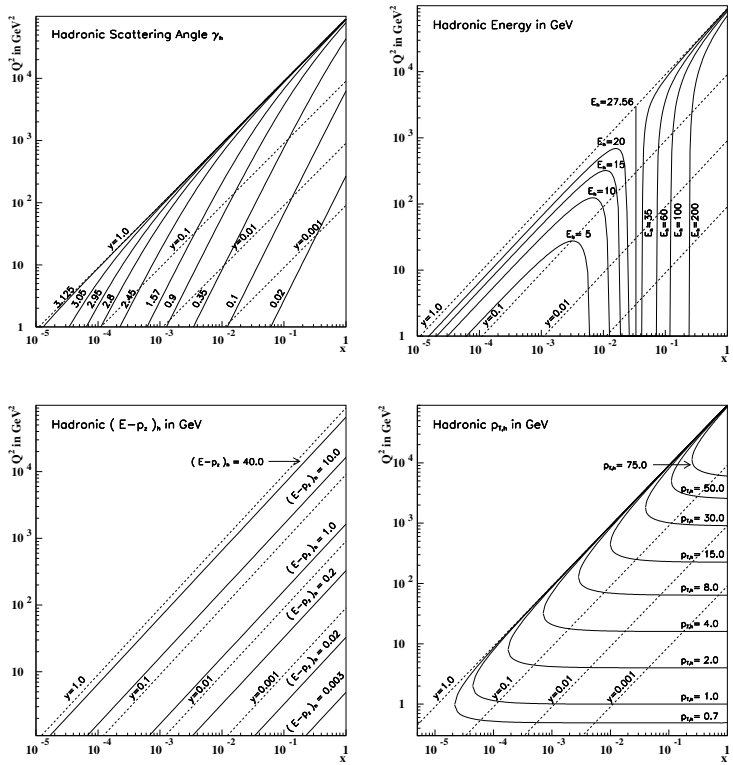

Figure 6.1: Relationships between measured hadronic kinematic variables for CC interactions. The upper left plot shows the lines of constant γ_h, the upper right plot shows the lines of constant hadronic energy E_h, the lower right plot shows lines of constant hadronic transverse momentum P_T^h, and the lower left plot shows lines of constant $E - p_z$ on the $x - Q^2$ kinematic plane.

The Electron (Lepton) Method

In the electron method [56] the kinematic variables are reconstructed from the scattered electron energy E'_l and angle θ_l, The expressions for the electron variables are:

$$Q_l^2 = -(k - k')^2 \approx 2kk' \approx 2E_e^{beam} E'_l(1 + \cos\theta_l) \tag{6.26}$$

$$x_l = \frac{E_e^{beam}}{E_p^{beam}}\left[\frac{E'_l(1 + \cos\theta_l)}{2E_e^{beam} - E'_l(1 - \cos\theta_l)}\right] \tag{6.27}$$

$$y_l = 1 - \frac{E'_l}{2E_e^{beam}}(1 - \cos\theta_l) \tag{6.28}$$

where E_e^{beam} and E_p^{beam} are the incident proton and electron energies.

From these kinematic equations the following relations for measurement uncertainties are derived:

$$\frac{\delta Q_l^2}{Q_l^2} = \frac{\delta E_l}{E_l} - \tan\frac{\theta_l}{2}\delta\theta_l \tag{6.29}$$

$$\frac{\delta x_l}{x_l} = \frac{1}{y_l}\frac{\delta E_l}{E_l} + \tan\frac{\theta_l}{2}(x_l\frac{E_p^{beam}}{E_e^{beam}} - 1)\delta\theta_l \tag{6.30}$$

$$\frac{\delta y_l}{y_l} = \frac{y_l - 1}{y_l}\frac{\delta E_l}{E_l} + \frac{y_l + 1}{y_l}\cot\frac{\theta_l}{2}\delta\theta_l \tag{6.31}$$

The Double Angle Method

In the double angle (DA) method [56], the kinematic variables are calculated from the angle of the scattered electron, θ_l, and angle of hadronic system, γ_h, with respect to the direction of the incoming proton beam. The approximation that no contribution to P_T and $E - P_Z$ is lost due to particles exiting the detector undetected along the beamline is made.

Momentum conservation requires that the sum of the energy of the incoming lepton, E_e, and quark, xE_p^{beam}, is equal to the sum of the energies of the scattered lepton E'_l and hadrons in the final state E_h,

$$xE_p^{beam} + E_e^{beam} = E'_l + E_h, \tag{6.32}$$

that the scattered lepton compensates the transverse momentum of the hadronic system,

$$E'_l \sin\theta_l = E_h \sin\gamma_h, \tag{6.33}$$

and that conservation of the longitudinal component can be written as

$$xE_p^{beam} - E_e = E'_l \cos\theta_l + E_h \cos\gamma_h. \tag{6.34}$$

Combining these expressions to eliminate xE_p^{beam} and E_h the energy of the scattered lepton as a function of the two angles θ_l and γ_h:

$$E'_l = 2E_e \frac{\sin\gamma_h}{\sin\gamma_h + \sin\theta_l - \sin(\theta_l + \gamma_h)}, \tag{6.35}$$

can be extracted.

This energy can now be substituted in the electron method formulae to obtain the kinematic variables as a function of θ_l and γ_h is:

$$Q^2_{DA} = 4E_e^2 \frac{\sin\gamma_h(1+\cos\theta_l)}{\sin\gamma_h + \sin\theta_l - \sin(\theta_l+\gamma_h)} \tag{6.36}$$

$$x^2_{DA} = \frac{E_e}{E_p} \frac{[\sin\gamma_h + \sin\theta_l + \sin(\theta_l+\gamma_h)]}{\sin\gamma_h + \sin\theta_l - \sin(\theta_l+\gamma_h)} \tag{6.37}$$

$$y^2_{DA} = \frac{\sin\theta_l(1+\cos\gamma_h)}{\sin\gamma_h + \sin\theta_l - \sin(\theta_l+\gamma_h)} \tag{6.38}$$

6.5 Leptoquark Mass Reconstruction

Leptoquarks with $M_{LQ} < 318\ GeV$ can be produced at HERA as s-channel resonances. In this channel the invariant mass distribution of the $l+q$ final state is sharply peaked at M_{LQ}. This signal is used in leptoquark searches to improve the signal-to-noise ratio by requiring the reconstructed $l+q$ mass to be consistent with the hypothesized M_{LQ}.

When reconstructing a leptoquark mass the following three approximations are made:

- The final state particles are massless.
- The contribution of the proton remnant to the reconstructed mass is negligible.
- No energy of the leptoquark escapes undetected along the beamline.

Four reconstruction methods can be used to derive the mass of the resonance:

1. $M_x : M_x = \sqrt{Q^2_{JB}/Y_{JB}}$
2. $M_{\nu had}$: The invariant mass of the reconstructed neutrino and all seen hadrons
3. $M_{\nu j}$: The invariant mass of the reconstructed neutrino and the highest-E_T jet
4. $M_{\nu js}$: The invariant mass of the reconstructed neutrino and all jets with $\eta^{jet} < 2.6$ and $P_T^{jet} > 10\ GeV$

The invariant mass in methods 2-4 are calculated from $(M^{inv}_{LQ})^2 = (P_h + P_\nu)^2$, where P_h is the four-momentum of hadrons, the highest E_T jet, or all jets, and P_ν is the four-momentum of the neutrino (see section 6.3).

For the resonance search the simplest approach is taken by only looking at states decaying to one (anti)neutrino and a single jet. When setting cross-section limits method four is used, as this shows the best resolution.

Chapter 7

Leptoquark Selection

The experimental data used in this analysis were collected by the ZEUS detector in the years $1998-2000$. The e^-p and the e^+p samples correspond to integrated luminosities of 16.7 pb^{-1} and 65.0 pb^{-1}, respectively. The event selection cuts used are similar to those used for selecting charged current DIS events which are also characterized by a missing transverse momentum signature. For the leptoquark search events have been classified into two groups using the angle of the hadronic system, γ_h, which is calculated from the nominal interaction point. Typical high- ($\gamma_h \geqslant 0.4$) and low- ($\gamma_h < 0.4$) γ_h events are shown in Fig. 7.1 and Fig. 7.2, respectively.

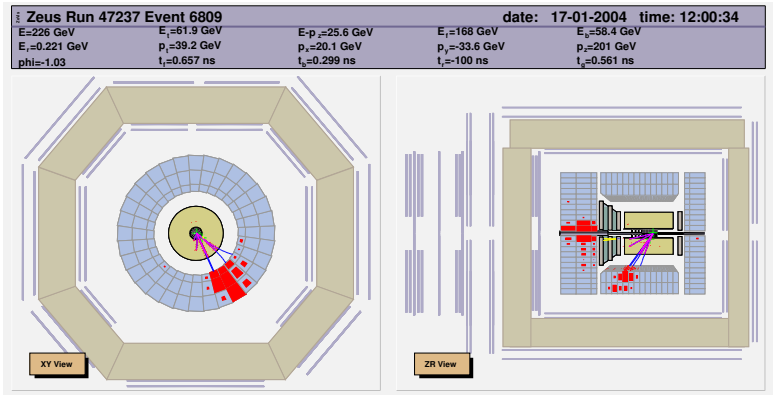

Figure 7.1: A typical high-gamma event.

The following offline selection steps, described later, are applied:

- Preselection

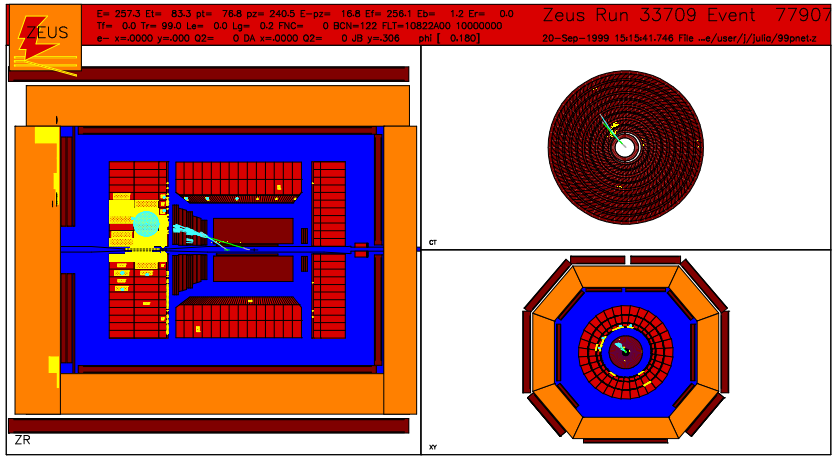

Figure 7.2: A typical low-gamma event.

- Non-ep background rejection
- Leptoquark selection cuts
  - Kinematic region: $Q^2 > 400$ GeV^2, $y < 0.9$
  - $P_T > 20$ GeV
  - Jet cuts
  - High-γ_h selection ($\gamma_h > 0.4$)
    - $|Z_{vtx}^{CTD}| < 50$ cm
    - P_T(outside first inner ring of FCAL) : $P_T[-1ir] > 14$ GeV
  - Low-γ_h selection ($\gamma_h < 0.4$)
    - $|Z_{vtx}^{FCAL}| < 50$ cm
    - P_T(outside first inner ring of FCAL) : $P_T[-1ir] > 20$ GeV
- ep background rejection
  - Photoproduction cut on P_T/E_T
  - NC DIS rejection

7.1 Preselection

Events surviving the three level online trigger system are reconstructed. At this stage a new level of filters are applied to the data and the results are written to Data Summary Tapes (DST). The DSTs are then used as a first selection, or preselection, requirement in offline analyses.

DST bit 34 is required to select events with missing $P_T > 7$ GeV. Events which satisfy all of the following 8 conditions are vetoed:

1. no vertexed track
2. $P_T[-ir] < 10$ GeV
3. $P_T < 25$ GeV
4. $P_T/E_T < 0.7$
5. $E - P_Z < 10$ GeV
6. $P_T/P_Z < 0.08$
7. $P_X < 0$
8. $|P_Y| < 4$ GeV

A detailed description of the DST bits available can be found in [61]. Note that the DST bit cuts used are less stringent than those used later, as such it is not necessary to evaluate DST bit efficiencies.

7.2 Non-*ep* backgrounds

In addition to the *ep*-background processes described in chapter 2.3 non-*ep* processes can produce high missing P_T in the calorimeter.

7.2.1 Beam-gas events

Interactions with residual gas molecules within the beam pipe can produce a large number of particles which deposit significant energy in the calorimeter. Such events have a large number of tracks and deposit most of their energy in the inner ring of the Forward Calorimeter. Additionally off momentum protons which travel at a radius different from the rest of the bunch can collide with the wall of the beam pipe and produce backgrounds similar to beam-gas events. An example of a beam-gas event is shown in Fig. 7.3.

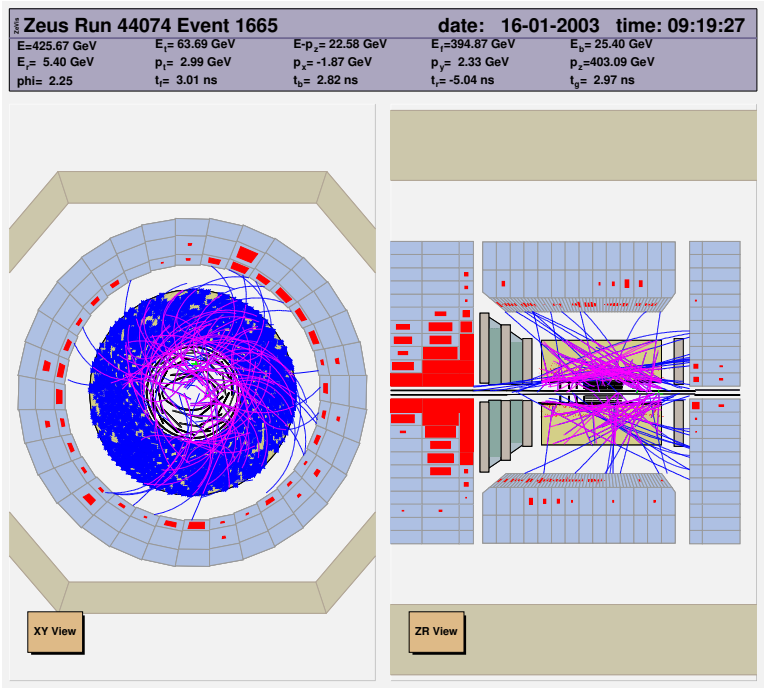

Figure 7.3: Beam-gas event.

7.2.2 Cosmic muons

An example of a cosmic-ray event that has large missing transverse momentum is shown in Fig. 7.4. These events typically have low vertex track multiplicity and calorimeter timing results inconsistent with IP interactions.

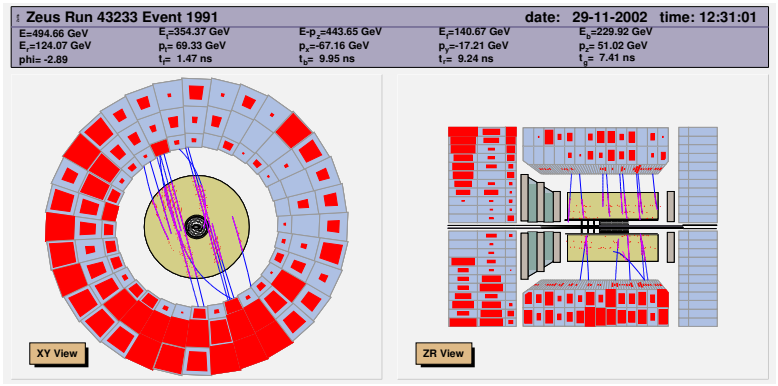

Figure 7.4: Cosmic shower.

7.2.3 Halo muons

Far upstream from the detector, protons from the beam sometimes interact with elements of the beamoptics and produce pions. These pions then decay to muons that travel parallel to the proton beam and can produce a significant measured missing P_T. Fig. 7.5 shows an example of a halo-muon event that passed the main charged current selection cuts. A large energy deposit is observed in the Forward Calorimeter, and it is accompanied by a small energy deposit in the Rear Calorimeter.

7.3 Non-*ep* background rejection

The following list of cuts are applied to reject non-*ep* background:

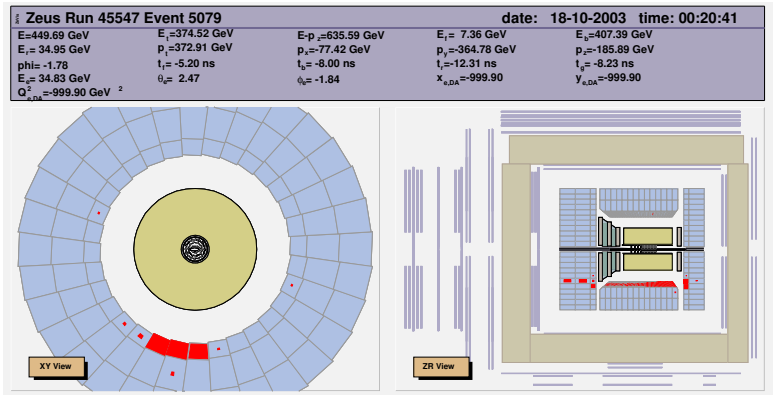

Figure 7.5: Halo muon.

7.3.1 Halo and cosmic muon rejection

Halo and cosmic muon events are rejected using the program MUFFIN [62]. This program uses data from the muon chambers, the backing calorimeter and timing information from the calorimeter in order to identify muon events.

7.3.2 HAC fractions

Particle emerging from *ep* collisions in the interaction region must hit the EMC before the HAC calorimeter layers. It follows that one would not expect such events to be purely hadronic. Non-*ep* events, in contrast, often deposit most of their energy in only one segment of the CAL. For example, a cosmic ray might deposit most of its energy in the FCAL HAC, while a halo-muon might only pass through the BCAL HAC and leave little energy in the EMC.

The following cuts reject halo muons passing through the Barrel Calorimeter HAC cells.

$$E_{Bhac1}/E_{Bcal} < 0.9 \tag{7.1}$$

$$E_{Bhac2}/E_{Bcal} < 0.6 \tag{7.2}$$

where E_{Bhac1} and E_{Bhac2} are the energies deposited in the HAC1 and HAC2 section of the BCAL, respectively. E_{Bcal} is the full energy of the Barrel part of CAL.

For events with low γ_h ($\gamma_h < 0.4$) similar additional cuts on the ratios of energies deposited in the Forward Calorimeter sections are required:

$$E_{Femc}/E_{Fcal} > 0.1 \tag{7.3}$$

$$E_{Fhac1}/E_{Fcal} > 0.1 \quad (7.4)$$

$$E_{Fhac2}/E_{Fcal} < 0.5 \quad (7.5)$$

where E_{Femc}, E_{Fhac1} and E_{Fhac2} are the energies deposited in the EMC, HAC1 and HAC2 section of the FCAL, respectively. E_{Fcal} is the full energy of the forward CAL.

7.3.3 Number of firing cells in calorimeter

A cut on the number of firing cells in the calorimeter helps to reduce non-*ep* events as some of them (for example sparks in the calorimeter) are characterized by a small number of firing cells. The cut used is:

$$N_{cell} > 50 \quad (7.6)$$

7.3.4 $P_T[-1ir]$ cuts

Beam-gas events deposit large energies close to the forward beam pipe, mostly in the inner ring of the Forward Calorimeter. To discard these, the transverse momentum, $P_T[-1ir]$, is calculated excluding inner cells of the FCAL around the beam pipe. The following cut on $P_T[-1ir]$ is applied:

$$P_T[-1ir] > \begin{cases} 20\ GeV,\ \gamma_h < 0.4 \\ 14\ GeV,\ \gamma_h > 0.4 \end{cases} \quad (7.7)$$

A higher cut is applied in the low γ_h region, since the absence of CTD vertex information leads to more background.

7.3.5 Calorimeter Timing Cuts

The calorimeter provides timing information for each cell via an internal clock, which is offset according to the geometry of the calorimeter. The offsets are chosen such that a particle traveling from the nominal interaction point will strike any cell at cell time $t = 0$. The timing is synchronized with the HERA bunch crossing time allowing calorimeter timing cuts to be used to reject non-*ep* interactions and noise. The calorimeter timing cuts used are summarized in Table 7.1.

Table 7.1: Summary of calorimeter timing cuts.

Timing cuts	Energy requirement
$\lvert T_{FCAL}\rvert < 6$ ns	$E_{FCAL} > 0.6$ GeV
$\lvert T_{BCAL}\rvert < 6$ ns	$E_{BCAL} > 0.6$ GeV
$\lvert T_{GCAL}\rvert < 6$ ns	$E_{GCAL} > 2$ GeV
$\lvert T_{FCAL} - T_{BCAL}\rvert < 6$ ns	E_{FCAL} and $E_{FCAL} > 1\ GeV$

7.3.6 Selection with CTD tracks

The number of tracks reconstructed by the CTD in the high- γ_h region must be greater then 0.

$$N_{trk} > 0 \quad (7.8)$$

A *Good Vertex Track* is a track fitted to the vertex that has transverse momentum greater 0.2 GeV and approaches within 1.5 cm the nominal beam line. Demanding a good track helps to reduce non-*ep* backgrounds.

$$N_{trk}^{Vtx} > 0 \quad (7.9)$$

$$N_{trk}^{Vtx} > (N_{trk} - 20)/4, \quad (7.10)$$

where N_{trk}^{Vtx} is the number of "good vertex tracks" found by the CTD, as defined above, and N_{trk} is the total number of tracks found by the CTD. This cut is designed to remove proton beam-gas events that are characterized by a high number of non-vertex tracks [63].

7.3.7 Visual Scan

Since there is no reliable Monte Carlo simulation of non-*ep* events, a visual scan of all selected events is made to guarantee the purity of the sample.

7.4 Leptoquark selection cuts

In this section cuts which select leptoquark (and charged current) events are described.

7.4.1 Vertex requirement

Every event is required to have either a tracking vertex (for $\gamma_h > 0.4$) or a timing vertex (for $\gamma_h < 0.4$). The Z position of the *ep* interaction vertex, measured from the timing of the Forward Calorimeter, is required to be within 50 cm of the nominal interaction point at $Z_{IP} = 0$ cm:

$$|Z_{fcal}| < 50\ cm\ (\gamma_h < 0.4) \quad (7.11)$$

The Z position of the *ep* interaction vertex, measured by the CTD, is required to be:

$$|Z_{vtx}| < 50\ cm\ (\gamma_h > 0.4) \quad (7.12)$$

These cut help reject non-*ep* interactions and insure that the events have been well reconstructed.

7.4.2 Kinematic region

The kinematic quantities (x, y and Q^2) were reconstructed using the Jacquet-Blondel method.

This analysis concentrates on the very high Q^2 region.

$$Q^2_{JB} > 400\ GeV^2 \tag{7.13}$$

From Eq. 6.22, the dependence of the Q^2 resolution on y is obtained:

$$\frac{\Delta Q^2}{Q^2} = \sqrt{4\left(\frac{\Delta P_T}{P_T}\right)^2 + \left(\frac{\Delta y}{1-y}\right)^2} \tag{7.14}$$

This becomes large as $y \to 1$, therefore, an upper cut on the measured y is applied :

$$y_{JB} < 0.9. \tag{7.15}$$

7.4.3 P_T cuts

The net transverse momentum, P_T, is the primary signature of leptoquark and charged current events. The following cut on P_T is applied:

$$P_T > 20\ GeV \tag{7.16}$$

7.4.4 Jet cuts

The following cuts were applied to the whole data sample:

At least one jet with $E_T^{jet} > 10$ GeV

To ensure accurate mass reconstruction, events which have mismeasured jets are discarded from the event sample using a "box-cut". Jet mismeasurement can occur when part of a forward-going jet is lost down the beam pipe. The box-cut requires the center of the jet with the highest E_T be outside a 30 cm ×30 cm box on the face of the FCAL.

7.5 ep background rejection

7.5.1 Pt_H/Et_H cut

Photoproduction events with high E_T are sometimes measured as having high missing P_T. To reject these, a cut of Pt_H/Et_H is applied:

$$Pt_H/Et_H > 0.4\ (Pt_H < 30\ GeV \gamma_h > 0.4) \tag{7.17}$$

The quantity Pt_H/Et_H reflects the azimuthal collimation of the energy flow. By definition $Pt_H/Et_H < 1$. This cut is also highly effective at removing beam-gas interactions.

7.5.2 Neutral current rejection for events with $\gamma_h > 0.4$

In NC scattering the transverse momentum of the hadronic system is usually balanced by the scattered electron. But if, for example, the scattered electron enters the BCAL near the edge of a module, a large mismeasurement of the electron energy can lead to an incorrectly large missing P_T.

The value of $E - P_Z$ peaks at $2E_e^{beam} = 55$ GeV for NC-DIS events. Since NC events have a relatively small P_T, large $E - P_Z$ results in a large γ_h. Most of the NC DIS background are in the high-γ_h region. Thus, a further NC-rejection cut was made utilizing an electron finder only for the high-γ_h events. In this analysis the EM [64] software package was used to find the electron candidates inside the calorimeter. Events are further examined when a candidate of electron with an energy greater than 4 GeV was found and P_T was smaller than 30 GeV. In this case the criteria for a neutral current background event is as follows:

A cone in the (η, ϕ) plane with a radius of $R \equiv \sqrt{\Delta\eta^2 + \Delta\phi^2} = 0.8$ was defined around the candidate DIS electron. Energy isolation of the electron cluster was required as

$$E_{cone} - E_e < 5\ GeV, \tag{7.18}$$

where E_{cone} is the total energy deposited in the cone, and E_e is the energy assigned to the electron cluster.

The polar angle of the electron candidate , θ_e, is required to be greater than 0.262. One of the following criteria was also required:

- if $E - P_Z$ was larger than 30 GeV and θ_e was in the range $0.262 < \theta_e < 2.88$, i.e. in the range where the CTD tracking efficiency is sufficiently high, a matching track was required to be found in the cone defined as a distance of closest approach ($DCA < 15\ cm$) between the calorimeter energy deposit and the track. More over,

the momentum of the matching track P_e is required to be consistent with the energy measured in CAL as

$$P_e/E_e > 0.25 \tag{7.19}$$

- if $E - P_Z$ was larger than 30 GeV and θ_e was greater then 2.88, then $E_T^e > 2$ GeV is required where E_T^e is the transverse energy of the electron candidate.
- The azimuthal angle difference of P_T directions measured by CAL and by CTD is denoted as $\delta\phi_{CAL-CTD}$. We required that

$$\delta\phi_{CAL-CTD} > 0.6 \tag{7.20}$$

Events which satisfy one of these criteria are labeled as neutral current background and are rejected.

7.6 Search results

When all non-ep cuts and charged current selection cuts are applied to the e^+p data 1196 events remain compared to 1122 expected from the Charged Current Monte Carlo simulation. In e^-p data, 719 events were found and 705.6 were expected from the Standard Model.

The cumulative selection efficiency for each cut from Monte Carlo and the fraction of data events passing each cut are shown in Table. 7.2. Groups 1 and 2 include either high or low gamma events, respectively. In group 3 total efficiencies for all events are summarized.

Once the events have been selected, distributions in the data are compared with the Monte Carlo prediction. In this chapter the control plots for e^+p are presented. All control plots for e^-p can be found in Appendix B.

Fig. 7.6 shows the distribution of the hadronic scattering angle (γ_h), missing transverse momentum (P_T^{mis}), $E - P_z$ and $\frac{P_T}{E_T}$. From the distribution of the hadronic scattering angle γ_h it can be seen that both normalization and shape of the data is well described by the Monte Carlo. The data and Monte Carlo agree well, within the limits of statistical fluctuations, in the P_T^{mis} distribution. The $E - P_Z$ distribution shows good agreement between data and the Charged Current Monte Carlo sample. In the $\frac{P_T}{E_T}$ distribution some discrepancies are seen for the low gamma region at $\frac{P_T}{E_T} < 0.7$. This could be due to the Monte Carlo's inability to simulate hadronization with high accuracy, but may also result from low data statistics.

Fig. 7.7 shows the vertex distribution for low gamma events measured from the timing of energy deposits in the forward calorimeter, Z_{fcal}, (upper left plot) and for high gamma events where the CTD tracking vertex, Z_{VTX}, is used (upper right plot). The data distribution for Z_{VTX} measured by the CTD shows a small shift to the +Z direction. The lower left and lower right plots show $P_T[-1ir]$ distributions for low-gamma and high-gamma events, respectively. The distributions show good agreement between data and Monte Carlo for high-gamma events. For low-gamma events small discrepancies are seen as a result of low data statistics.

The distributions of N_{trk} and N_{trk}^{Vtx} (Fig. 7.8) where only high gamma events are selected show good agreement with the data.

The distribution of N_{cells} is shown in the lower right plot of Fig. 7.8. To select events all other cut were applied except the cut on $N_{cells} > 50$. It can be seen from this plot that in the region with $N_{cells} < 50$, the number of data events is much larger than the expected number of events from the charged current Monte Carlo and also from the leptoquark MC. Most of the events in the region with $N_{cells} < 50$ are sparks in the Calorimeter or non-ep background events which are characterized by a small number of firing cells.

The plots for the fraction of energy deposited in the hadronic and electromagnetic part

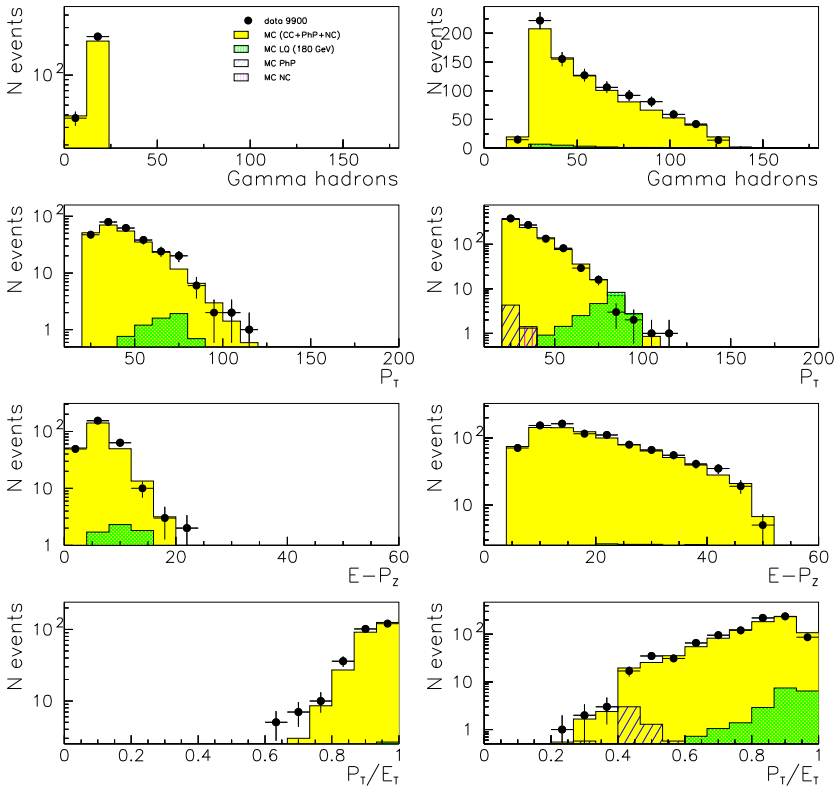

Figure 7.6: γ_h, P_T, $E - P_z$ and $\frac{P_T}{E_T}$ for low gamma events (left column) and high gamma events (right column) for e^+p data after all cuts are applied.

of the barrel calorimeter E_{Bemc}/E_{Bcal}, E_{Bhac1}/E_{Bcal} and E_{Bhac2}/E_{Bcal} after applying all selection cuts are shown in Fig. 7.9 (upper plots). It can be seen that there are too many events in the final data sample where not enough energy is deposited in the HAC1 part of the Barrel Calorimeter. These events could be non-ep events still present in the final data sample. The lower histograms of Fig. 7.9 show the E_{Femc}/E_{Fcal}, E_{Fhac1}/E_{Fcal} and E_{Fhac2}/E_{Fcal} distributions for the low gamma events after applying all selection cuts. The longitudinal energy sharing between calorimeter modules is described with an accuracy of about 10%.

Fig. 7.10 shows the Q^2, x and y distributions of the selected events in the e^+p data. The data distribution is well described by the Standard Model Monte Carlo prediction. In the e^+p data one event was found with $Q^2 \sim 50166.5$ GeV^2. This event has $\cos\theta^* \sim -0.49$ and an invariant mass of $M_{\nu j} \sim 246$ GeV. This event is shown in Fig. C.1.

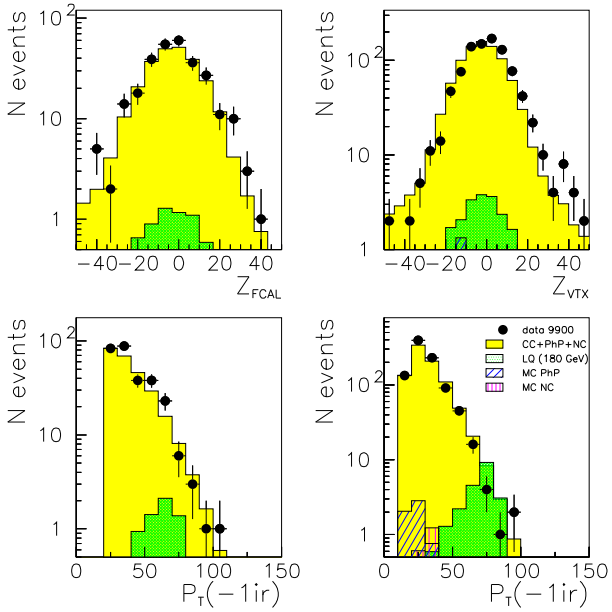

Figure 7.7: The distribution of the $z-$ position of the vertex measured using FCAL timing (upper left plot) and Z-vertex measured by CTD tracking (upper right plot) for low and high gamma events, respectively. $P_T[-1ir]$ distribution for low and high gamma events are shown in lower left and lower right plots.

Distributions of the total number of jets, E_T of the highest E_T jet and η of highest E_T jet for the selected data sample are presented in Fig. 7.11. The distributions show good agreement between data and Monte-Carlo.

Fig. 7.12 shows reconstructed neutrino variables for the e^+p selected events after all selection cuts are applied. The distributions of reconstructed neutrino E_ν show agreement between data and SM Monte Carlo. The data and Monte Carlo agree well in P_T^ν and scattered angle θ_ν.

The observed mass distribution of the ν-jet events is compared to the Monte Carlo prediction in Fig. 7.13. For all four methods of mass reconstruction (M_x, $M_{\nu had}$, $M_{\nu j}$ and $M_{\nu js}$) (see chapter 6.5) good agreement with Standard Model expectation except for the bin near 200 GeV in the $M_{\nu had}$ mass spectrum are seen. Note that the expected width for a LQ is much larger than the bin width. Some excess of data over the Standard Model

expectation histogram can be seen in the region between $150 - 200$ GeV in $M_{\nu js}$ mass spectrum.

For the νq resonance search only the highest E_T jet is used in the mass reconstruction. All missing transverse momentum is assumed to be taken by the final-state neutrino. No additional assumptions are made about how the state is produced and how it decays. This method of mass reconstruction is rather general and not confined to a specific physics model.

Fig. 7.14 and Fig. 7.15 show the observed mass distributions of ν-jet events ($M_{\nu j}$) for e^+p and e^-p data, respectively. The upper plots show the reconstructed mass spectra and the lower plots show the ratio of the observed mass spectra to the Standard Model expectation (N_{obs}/N_{exp}).

For $M_{\nu j} > 140$ GeV the e^+p data mostly lie above the expectations. One event was found with $M_{\nu j} \sim 250$ GeV. This event has $Q^2 \sim 13500$ GeV^2 and $\cos\theta^* \sim 0.567$ and is shown in Fig. C.2. For the e^-p data good agreement between data and Standard Model Monte Carlo can be seen. In the region above $M_{\nu j} > 260$ GeV one event is observed while 0.4 are expected from the Standard Model.

The reconstructed values of $M_{\nu j}$ are plotted versus $\cos\theta^*$ (Fig. 7.16) for the selected data events (upper plot), for leptoquark Monte Carlo signal (middle plot) and for charged current Monte Carlo events (lower plot). Most of the data and Charged Current Monte Carlo events are concentrated at large $\cos\theta^*$ and small mass while events from a scalar leptoquark signal have a flat distribution in $\cos\theta^*$ for defined LQ mass.

The $\cos\theta^*$ distributions for e^+p data is shown in the upper plot of Fig. 7.17. The shape of the data and CC MC for the $\cos\theta^*$ distributions are qualitatively similar, peaking at high values of $\cos\theta^*$ while a scalar LQ resonance has a flat distribution. The $\cos\theta^*$ spectrum for data and MC events with $M_{\nu j} > 180$ GeV is shown in Fig. 7.17 (lower plot). The distributions of $\cos\theta^*$ using e^-p data are shown in Fig. 7.18 for all selected events (upper plot) and for events with $M_{\nu j} > 180$ GeV (lower plot).

Unfortunately no resonant peak has been observed in e^-p and e^+p data. Therefore a limit on leptoquark production has to be set.

Table 7.2: Cumulative efficiency for MC samples and e^+p data are shown. Group 1 includes only events from the high gamma sample. Group 2 includes only low gamma events. The total efficiency is summarized in group 3.

	Only for high gamma region ($\gamma > 0.4$)						
	Cut	LQ (180)	CC	PhP dir	PhP res	NC	DATA for e^+p
1	$Q^2 > 400\ GeV^2$	96.72	66.98	17.96	18.02	8.41	39.68
	$Y < 0.9$	86.97	64.9	12.13	11.97	0.67	36.23
	$Z_{vtx}^{CTD} < 50\ cm$	84.03	62.65	11.56	11.39	0.611	35.09
	$P_T > 20\ GeV$	83.27	49.50	0.81	0.52	0.021	30.13
	$P_T(-1ir) > 10\ GeV$	83.14	49.35	0.76	0.45	0.020	29.78
	$N_{trk} > 0$	83.08	49.23	0.74	0.45	0.20	0.79
	$N_{trk}^{Good} > 0$	83.06	49.17	0.74	0.45	0.20	0.37
	$N_{trk}^{Good} > (N_{trk} - 20)/4$	82.90	49.15	0.74	0.45	0.20	0.34
	$Pt_H/Et_H > 0.4$ ($Pt_H < 30\ GeV$)	82.32	48.46	0.33	0.12	0.0093	0.33
	NC rejection	82.11	47.55	0.33	0.12	0.0089	0.32
	$N_{cell} > 50$	82.11	47.51	0.33	0.12	0.0084	0.27
	$E_{Bhac1}/E_{Bcal} < 0.9$	82.09	47.36	0.33	0.12	0.0084	0.26
	$E_{Bhac2}/E_{Bcal} < 0.6$	82.06	47.25	0.33	0.12	0.0084	0.24
	$E_T^{jet} > 10\ GeV$	81.56	46.02	0.33	0.12	0.0054	0.23
	$X_{jet} > 30\ cm$ and $Y_{jet} > 30\ cm$	81.33	45.93	0.33	0.12	0.0049	0.226
	Total eff.	81.32	45.93	0.33	0.12	0.0049	0.226

	Only for low gamma region ($\gamma < 0.4$)						
	Cut	LQ (180)	CC	PhP dir	PhP res	NC	DATA for e^+p
2	$Q^2 > 400\ GeV^2$	97.56	68.29	100	50.00	0.00	17.23
	$Y < 0.9$	97.56	68.29	100	50.00	0.00	17.22
	$\lvert Z_{fcal}\rvert < 50\ cm$	93.99	66.17	100.00	50.00	0.00	11.46
	$P_T > 20\ GeV$	93.99	65.19	100.00	50.00	0.00	10.64
	$P_T(-1ir) > 20\ GeV$	84.25	49.16	25.00	0.00	0.00	6.70
	$Pt_H/Et_H > 0.4$ ($Pt_H < 30\ GeV$)	84.07	49.09	0.00	0.00	0.00	6.70
	$E_{Femc}/E_{Fcal} > 0.1$	84.07	48.94	0.00	0.00	0.00	1.22
	$E_{Fhac1}/E_{Fcal} > 0.1$	83.64	48.51	0.00	0.00	0.00	0.640
	$E_{Fhac2}/E_{Fcal} < 0.5$	83.46	48.41	0.00	0.00	0.00	0.612
	$N_{cell} > 50$	83.46	48.36	0.00	0.00	0.00	0.205
	$E_{Bhac1}/E_{Bcal} < 0.9$	83.29	47.04	0.00	0.00	0.00	0.198
	$E_{Bhac2}/E_{Bcal} < 0.6$	83.29	46.43	0.00	0.00	0.00	0.195
	$E_T^{jet} > 10\ GeV$	82.77	45.26	0.00	0.00	0.00	0.177
	$X_{jet} > 30\ cm$ and $Y_{jet} > 30\ cm$	77.98	42.99	0.00	0.00	0.00	0.166
	Total eff.	77.98	42.99	0.00	0.00	0.00	0.166

3	Total eff. all	80.55	45.20	0.33	0.12	0.0049	0.208

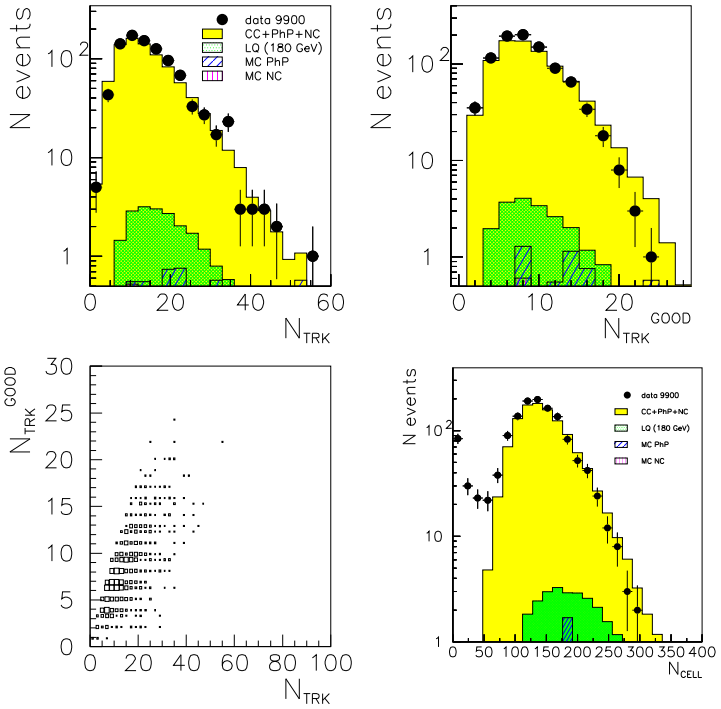

Figure 7.8: Distributions of N_{trk} (upper left), N_{Good} (upper right) and N_{trk} vs N_{Good} (lower left), where N_{trk} is the total number of CTD tracks and N_{good} is the number of "good" CTD tracks. For these plots only high gamma events are selected. The N_{cells} distribution (lower right) for e^+p data and MC after all other cuts have been applied except the cut on $N_{cells} > 50$.

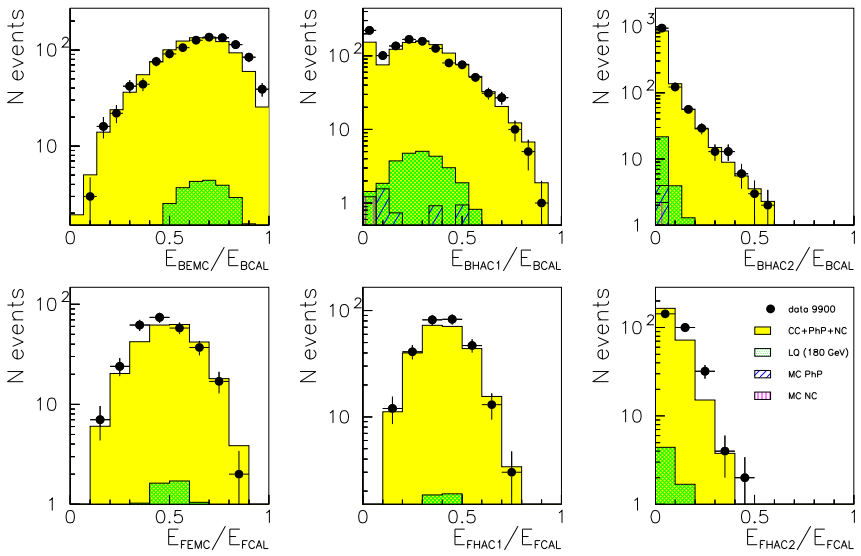

Figure 7.9: The E_{Bemc}/E_{Bcal}, E_{Bhac1}/E_{Bcal} and E_{Bhac2}/E_{Bcal} distributions for all selected events in e^+p data and Monte Carlo samples and the E_{Femc}/E_{Fcal}, E_{Fhac1}/E_{Fcal}, E_{Fhac2}/E_{Fcal} distribution for e^+p data and MC only for events selected in low gamma region.

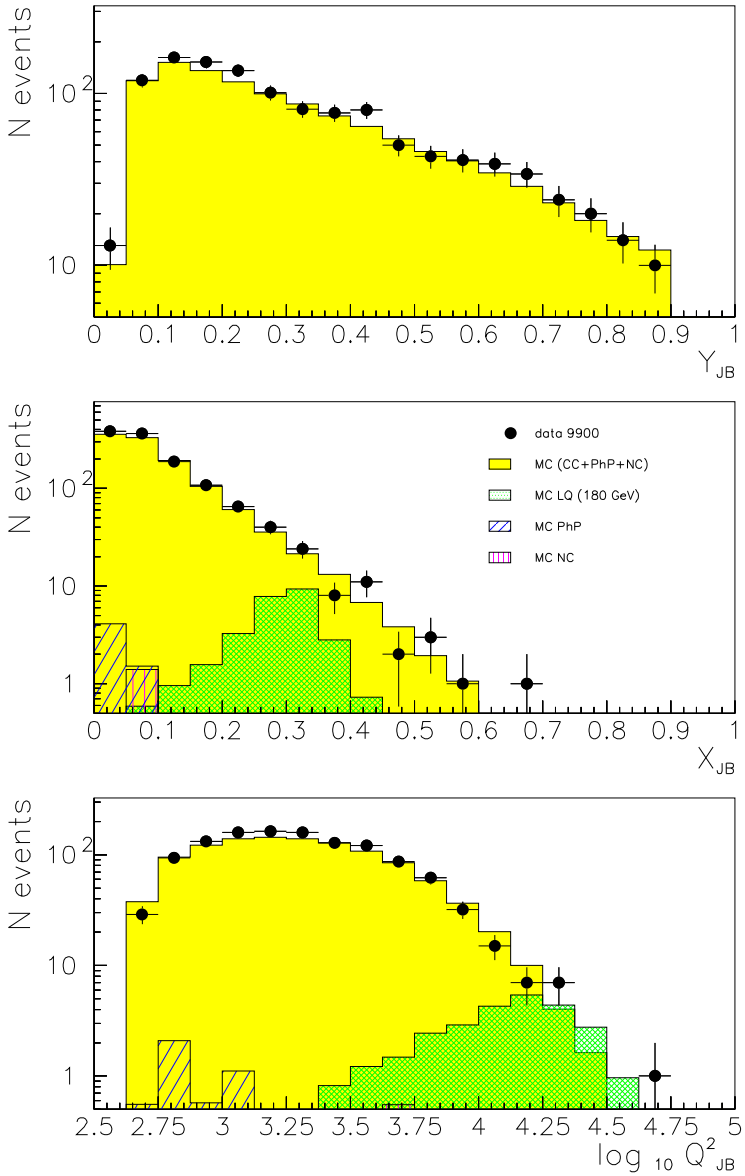

Figure 7.10: The Y_{JB}, X_{JB}, $\log_{10}(Q^2_{JB})$ distributions for e^+p data and Monte Carlo samples.

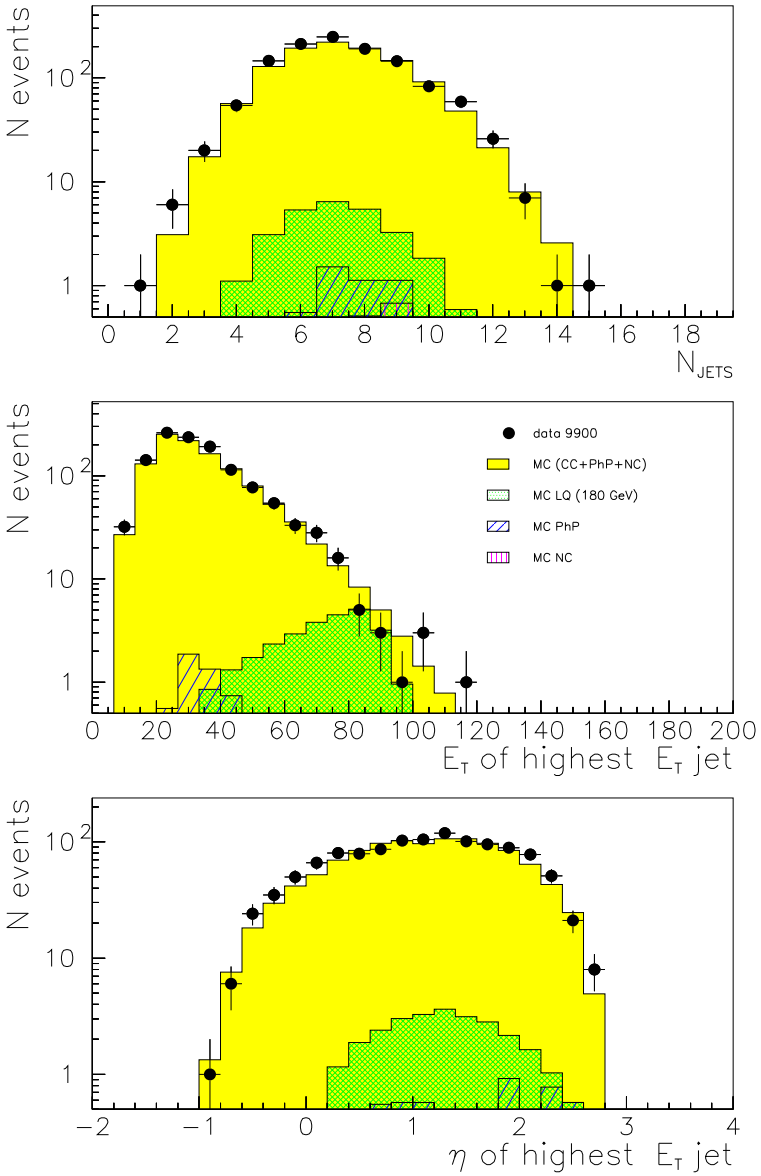

Figure 7.11: Jet variables for e^+p data after all cuts are applied.

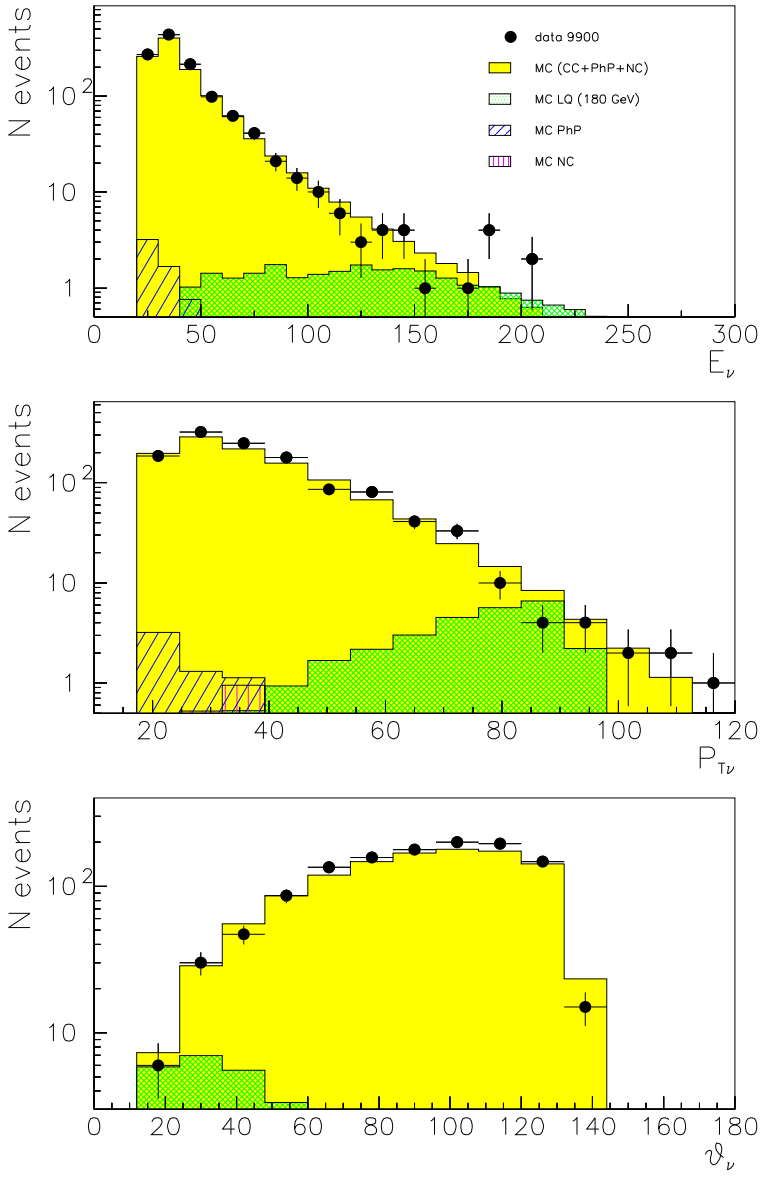

Figure 7.12: Neutrino variables (total energy E_ν, P_T^ν and θ_ν) for selected events in e^+p data after all selection cuts are applied.

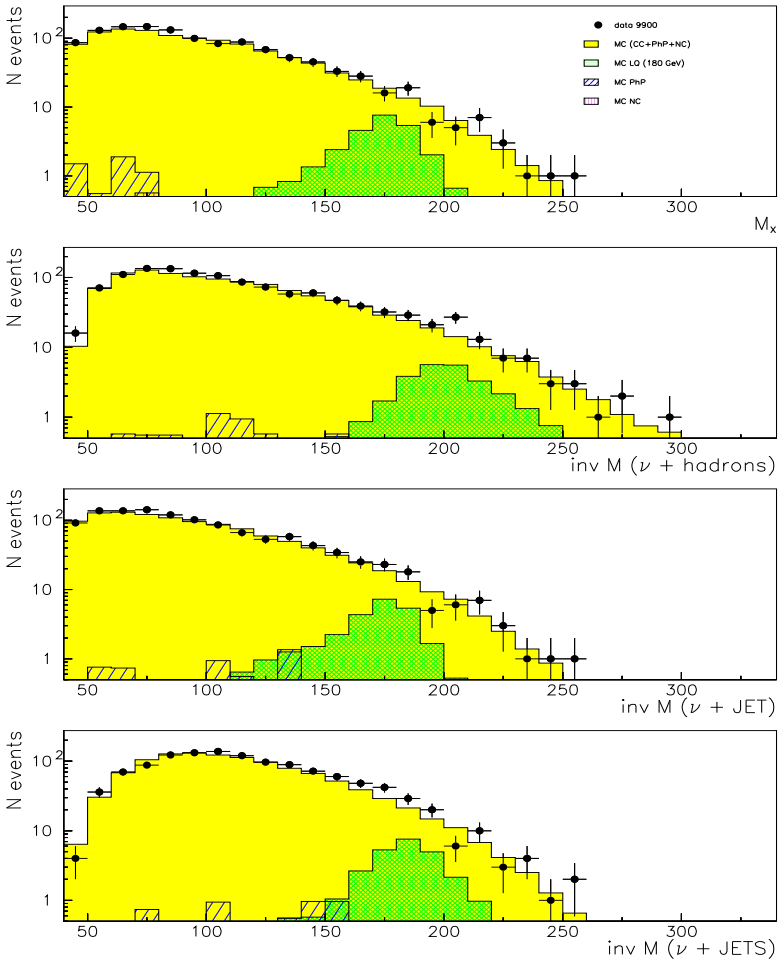

Figure 7.13: Mass spectrums for e^+p data for four different methods of mass reconstruction.

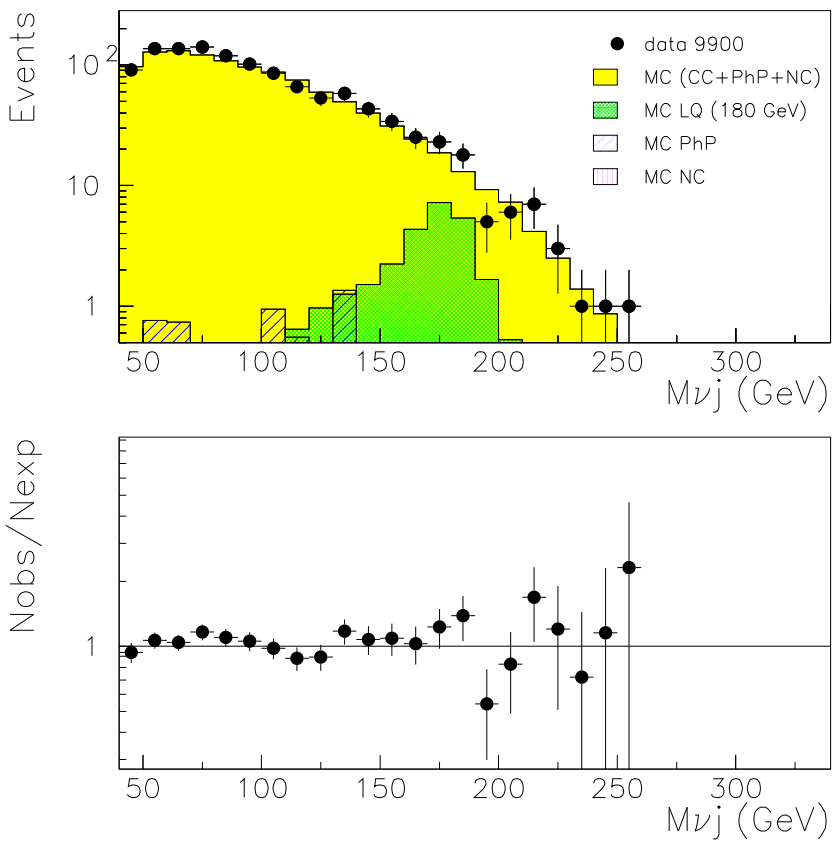

Figure 7.14: The upper plot shows a comparison of the observed e^+p samples (dots) and the CC SM expectations (yellow histogram) for the reconstructed invariant mass $M_{\nu j}$. The lower plot shows the ratio between the data and the SM expectation for e^+p data.

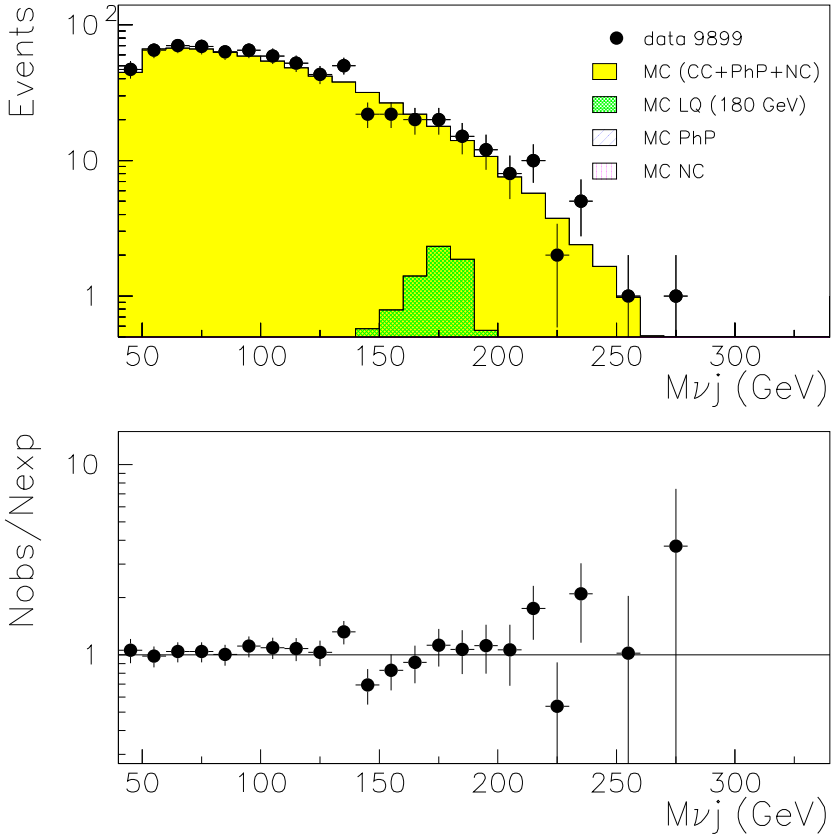

Figure 7.15: The upper plot shows a comparison of the observed e^-p samples (dots) and the CC SM expectations (yellow histogram) for the reconstructed invariant mass $M_{\nu j}$. The lower plot shows the ratio between the data and the SM expectation (N_{obs}/N_{exp}) for e^-p data.

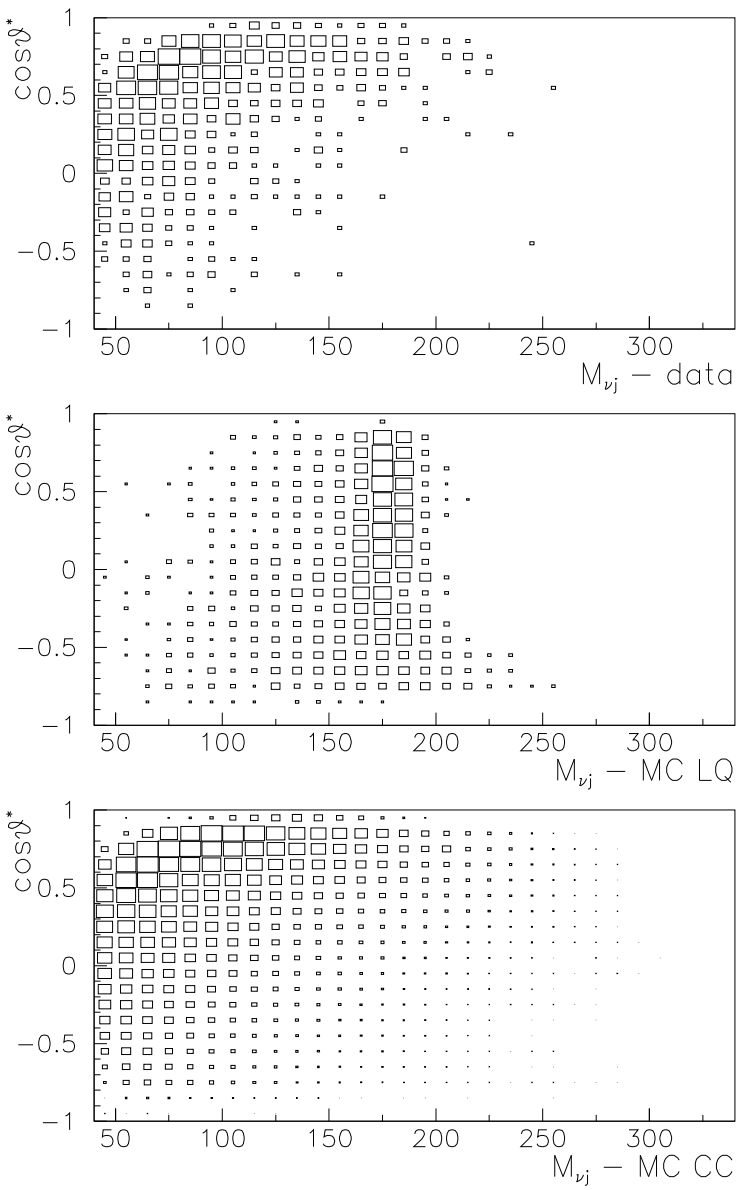

Figure 7.16: Invariant mass $M_{\nu j}$ versus $\cos\theta^*$ for e^+p data (upper plot), for leptoquark Monte Carlo (middle plot) and for Charged Current Monte Carlo (lower plot).

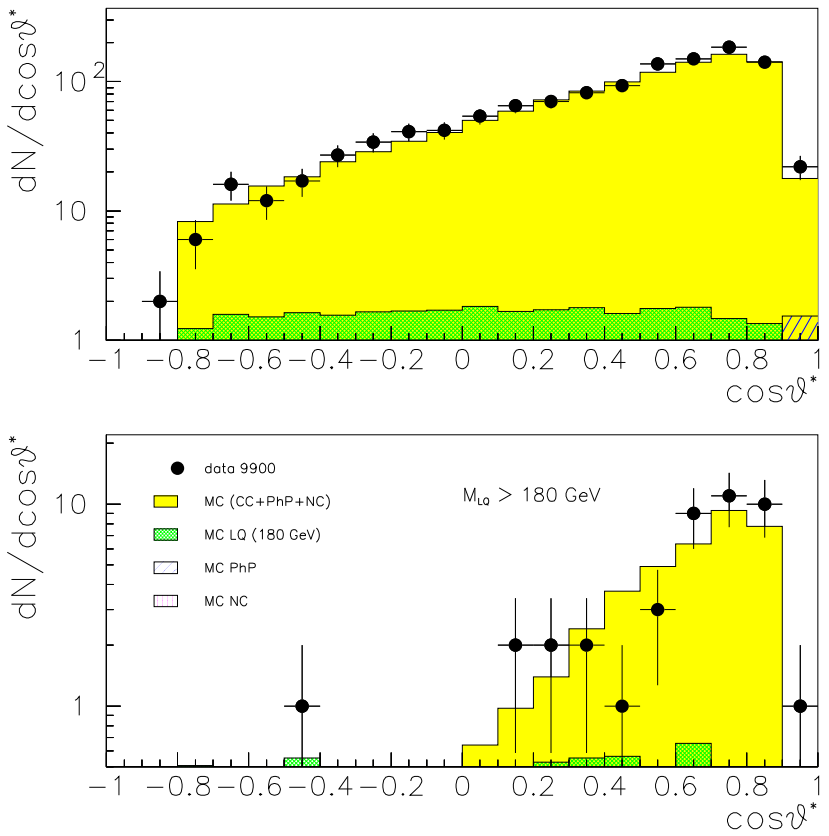

Figure 7.17: The $\cos\theta^*$ distributions for all e^+p data passing the event selection (upper plot). The $\cos\theta^*$ spectrum for data and MC events with $M_{\nu j} > 180$ GeV (lower plot).

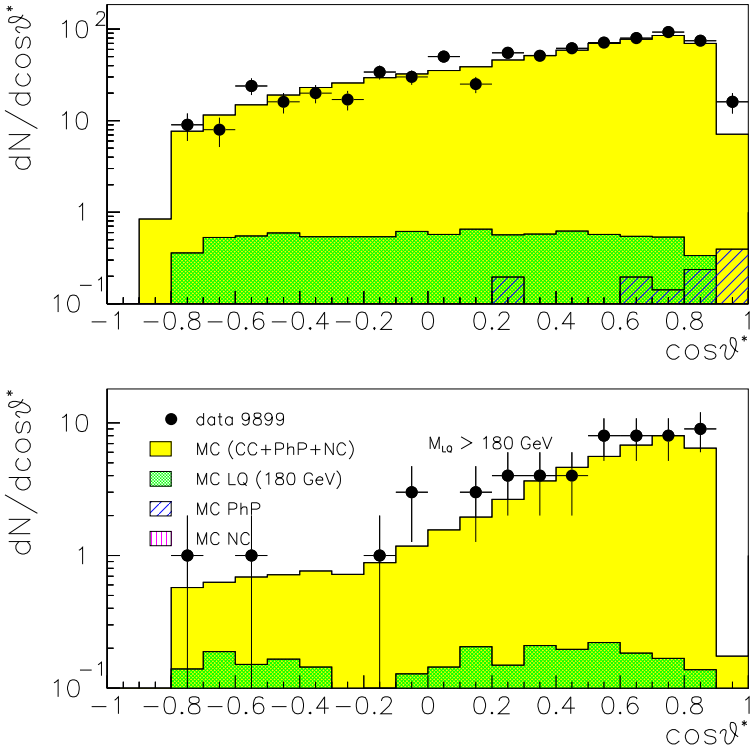

Figure 7.18: The $\cos\theta^*$ distributions for all e^-p data passing the event selection (upper plot). The $\cos\theta^*$ spectrum for data and MC events with $M_{\nu j} > 180$ GeV (lower plot).

7.7 Systematic uncertainty of the mass spectrum

To correctly estimate possible errors of the measurements, both statistical and systematic uncertainties have to be calculated. The statistical uncertainty is given by the Poisson errors on the number of entries.

Below is a list of all systematics that are taken into account:

- FCAL hadron energy scale $\pm 1\%$.
- FCAL EMC/HAC cells energy scale $\mp 1\%/\pm 1\%$.
- BCAL hadron energy scale $\pm 1\%$.
- BCAL EMC/HAC cells energy scale $\mp 1\%/\pm 1\%$.
- FCAL IR cells energy scale $\pm 10\%$.

The energy scales of the FCAL and BCAL have been determined to within $\pm 1\%$ for hadronic energy deposits [65]. This is the primary source of systematic uncertainties in the measurement of ν-jet events. Another systematic effect is the $\pm 1\%$ relative uncertainties between the EMC and HAC energy scales. The FCAL inner ring is estimated to have an uncertainty of $\pm 10\%$.

These variations have been applied to the charged current Monte Carlo followed by the selection and reconstruction of the spectrum $M_{\nu js}$. The effect of each systematic uncertainty on the $M_{\nu js}$ spectrum is shown in Fig. 7.19.

At $M_{\nu js}$ above 250 GeV the total systematic uncertainty is greater than 20%. The large uncertainty at high mass is primarily due to the energy-scale uncertainty in the FCAL and the FCAL inner ring since events with high mass deposit most of their energy at small angles in the FCAL.

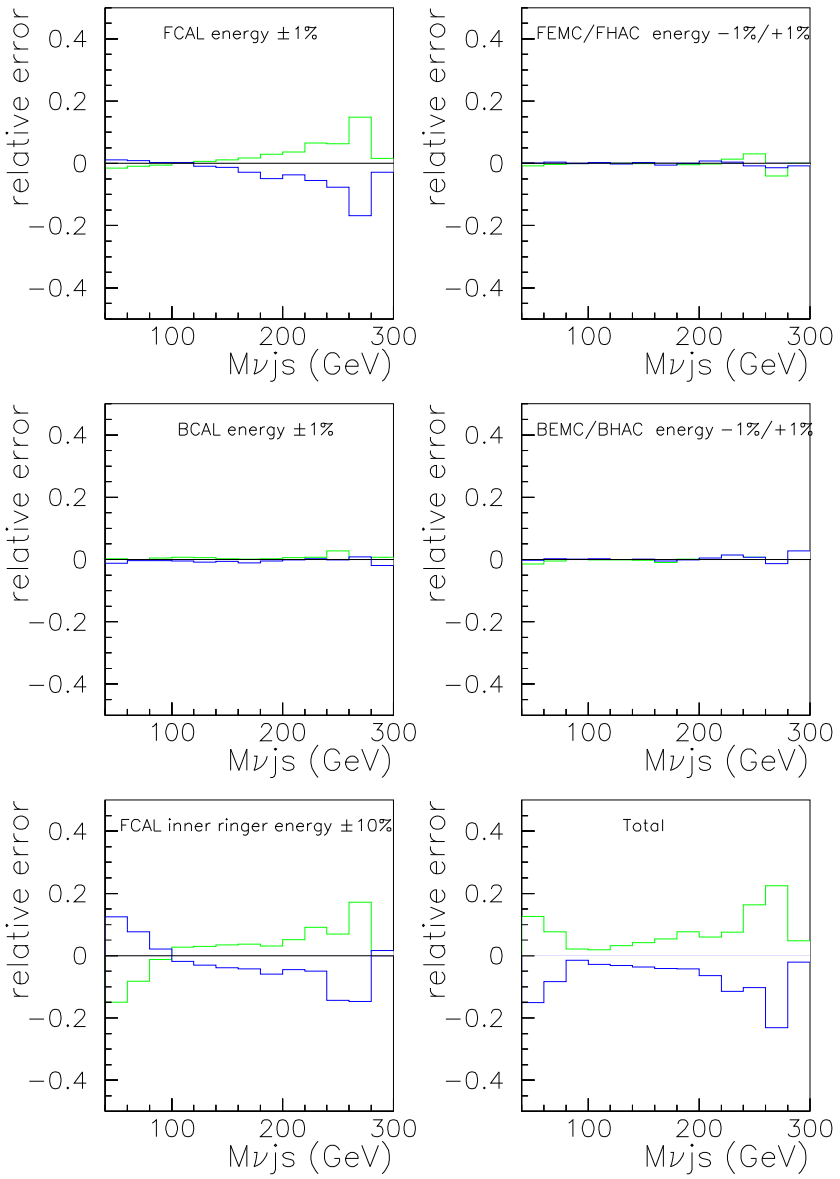

Figure 7.19: The fractional uncertainty, $(N - N_{nom})/N_{nom}$, from each systematic effect in the measurement of $M_{\nu jets}$ spectrum.

Chapter 8

Leptoquark Coupling Limit

The absence of a significant resonant peak in the analysis presented means that only limits can be set on the leptoquark production cross-section and coupling constants. This chapter describes how these limits are determined within the framework of the Narrow Width Approximation Method (NWAM) and two likelihood based methods.

8.1 Narrow width approximation method

NWAM is used to estimate the total cross-section of a resonant state by integrating over the s-channel cross-section. Direct and interference contributions from u-channel production are ignored and it is assumed that the width of the resonance is sufficiently narrow and the coupling small ($\lambda < 1.0$) so that parton densities can be evaluated at $x = M_{LQ}^2/s$ in order to calculate the resonant cross-section (see Eq. 2.23). In this analysis the leptoquark is assumed to have properties described by the leptoquark Monte Carlo simulation reviewed in section 5.2.1.

To set limits on the leptoquark production cross-section and coupling constants, it is necessary to minimize the expected cross-section limit under the assumption that no signal is observed. This minimization is achieved by varying the search mass window size and $\cos\theta^*$ cut. When convergence is achieved the leptoquark cross-section limit is calculated after applying the optimized cuts to the data.

8.1.1 Determination of the search window size

Monte Carlo samples with different true leptoquark masses have been generated to evaluate the optimal search mass window size.

The result of applying the mass reconstruction methods (M_x, $M_{\nu had}$, $M_{\nu j}$, and $M_{\nu js}$)

described in section 6.5 to these samples are shown in Fig. 8.1.

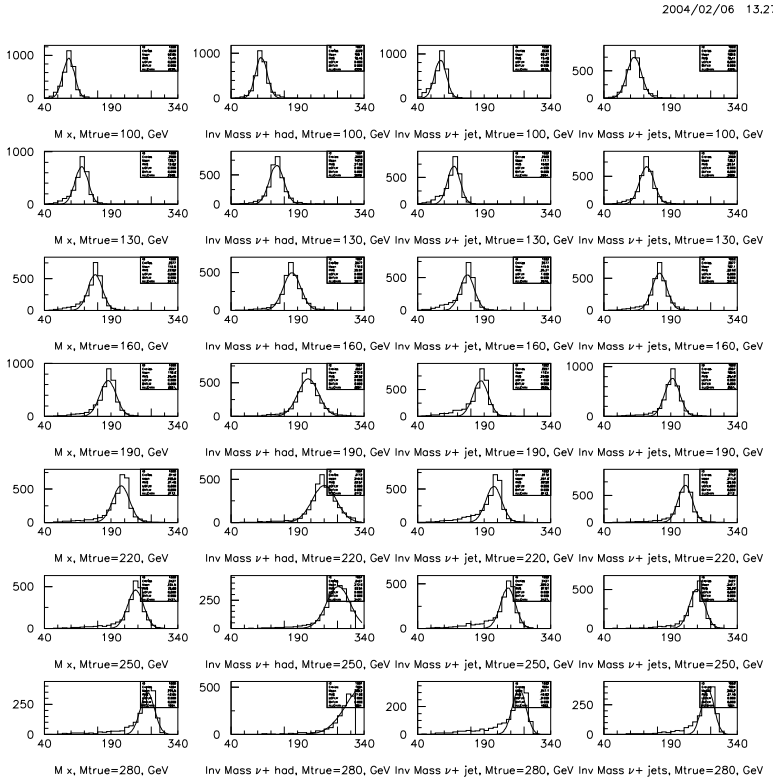

Figure 8.1: Reconstructed mass spectrum for different M_{true} numbers using four different reconstruction methods M_x (left column), $M_{\nu had}$ (middle left column), $M_{\nu j}$ (middle right column), and $M_{\nu js}$ (right column).

The superimposed curves are the results of Gaussian fits to the spectra. The fit parameters (mass, μ, and width, σ) are used in Fig. 8.2 to show the relative error in the estimation of the true mass of the leptoquark and the width introduced as a function of true mass. As discussed in section 2.5.1 the expected width of a LQ with mass $\sim 200\ GeV$ is $\Gamma/M_{LQ} = 4/200 = 0.02$, which is much less than the detector resolution of ≥ 0.04 GeV over the mass range $100 \leq M_{LQ} \leq 300$ GeV, c.f. Fig. 8.2.

For all true leptoquark masses the $M_{\nu j}$, $M_{\nu js}$ and M_x methods give similar small mass bias and width. The distributions of the fit parameters obtained from the $M_{\nu js}$ reconstruction method versus true leptoquark mass are shown in Fig. 8.3. The size of the window is chosen to be $\pm 1.5\sigma$ around μ [67], which corresponds to a window size of $\sim 50\ GeV$ at

$M_{\nu js} = 200 GeV$. In principal the window size could be optimized, however a previous study [66] has shown that the window size has little effect on the final results.

8.1.2 Optimization of $\cos(\theta^*)$ cut

The $\cos\theta^*$ cut is optimized using charged current DIS Monte Carlo and leptoquark Monte Carlo samples. For a given LQ mass, after the $M_{\nu js}$ searching window size is defined, a certain $\cos\theta^*$ cut is applied to the charged current DIS MC and leptoquark MC events. Using charged current DIS Monte Carlo the number of Standard Model events expected, N_{exp}, in the range $\cos\theta^* < \cos\theta^*_{cut}$ and $M_{\nu js}$ within $\mu \pm 1.5\sigma$ is calculated.

The expected cross section limit $< \sigma_{lim} >$ is calculated as a function of $\cos\theta^*$ cut.

$$< \sigma_{lim} >= \sum_{N_{obs}=0}^{\infty} [P_P(N_{obs}, N_{exp}) \cdot \sigma_{lim}(N_{obs}, N_{exp}, \epsilon, L) \cdot \beta] \tag{8.1}$$

Here

$$\sigma_{lim} = N_{sig}/(L \cdot \epsilon) \tag{8.2}$$

is the 95% Confidence Level (CL) cross-section limit on the leptoquark signal, with N_{exp} and N_{obs}. L is the luminosity and ϵ is the LQ efficiency after all selection cuts, including mass window cut and extra $\cos\theta^*$ cut calculated using the leptoquark Monte Carlo. N_{sig}, the 95% CL upper limit on number of new physics events, is obtained by solving the following equation:

$$\sum_{k=0}^{N_{obs}} P_P(k, N_{exp} + N_{sig}) = 0.05 \sum_{k=0}^{N_{obs}} P_P(k, N_{exp}) \tag{8.3}$$

where the $P_P(k, N)$ is the Poisson probability to find k events when N events are expected:

$$P_P(k, N) = \frac{N^k e^{-N}}{k!} \tag{8.4}$$

Distributions of $< \sigma_{lim} >$ as a function of the $\cos\theta^*$ cut for different LQ Monte Carlo samples are shown in Fig. 8.4 . The $\cos\theta^*$ cut with minimum $< \sigma_{lim} >$ is the final optimized cut.

The obtained $\cos\theta^*_{max}$ values are shown in Fig. 8.5 for the e^+p (upper left) and e^-p samples (upper right). Polynomial fits to these distribution are used as cuts for data and Monte Carlo samples as a function of $M_{\nu js}$. Events are rejected if $\cos\theta^*$ is larger than the corresponding value in the plot. From these plots it can be seen that for the mass range from $100 - 300\ GeV$ the $\cos\theta^*$ cut has a plateau distribution near 1 as a function of LQ mass for vector type leptoquarks. In contrast the $\cos\theta^*$ cut for the scalar type increases from 0.3 till 1 in the e^+p sample and stays within $0.4 - 0.8$ for the e^-p sample. Both of these curves have a minimum around a LQ mass $\sim 200\ GeV$. The tighter $\cos\theta^*$ cut for scalar LQ originates from the y distribution (or decay angle). The scalar LQ has a isotropic distribution of the decay angle (flay y distribution) while the vector LQ has $(1-y)^2$ distribution and it is closer to the Standard Model distribution which has a $1/y^2$ dependence. Therefore, the tighter $\cos\theta^*$ cut gives a better signal to background ratio for scalar LQ.

After applying mass window and $\cos\theta^*$ cuts 251 events are observed while 248 events are expected from the Standard Model. Fig. 8.6 shows the distributions of P_T^{mis}, $M_{\nu j}$, and $\cos\theta^*$ after applying the mass window and $\cos\theta^*$ cuts to the e^+p data. The distributions agree well with the Standard Model expectation. In the tail of the invariant mass plot for $M_{\nu j}$ above 180 GeV 6 events are observed while ~ 3.2 are expected. The distribution of $\cos\theta^*$ for $M_{\nu j} > 180\ GeV$ is also shown in the lower plot of Fig. 8.6.

The final leptoquark efficiencies after applying mass window and $\cos\theta^*$ cut are plotted as a function of the leptoquark masses in Fig. 8.5 for the e^+p and e^-p samples.

8.1.3 $\sigma \cdot \beta$ and λ limit at 95% CL

The leptoquark reconstruction efficiency after mass window and $\cos(\theta^*)_{max}$ cuts are applied are shown in Fig. 8.5. Polynomial fits of these distributions are then used as efficiencies in Eq.8.2.

Limits on the cross-sections of scalar and vector resonance states are obtained using Eq. 8.1 - 8.2 for M_{LQ} between 90 and 300 GeV in 1 GeV steps. The results are shown in Fig. 8.7. The area above the curve is excluded by this analysis. For both scalar and vector states, tighter limits are obtained from the e^+p data because of the larger luminosity and the smaller cross-section of the DIS background when compared to the e^-p dataset.

The limits on $\sigma \cdot \beta$ are converted to limits on the leptoquark coupling λ using Eq. 2.23. The branching ratio for the νq decay channel is set to $\beta_{\nu q} = 1/2$. The coupling limits for S_0^L and V_0^L LQ states, which are listed in Tab. 2.4, are shown in Fig. 8.7. The area above the curve is excluded by this analysis. For the S_0^L LQ states the e^-p sample gives better limits because the leptoquark state can couple to a valence u-quark, while in the e^+p collision the LQ couples to a sea $\bar{u}$-quark. In contrast, for the vector LQ states V_0^L, the better limit is obtained with the e^+p sample, where the LQ couples to the d-quark, while in e^-p collision the LQ couples to a sea $\bar{d}$-quark.

If the electroweak coupling $\lambda = 0.31 \sim \sqrt{4\pi\alpha_{EM}}$ is assumed then values of $M_{LQ} < 285\ GeV$ are excluded for both S_0^L and V_0^L states. Values of $M_{LQ} < 270\ GeV$ are excluded for the coupling $\lambda = 0.1$ for both S_0^L and V_0^L states. The limits from Tevatron [68] and LEP experiments are also shown in Fig. 8.7. For M_{LQ} masses between 204 GeV and 290 GeV this analysis provides the tightest constraint for scalar LQ.

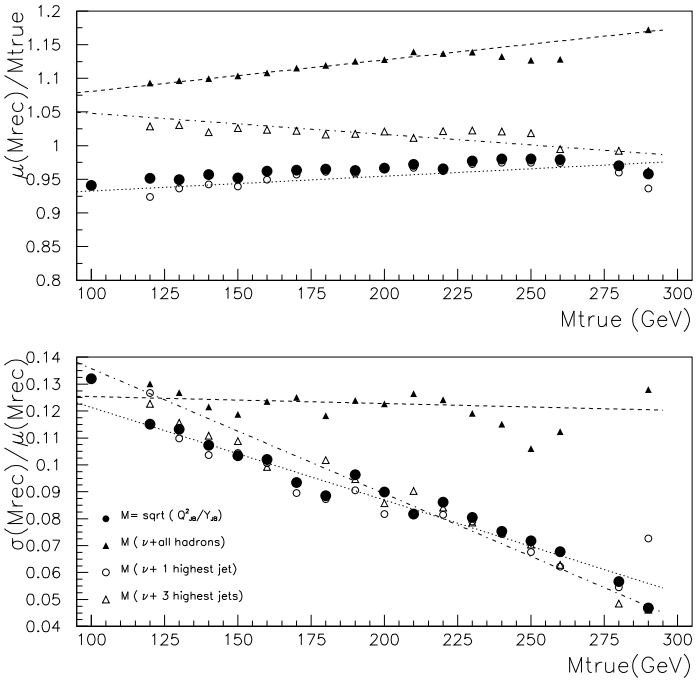

Figure 8.2: Distribution of fitting parameters (μ and σ/μ) of reconstructed mass spectra using four methods (M_x, $M_{\nu had}$, $M_{\nu j}$, and $M_{\nu js}$) of mass reconstruction as a function of true leptoquark mass.

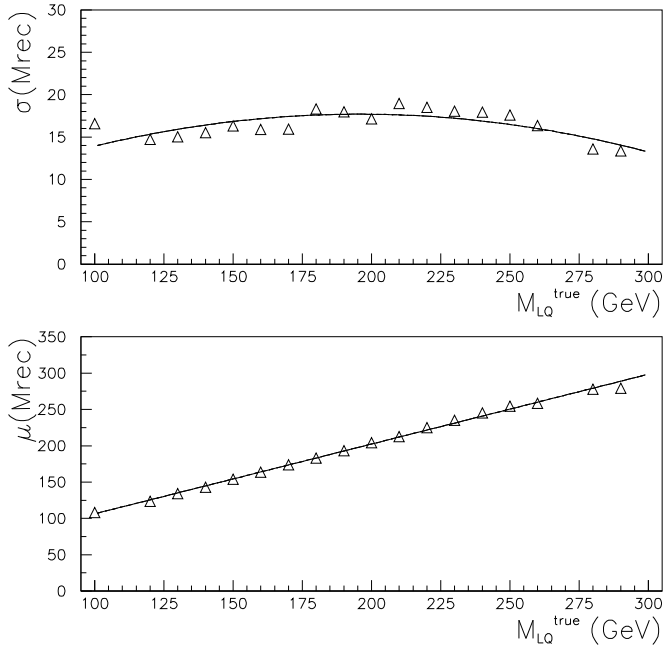

Figure 8.3: Distribution of fitting parameters (μ and σ) of reconstructed mass spectra using $M_{\nu js}$ method vs the true leptoquark mass.

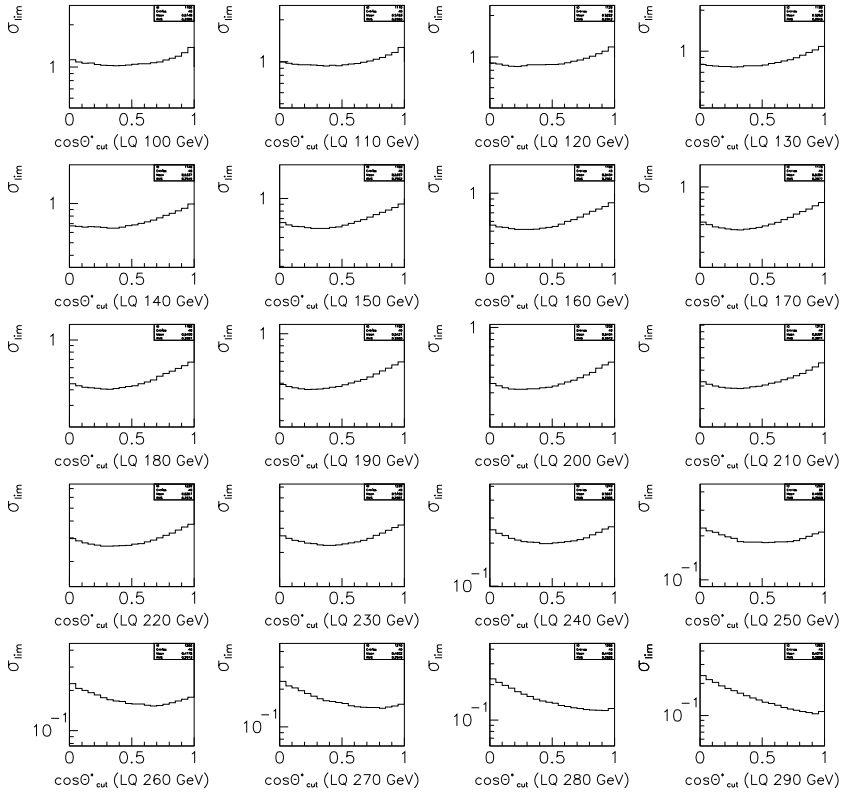

Figure 8.4: Example distributions of $< \sigma_{lim} >$ as a function of $\cos\theta^*$ cut for different LQ Monte Carlo samples (e^+p sample). The minimum $< \sigma_{lim} >$ on this plot determines the final optimized cut for each LQ mass.

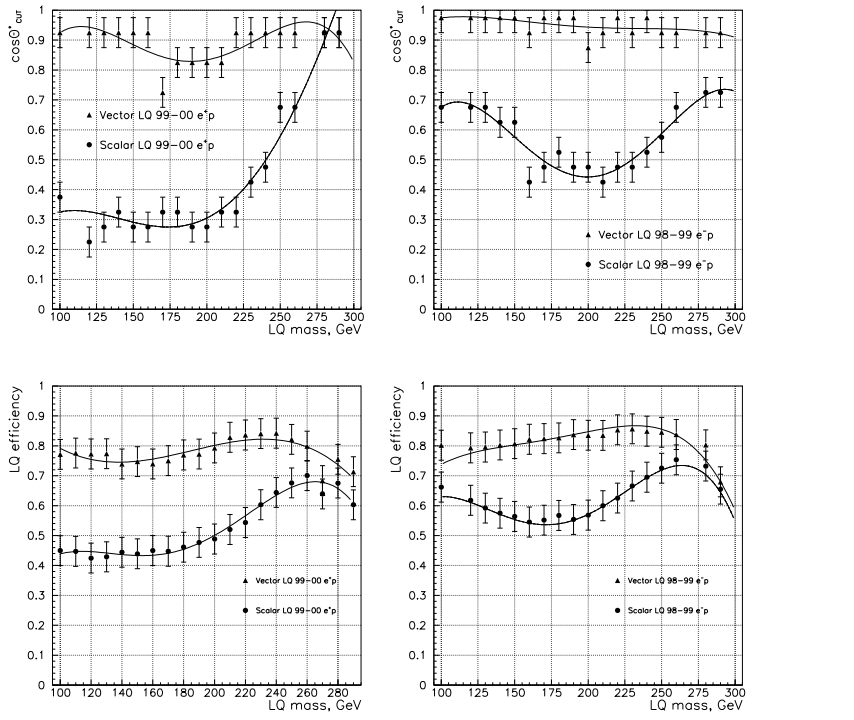

Figure 8.5: Optimized $\cos\theta^*$ cut for e^+p sample (upper left) and e^-p sample (upper right). Leptoquark efficiency after applying additional mass window and optimized $\cos\theta^*$ cut for e^+p leptoquark Monte Carlo sample (lower left) and e^-p leptoquark Monte Carlo sample (lower right).

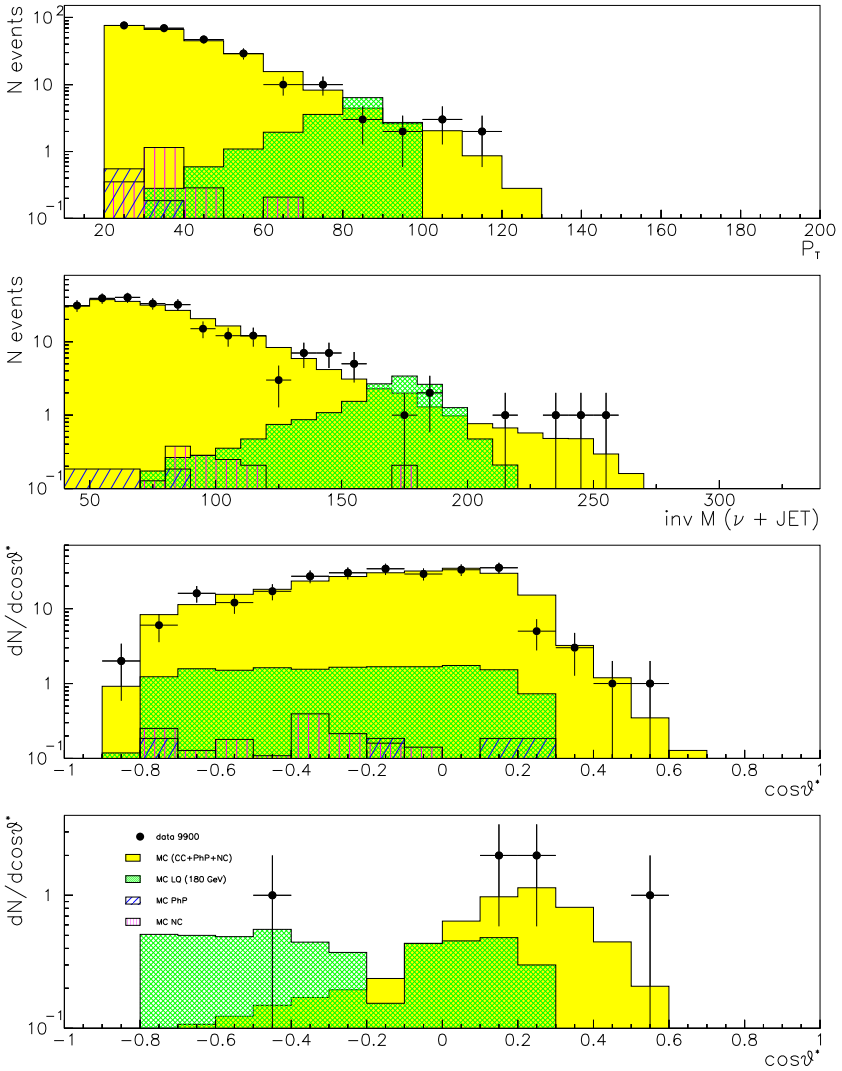

Figure 8.6: The distributions of P_T^{mis}, $M_{\nu j}$, and $\cos\theta^*$ after applying mass window and $\cos\theta^*$ cuts for the e^+p data. The lower figure shows the $\cos\theta^*$ distribution for $M_{\nu j} > 180\ GeV$.

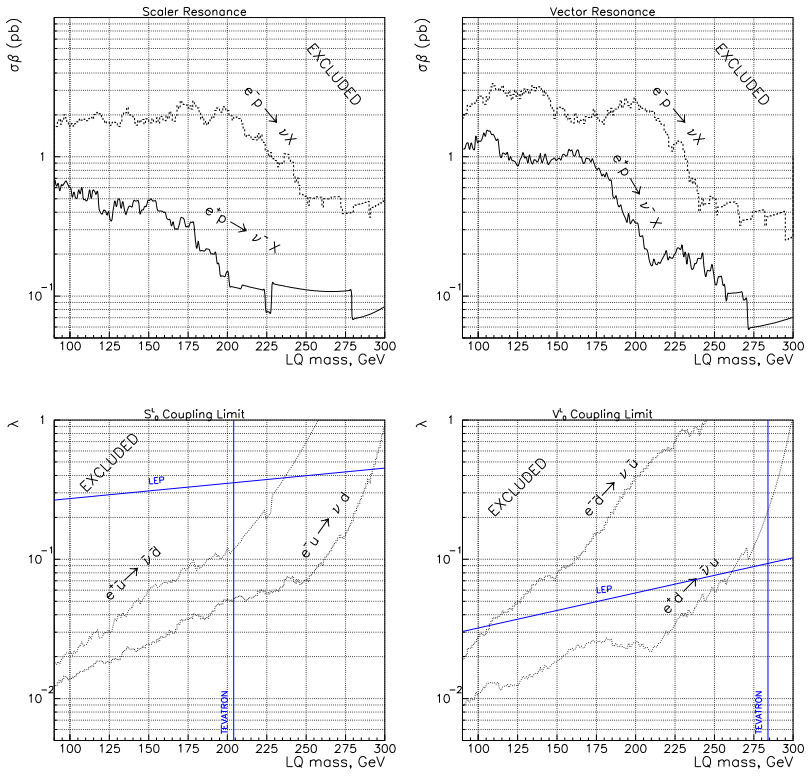

Figure 8.7: $\sigma \cdot \beta$ 95% CL limits for scalar (upper left) and vector (upper right) leptoquarks as a function of LQ mass. Limits on λ for scalar (lower left) and vector (lower right) leptoquarks as a function of LQ mass.

8.2 Likelihood Method

In the previous section NWAM was used under the assumption that the width of the resonance is sufficiently small and the coupling is small ($\lambda < 1.0$). When the coupling is large ($\lambda \simeq 1$) NWAM no longer provides a correct estimate of the resonant cross-section. The full LQ differential cross-section, as described in section 2.5.2, has been used for calculating the Likelihood limits. This method enables us to extend the limit range to beyond the HERA kinematic limit. The coupling strength limit, λ_{LQ}, of the 4 BRW LQs which couple to νq, listed in Table 2.4, were calculated as a function of the LQ mass.

Limit setting procedure

The phase space in the $M_{\nu js} - \cos\theta^*$ plane bounded by $100 \leq M_{\nu js} \leq 280\ GeV$ and $-1.0 \leq \cos\theta^* \leq 1.0$ is divided into 18×10 bins in steps of 10 GeV in $M_{\nu js}$ and steps of 0.2 in $\cos\theta^*$. Inside each bin the number of charged current events expected is counted from CC Monte Carlo samples. The number of observed events from the data sample are also counted inside each bin (see Fig. 8.8). Good agreement between data and MC prediction can be seen.

The charged current Monte Carlo events inside each bin is re-weighted by

$$WF = 1.0 + \frac{\frac{d^2\sigma^{int}}{dxdy} + \frac{d^2\sigma^{LQ}}{dxdy}}{\frac{d^2\sigma^{SM}}{dxdy}} = WF(x, y, M_{LQ}, \lambda_{LQ}), \tag{8.5}$$

using the true x and y [69]. The weighting factor is a function of mass and coupling constant of the leptoquark. It is also a function of the true x and y for that particular Monte Carlo event.

In each $M_{\nu js} - \cos\theta^*$ bin the probability of having N_i^{obs} while expecting N_i^{exp} is

$$p_i(M_{LQ}, \lambda_{LQ}) = \frac{e^{-N_i^{exp}}(N_i^{exp})^{N_i^{obs}}}{N_i^{obs}!} \tag{8.6}$$

Taking into account all bins, the total probability is:

$$P(M_{LQ}, \lambda_{LQ}) = \prod_i p_i(M_{LQ}, \lambda_{LQ}) \tag{8.7}$$

For each leptoquark mass M_{LQ}, the 95% CL λ_{LQ} limit can be defined as

$$\int_0^{\lambda^2_{lim}} P(\lambda)d\lambda^2 = 0.95 \int_0^{\infty} P(\lambda)d\lambda^2 \tag{8.8}$$

Fig. 8.9 shows an example of the full probability $P(\lambda)$ distribution as a function of λ at two different masses. The full integral of probability $F(\lambda) = \int_0^{\lambda} P(\lambda_0)d\lambda_0$ as a function of λ for BRW leptoquark S_0^L at two different mass points are shown in two lower plots.

The effect of systematic errors have been estimated by re-weighting the number of expected events by $\pm 1\sigma$ and comparing the limit calculated with these extremes. The final limit is calculated by:

$$\lambda_{lim}^{sys} = \frac{\lambda_{lim}^{Nom} + \lambda_{lim}^{+1\sigma} + \lambda_{lim}^{-1\sigma}}{3}$$

.

The difference between λ_{lim}^{sys} and λ_{lim}^{Nom} are less then 1% in the mass range $100 - 400\ GeV$.

8.3 Frequentist Likelihood Method

The two-dimensional Likelihood Method shows good results, as described above, but this method has an open question. In Eq. 8.8 the integral is integrated over λ^2, but this is not required and integrating over λ, λ^3, etc. will result in different limits for λ. Therefore a new method for setting the coupling limit has been used, the so-called 'frequentist likelihood method'. The same experiment was repeated many times, using the Standard Model MC sample. The percentage of experiments which have a limit less than found in the data was calculated. The procedure is repeated for different λ_{LQ} until this percentage is $\sim 95\%$.

Limit setting procedure

The $M_{\nu js} - \cos\theta^*$ phase space between (100 to 280 GeV) and (-1.0 to 1.0) is again divided into 18×10 bins in steps of 10 GeV in $M_{\nu js}$ and 0.2 in $\cos\theta^*$. Inside each bin the number of expected charged current events, N_i^{exp}, are counted from CC Monte Carlo samples. The number of observed events, N_i^{obs}, from the data sample are also counted inside each bin.

In each bin the Poisson probability, $p_i(N_i^{obs}, N_i^{exp})$, of having N_i^{obs} while expecting N_i^{exp} events is calculated, see Eq. 8.6, from which the total probability is calculated:

$$P(N^{obs}, N^{exp}) = \prod_i p_i(N_i^{obs}, N_i^{exp}) \tag{8.9}$$

Charged current Monte Carlo events inside each bin were re-weighted by Eq. 8.5, using true x and y (N_i^{REW}). N_i^{REW} was taken as mean value for a Poisson distribution to generate $j = 1...1000$ experiments ($N_i^{REW-zeus\ j}$). In each bin and for each of the 1000 simulated experiments the Poisson probability, $p_i^j(N_i^{REW-zeus\ j}, N_i^{exp})$, of having

$N_i^{REW-zeus\ j}$ while expecting N_i^{exp} events is calculated, from which the total probability is calculated:

$$P^j(M_{LQ}, \lambda_{LQ}) = \prod_i p_i^j(N_i^{REW-zeus\ j}, N_i^{exp}) \tag{8.10}$$

For each leptoquark mass M_{LQ}, one can calculate the fraction $\alpha(M_{LQ}, \lambda_{LQ})$ of simulated experiments with a total probability $P^j(M_{LQ}, \lambda_{LQ})$ greater than the actual ZEUS measurement $P(N^{obs}, N^{exp})$. The procedure is repeated for different λ_{LQ} until $\alpha(M_{LQ}, \lambda_{LQ})$ is approximately 0.95 ($\alpha(M_{LQ}, \lambda_{LQ}^{lim}) \sim 0.95$). Systematic errors are taken into account in a similar way as in the previous section (see. 8.2). The resulting limit variations are less than 1% in the mass range $100 - 400\ GeV$.

8.4 Results

Fig. 8.10 shows the comparison of Narrow Width approximation, Likelihood and Frequentist methods for coupling limits on the scalar and vector BRW leptoquarks with $F = 0$ and $F = 2$. For Likelihood and Frequentist methods the limits were extended beyond the center-of-mass energy.

The limit on λ_{LQ} at $M_{LQ} = 400$ GeV range from 0.2 to 0.5 depending on the LQ type. Also shown are the limits on S_0 and V_0 LQ from D0 (Tevatron) , OPAL (LEP) and L3(LEP) experiments. The results are better than LEP limits below 270 GeV.

Fig. 8.11 shows the coupling limits as a function of leptoquark mass for S_0, S_1, V_0 and V_1 leptoquark types using the Frequentist method. They have been extended beyond the center-of-mass energy. The area above the curve is excluded by this analysis. The results using the Frequentist method are slightly above the NWA limit and the limit set using the Likelihood method. One explanation for this is that the normalization of data from the Monte Carlo is responsible. In order to confirm this the same limit setting procedure has been performed normalizing to the number of events found. The resulting differences between the Frequentist method with and without normalization are less then 1%.

The excluded mass regions using the Frequentist method with the assumption of a BRW LQ with $\lambda = 0.1$ and $\lambda = 0.31$ for the 4 BRW LQs are summarized in Table 8.1. They range from 265 GeV to 270 GeV for $\lambda = 0.1$ and from 300 GeV to 400 GeV for $\lambda = 0.31$.

Table 8.1: Mass limit of the 4 BRW LQs at $\lambda = 0.1$ and $\lambda = 0.31$.

	S_0^L	S_1^L	V_0^L	V_1^L
M(GeV) $\lambda = 0.1$	260	262	257	264
M(GeV) $\lambda = 0.31$	307	380	308	400

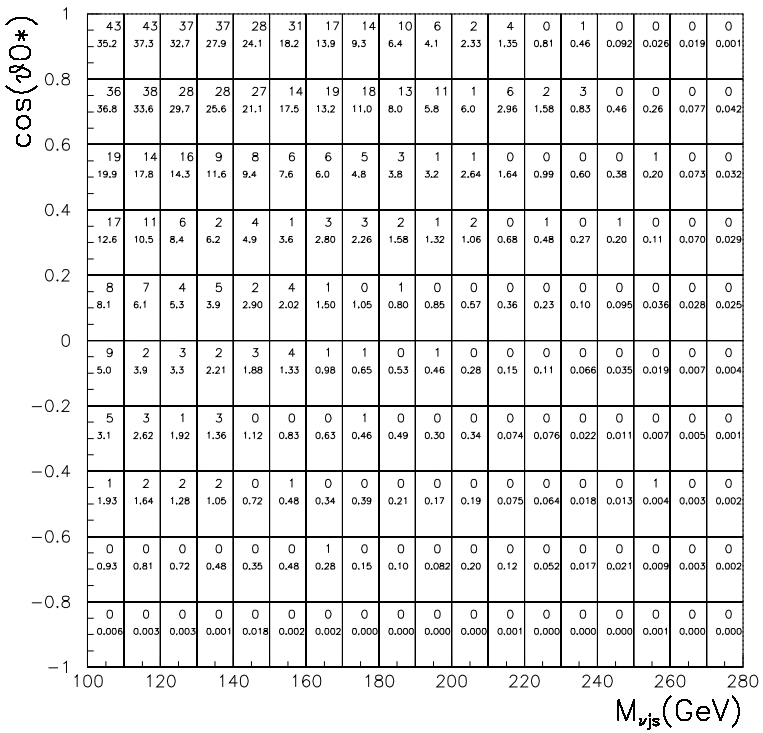

Figure 8.8: Number of data (large digits) and Standard Model expected events (small digits) in the plane $M_{\nu js}$ vs $\cos\theta^*$.

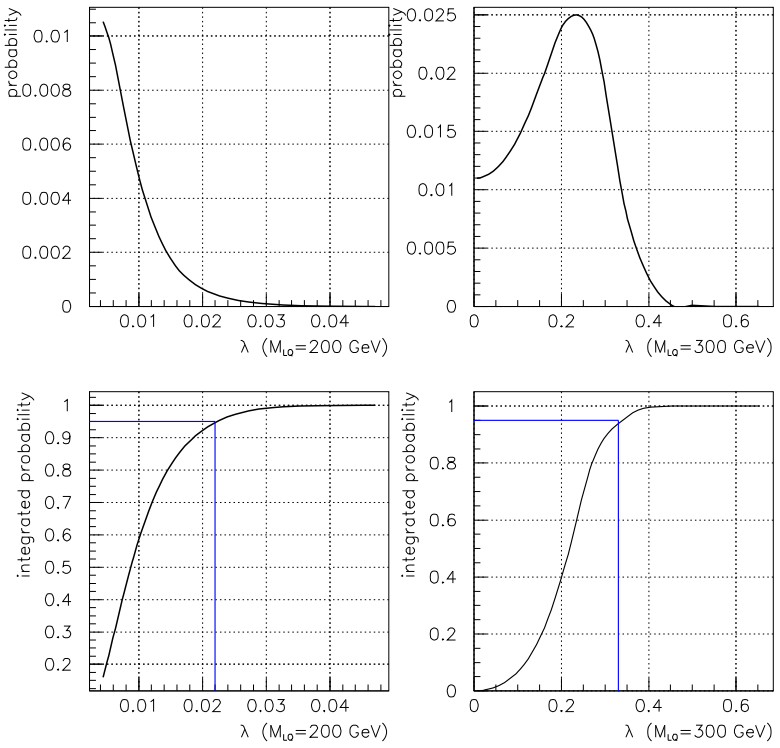

Figure 8.9: The full probability $P(\lambda)$ as a function of λ at two different masses is shown in the two upper plots. The full integral of probability $F(\lambda) = \int_0^{\lambda} P(\lambda_0) d\lambda_0$ as a function of λ for BRW leptoquark S_0^L at two different masses (lower plots). The vertical lines on the plots show the limit on λ, where $F(\lambda) = 0.95$.

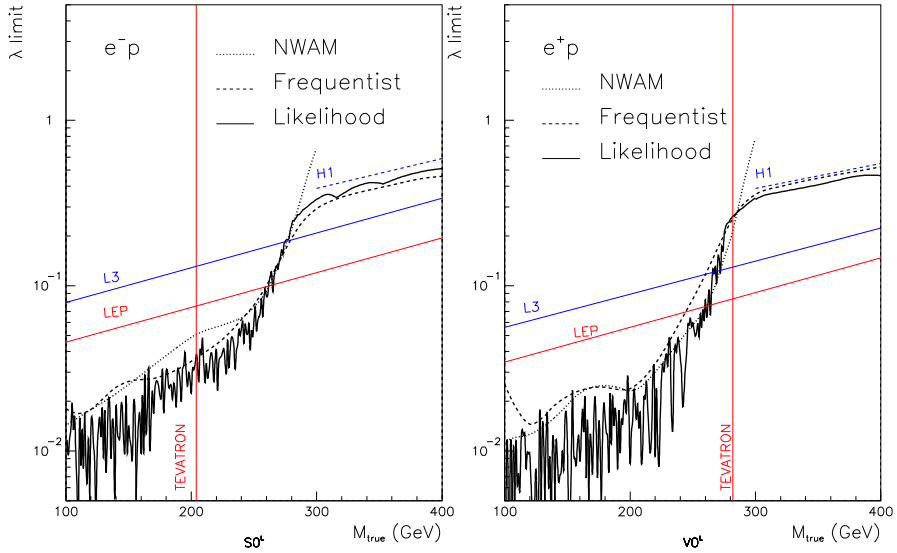

Figure 8.10: The comparison of NWA, Likelihood and Frequentist limits for S0 (left plot) and V0 (right plot) leptoquarks using e^-p data and e^+p data. Limits reported by the D0 experiment at the Tevatron and from OPAL and L3 experiments at LEP are also shown.

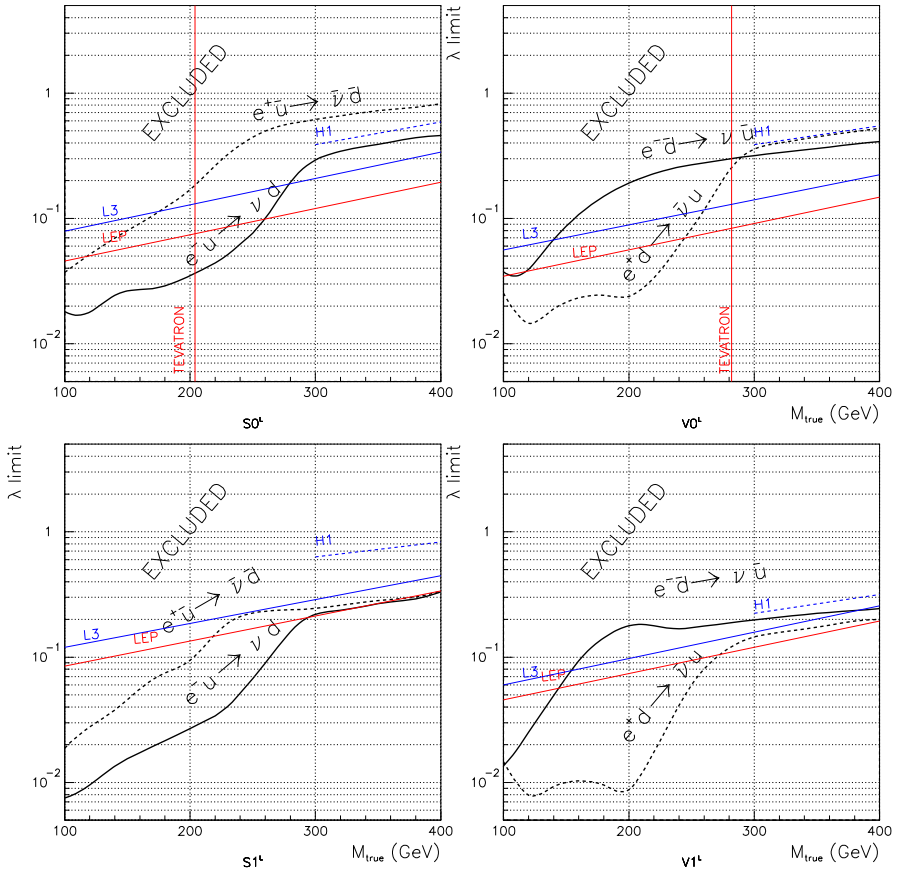

Figure 8.11: Coupling limits as a function of leptoquark mass for S0, V0,S1 and V1 leptoquarks for e^-p and e^+p data using Frequentist method. Limits reported by the D0 experiment at the Tevatron and from OPAL and L3 experiments at LEP are also shown.

Chapter 9

Artificial Neural Network Selection

The goal of the analysis described in this chapter is to improve the background rejection and signal efficiency obtained in the preceeding analysis by using an Artificial Neural Network (ANN) [70].

9.1 Introduction

9.1.1 Multivariate classifiers

A classifier is any procedure that assigns objects to classes. In this analysis a classifier is defined which separates signal events from the background. The standard classification methods, e.g. the analysis methods used in the previous chapters, of examining 1-dimensional (uni-variate) and 2-dimensional (bi-variate) distributions of variables to optimize cuts for separating signal and background events do not in general provide the maximum possible discrimination when correlations exist between variables. Multivariate classifiers which fully exploit the correlations that exist among several variables provide a discriminating boundary between signal and background in multi-dimensional space that can yield discrimination close to the theoretical maximum.

In the multivariate approach, each event is encoded as a point in a multi-dimensional space, called *feature space*, corresponding to a vector x of feature variables such as E_T^H of the hadronic system, scattered angle of neutrino, $(E-P_z)^H$ of the hadronic system, etc. This feature space is then mapped into an output space of lower dimensionality in such a way that the signal and background vectors are mapped onto different regions of space. The aim of the multivariate method is to reduce the dimensionality of the problem without losing information.

9.1.2 Artificial neural network

ANNs are examples of multivariate methods. In the past decade neural network methods have become one of the more favored techniques for separating signal from background samples. Artificial neural networks provide a powerful new method for event classification. In computer science literature many variations of the neural network approach exist [71], but in high energy physics [72] the principle type used is called a feed-forward multilayer perceptron, which is trained using a backpropagation algorithm. The representation of a three layer feed-forward neural network with one hidden layer is shown in Fig. 9.1.

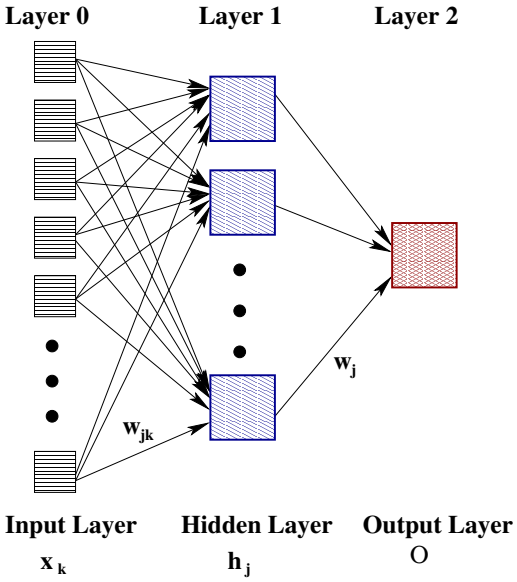

Figure 9.1: A feed-forward Neural Network with one hidden layer.

The nodes in the input layer correspond to the components x_k of the feature vector x, and the output layer has a single node commonly used in binary classification problems. The network builds an internal representation of the mapping of the feature space into the output space. The output of the network is given by

$$O(x) = g(\sum_j w_j g(\sum_k w_{jk} x_k + \theta_j) + \theta), \tag{9.1}$$

where the weights, w_{jk} and w_j, and the thresholds, θ_j and θ, are parameters that are adjusted during the training process. The quantity g is a non-linear transfer function of the form $g(y) = 1/(1+e^{-2y})$. The use of transfer functions to allow the mapping of any

real function is described elsewhere [73]. The parameters are determined by minimizing the mean square error between the actual output O^p and the desired output t^p

$$E = \frac{1}{2N_p}\sum_{p=1}^{N_p}(O^p - t^p)^2 \tag{9.2}$$

with respect to the parameters. Here p denotes a feature vector or *pattern*. Once the parameters are determined using a large number of signal and background events the network can be used to classify events. It has been shown [74] that the feed-forward neural network when trained as a classifier using the back-propagation algorithm for updating the parameters, yields an output that approximates the Bayesian probability for the signal. Back-propagation is in essence a gradient descent, starting with random weights and thresholds.

The aim is to reduce the error function which is essentially a chi-square quantity, the sum of the squared deviations of the neural network output from the desired output for signal (usually 1) and background (usually 0). Then the trained network with its optimized weights and thresholds is used with real events, and the net output for each event is the statistic on which a decision about signal selection is made. Usually the output ranges from 0 to 1 continuously.

The best known and most widely used neural net software is JETNET [75] which was used in this thesis.

9.2 Background rejection

The rejection of *ep* backgrounds are described. Note that non-*ep* background Monte Carlo samples to train the Neural Network do not exist and, consequently, these events have been rejected by applying the cuts described in section 7.2 before the Neural Network selection.

Based on a study of various Monte Carlo distributions, the following 8 variables were chosen as inputs to the Neural Network (see Fig. 9.2):

1. E_T^H - transverse energy of the hadronic system
2. E_T^{jet}/E_T^H - fractional transverse energy of the most energetic jet w.r.t. the energy of the hadronic system
3. $P_T^H/\sqrt{E_T^H}$ - fractional transverse momentum of the hadronic system w.r.t. the squareroot of the transverse energy of the hadronic system
4. $(E-P_z)^H$ - longitudinal energy of the hadronic system
5. Q_H^2 - momentum transfer squared of the hadronic system

6. Y_{YB} - fractional energy transfer
7. θ_ν - scattering angle of the neutrino
8. γ_h - scattering angle of the hadronic system

As can be seen from this list the mass variables (invariant masses of ν+jet or x) were not used for training in order to avoid selection with a particular mass. The resulting mass distributions were used to control the output data.

All the variables defined previously have been combined in a Neural Network using the package JETNET 3.4 [75]. One major difference between JETNET 3.4 and other versions is the existence of several alternative learning algorithms. Back-propagation is the most widely used learning algorithm for the weights update. The Rprop method was reported to outperform all other learning algorithms, both in speed and quality. Back-propagation, Manhattan and Rprob have been tested and the Rprop method was chosen as it showed the best results.

Various combinations of the number of input variables and hidden nodes have been investigated. The network chosen, for this analysis, has 8 input nodes, 17 hidden nodes, and one output. After initialization, the network has been trained using $\sim$ 6000 events with $E_T^{had} > 40$ GeV of direct photoproduction Monte Carlo, $\sim$ 4000 events with $E_T^{had} >$ 40 GeV of resolved PhP Monte Carlo, $\sim 10^6$ events of neutral current Monte Carlo, $\sim$ 400000 events of charged current Monte Carlo and $\sim$ 4000 events of leptoquark Monte Carlo for each leptoquark mass. A detailed description of all Monte Carlo samples is given in section 5.

Several combinations of background and signal samples are used for training (see Table 9.1):

Table 9.1: Background and signal samples used for training.

Background processes	Signal processes
PhP dir + PhP res + NC	LQ (100 or...290 GeV) + CC
PhP dir + PhP res + NC	all LQ (100 and...290 GeV) + CC
PhP dir + PhP res + NC	all LQ (100 and...290 GeV)

After training is completed, independent samples of Monte Carlo events of each type have been used as input for the trained net. An example of the output value of the ANN after training on all LQ masses and CC as signal events is shown in Fig. 9.3. The signal and background curves are very well separated, with continuum background events (direct PhP, resolved PhP, neutral current MC) accumulating around 0 and signal events (charged current MC and leptoquark MC) around 1.

To evaluate the rejection power of the Neural Network a cut is set on the output such that the efficiency for the LQ signal for the mass range 130 GeV to 290 GeV is $> 90\%$, which corresponds to requiring an output greater than 0.5. The fraction of background events surviving the cut is $\sim 0.09\%$ for PhP (direct and resolved) and $\sim 2.3 \cdot 10^{-5}$ % for

NC events. When normalized to the luminosity of data this percentage corresponds to the total number of ~ 2.3 events for PhP and ~ 0.01 events for NC samples.

9.3 Search results

After the Neural Network and non-ep background rejection 729 events are selected from the e^+p data while 689 events are expected from the Standard Model. For e^-p data 509 events are selected and 464 events are expected. The number of observed events are in good agreement with the Standard Model prediction.

The number of observed events and number of expected events from the Standard Model are shown in Table 9.2 for the standard charged current cut selection and for Neural Network selection.

Table 9.2: Comprasion of standard cut selection and Neural Network selection

Data sample	Cuts		Neural Network	
	N_{obs}	N_{exp}	N_{obs}	N_{exp}
e^+p	1196	1122.	729	685
e^-p	719	705.6	509	464

Fig. 9.4 shows distributions of 8 input variables after Neural Network and non-ep background cuts are applied. Good agreement between data and Monte Carlo prediction are observed.

The Q^2 , x and y distributions show good agreement between data and Monte Carlo, see Fig. 9.5. As can be seen from these plots the event with $Q^2 \sim 50000\ GeV^2$ is also selected by the Neural Network.

The invariant mass spectra calculated using the four different methods, described previously, are shown in Fig. 9.6 for e^+p data after Neural Network selection and all non-ep background cuts have been applied. A slight excess of events compared to prediction is seen in the high mass region of the plots. Fig. C.3 shows a typical high $M_{\nu j}$ event with $M_{\nu j} = 247 GeV$ ($M_{\nu had} = 370\ GeV$, $M_{\nu js} = 268\ GeV$, $Q^2 = 8100\ GeV^2$, and $\cos\theta^* = 0.733$). Most events with $M_{\nu j} \gtrsim 250\ GeV$ have energetic jets very close to the FCAL first inner ring, which suggests that they are incorrectly measured. Other explanations, e.g. non-resonance proton remnant effects, may cause the excess.

The $\cos\theta^*$ distributions are shown in Fig. 9.7 for all data and for events with $M_{\nu j} > 180\ GeV$.

The LQ efficiency after training on all LQ mass samples are compared with the efficiency of the previous chapters cut analysis (with non-ep background rejection cuts and standard cut selection) in Fig. 9.8 as a function of leptoquark mass. It is evident that the Neu-

ral Network selection has a superior leptoquark efficiency. As mentioned above non-ep rejection was performed using the standard cuts as no MC sample is available for non-ep background channels, consequently the ANN used, the intermediate curve, is not as efficient as it could be.

From Table 9.3 it can be seen that the Neural Network selection gives a better efficiency for leptoquarks ($\sim 87\%$) while reducing significantly the PhP and NC efficiency, when compared to the cut selection. The LQ efficiency for the standard charged current cut selection is $\sim 80\%$.

Table 9.3: Comparison of standard cut selection and Neural Network selection. Efficiency and number of observed events are normalized to the luminosity of data.

	Cuts		Neural Network	
	Efficiency	N_{events}	Efficiency	N_{events}
Data 9900 efficiency	0.20%	1194.	0.12%	729.
CC efficiency	45.2%	1122.0 ± 3.5	27.6%	685.0 ± 2.5
LQ efficiency	80.55%	27.7 ± 5.0	86.86%	29.9 ± 5.2
PhP dir efficiency	0.33%	3.7 ± 0.8	0.10%	1.1 ± 0.4
PhP res efficiency	0.12%	1.9 ± 0.9	0.07%	1.2 ± 0.6
NC efficiency	$5 \cdot 10^{-3}\%$	2.3 ± 0.2	$2.3 \cdot 10^{-5}\%$	0.011 ± 0.002

No significant signal is found, and limits are derived on resonant production as a function of leptoquark mass using the Frequentist method (see Fig. 9.9).

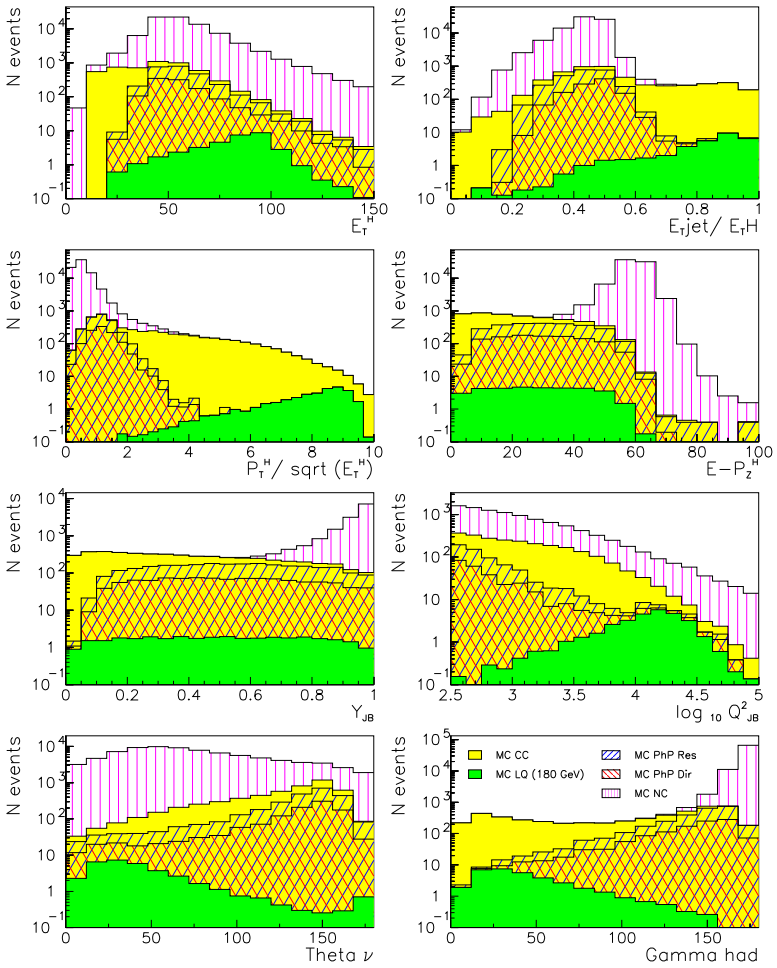

Figure 9.2: Distribution of input variables which was used for Neural Network training (E_T^H ,E_T^{jet}/E_T^H, $P_T^H/\sqrt{(E_T^H)}$, $(E-P_z)^H$, Q^2_H, Y_{JB}, θ_ν, and γ_h) for different MC samples.

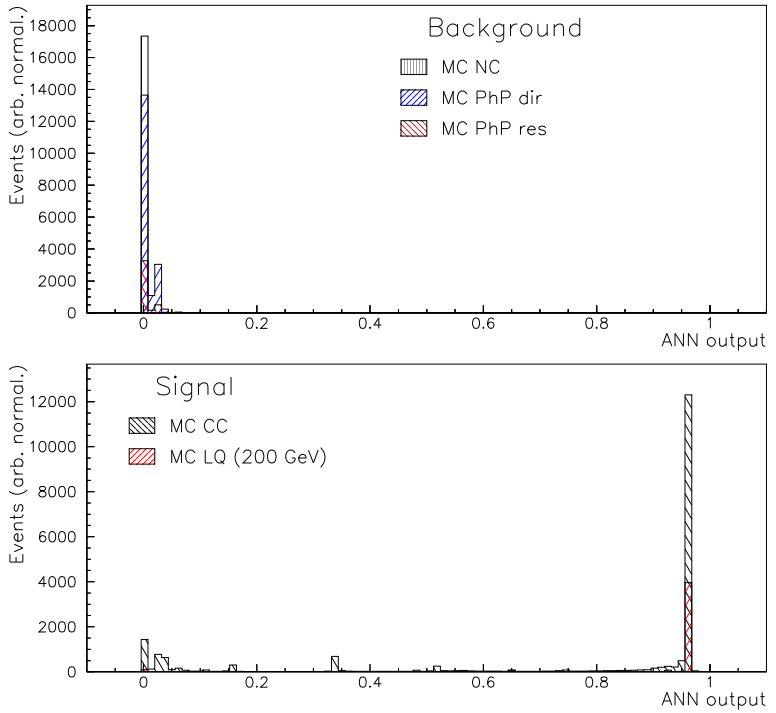

Figure 9.3: Distribution of output values of the Neural Network after training on all LQ masses.

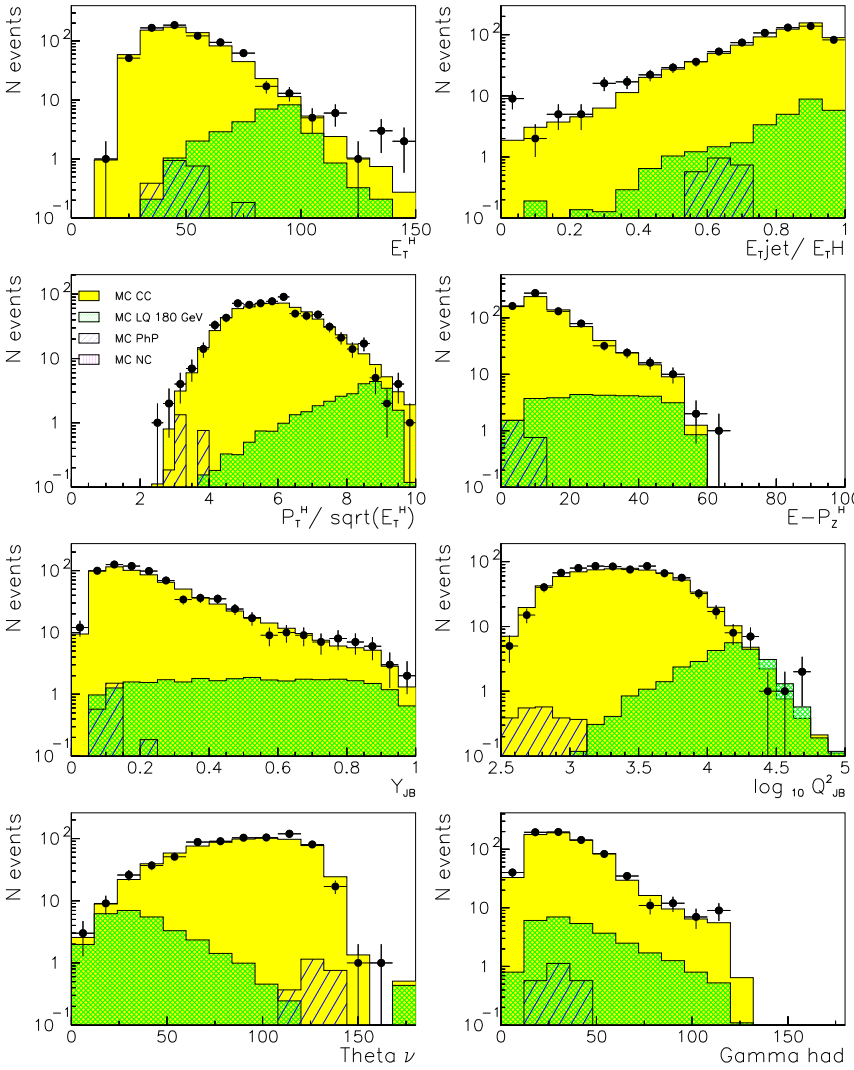

Figure 9.4: Input train variables after Neural Network selection and non-ep background cuts are applied.

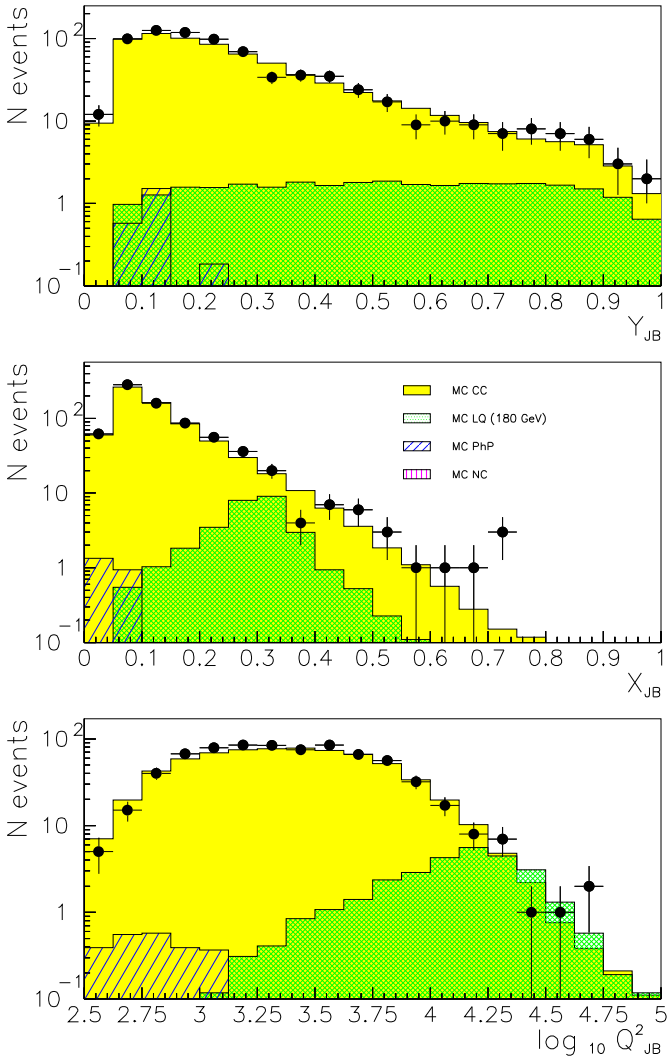

Figure 9.5: The Y_{JB}, X_{JB}, and $\log_{10}(Q^2)$ distributions for data and MC after Neural Network selection and all non-ep background cuts are applied.

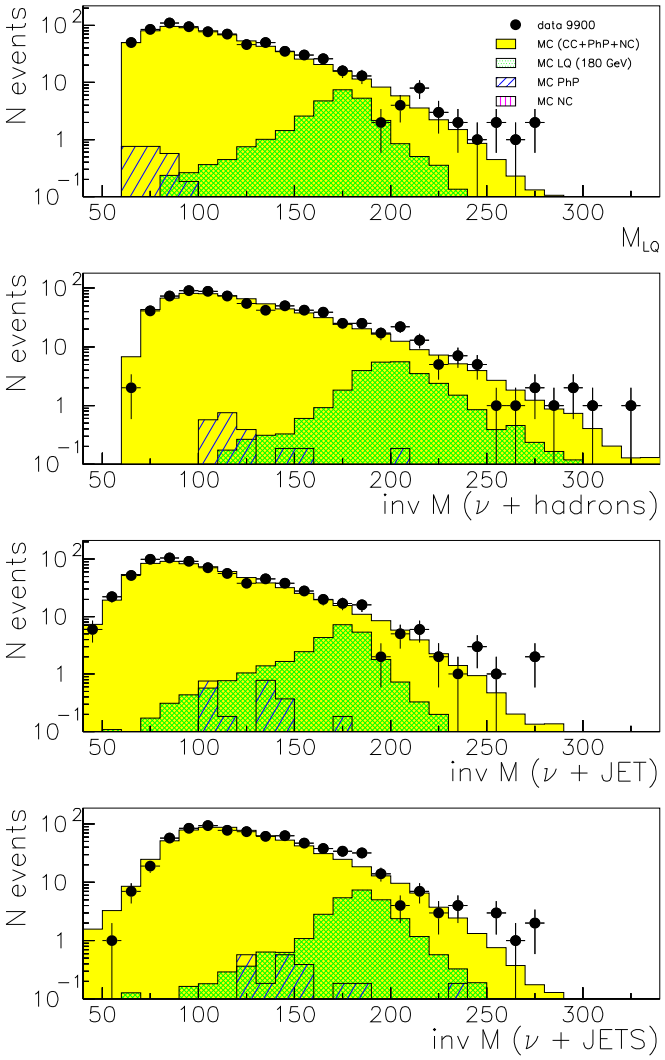

Figure 9.6: Mass spectra for e^+p data for different methods of mass reconstruction after Neural Network selection and all non-ep background cuts are applied.

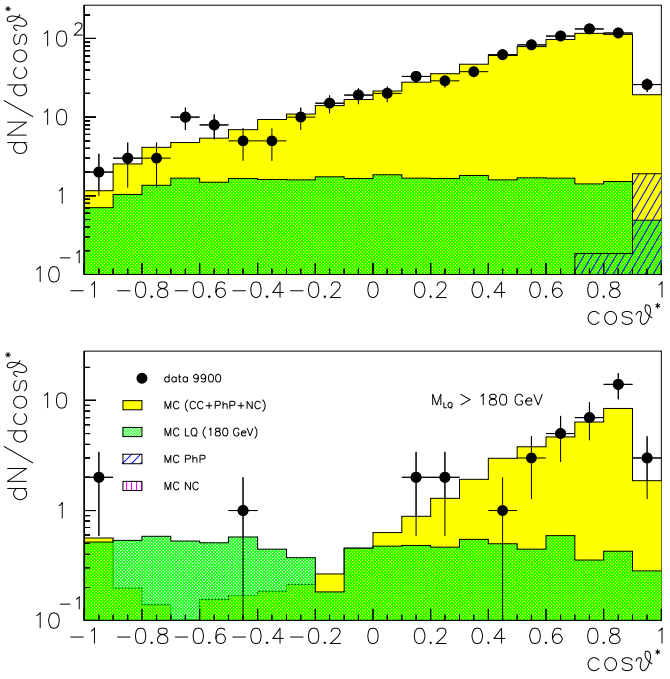

Figure 9.7: The $\cos\theta^*$ distributions for e^+p data passing the Neural Network selection and non-ep background cuts and MC predictions. Upper and lower plots show all data and events with $M_{\nu j} > 180\ GeV$, respectively.

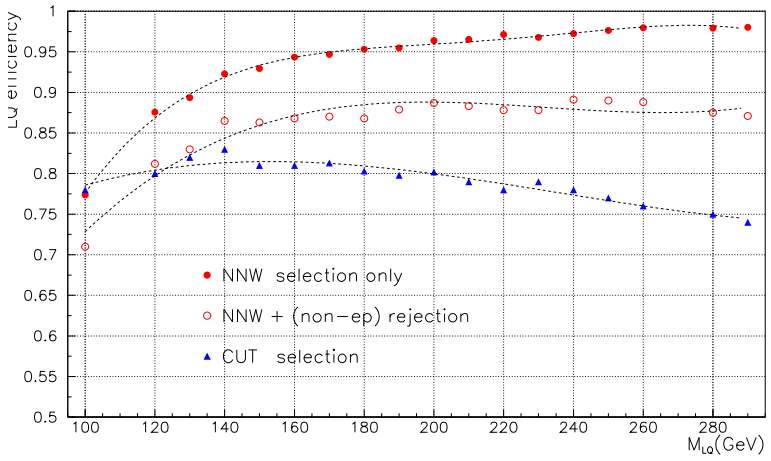

Figure 9.8: LQ efficiency after Neural Network selection and charged current cut selection.

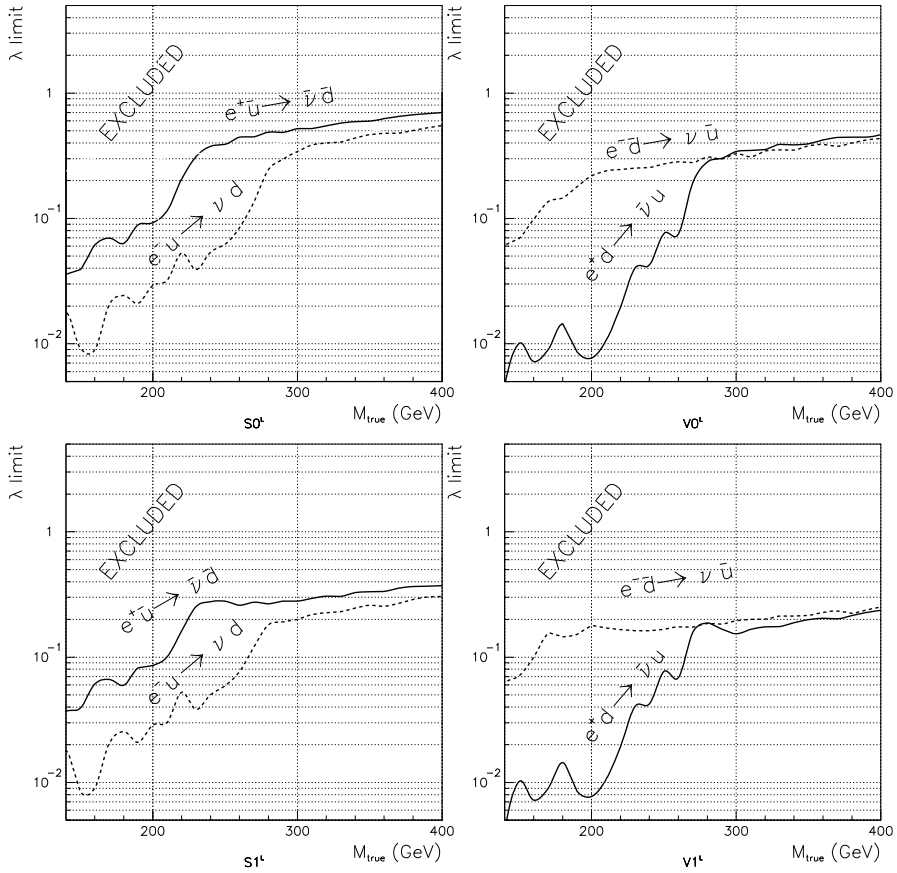

Figure 9.9: Coupling limits as a function of leptoquark mass for BRW LQ V_0^L, BRW LQ V_1^L, BRW LQ S_0^L and BRW LQ S_1^L, derived from e^-p and e^+p data samples. The ANN selection is used together with the Frequentist method.

Chapter 10

Search for Other Exotics in events with P_T^{mis}

In section 2.6 the importance of the missing transverse momentum, P_T^{mis}, event signature when searching for physics beyond the Standard Model was emphasized. In this chapter a search for events with P_T^{mis} and electrons or jets, see table 10.1, in the final state are presented. The results of the search are rudimentary in the sense that production cross-section limits are not derived. Some of the channels are analyzed for the first time at ZEUS. The datasets and data handling techniques used in the leptoquark search have been reused where applicable.

10.1 Selection Cuts and Background Rejection

The initial event selection is performed using standard charged current selection criteria. The missing momentum is required to satisfy $P_T^{miss} > 20$ GeV and is assigned to a massless neutrino, ν, which escapes detection.

Electron identification is performed using standard ZEUS electron identification tools and the following cuts:

- Probability > 0.001 for energy > 4 GeV.
- For electrons with $\theta_e > 0.3$, a track with distance of closest approach to the calorimeter cluster of less than 10 cm, $P_e/E_e > 0.25$, and $P_T^e > 5$ GeV is required.
- For electrons with $\theta_e < 0.3$, $P_T^e > 30$ GeV is required.

Jets are required to have $|\eta^{jet}| < 2.6$ and $E_T^{jet} > 10$ GeV.

Non-ep background rejection has been applied as described in section 7.2. For event classes without electrons the neutral current rejection described in section 7.5 has been applied.

10.2 Results

By plotting all combinations of invariant masses in the event and comparing with the Standard Model Monte Carlo distribution, good overall agreement between data and expectation for most of the event classes, see table 10.1, is found. Note that the contribution from PhP is negligible except in the high jet multiplicity classes.

Table 10.1: The data and Standard Model expectation for all event classes with data events.

Process	CC	DATA for e^+p
$\nu + e + e$	11.4	13
$\nu + e + j$	129.4	142
$\nu + j + j$	100.6	107
$\nu + e + j + j$	14.2	14
$\nu + e + e + j$	11.4	13
$\nu + e + e + e$	0.7	1
$\nu + j + j + j$	5.1	4
$\nu + e + e + j + j$	1.7	1
$\nu + e + j + j + j$	1.0	1
$\nu + e + e + e + j$	0.1	0
$\nu + e + e + e + e$	0.0	0
$\nu + j + j + j + j$	0.2	0

No events have been observed in the classes $\nu + e + e + e + j$, $\nu + e + e + e + e$, and $\nu + j + j + j + j$. The number of CC events expected are 0.1, 0.0 and 0.2, respectively. Those event classes where events are found are reviewed below.

$\nu + e + e$

All possible invariant mass combinations for the final state $\nu+e+e$ (P_T^{mis} + first electron, P_T^{mis} + second electron, first electron + second electron, P_T^{mis} + two electrons) are shown in Fig. 10.1. 13 events are found while 11.4 are expected from the Standard Model. Good agreement between data and Monte Carlo has been observed. One event is found with M(P_T^{mis} + first electron) $\sim$ 170 GeV, whilst 1.4 events with mass above 70 GeV and 0.19 events with mass above 100 GeV are expected from the SM. This event was already discussed in section 7.6 and an event display of this event can be found in Fig. C.1. Since this analysis is not exclusive the event can appear in other investigated classes (see Figs. 10.2).

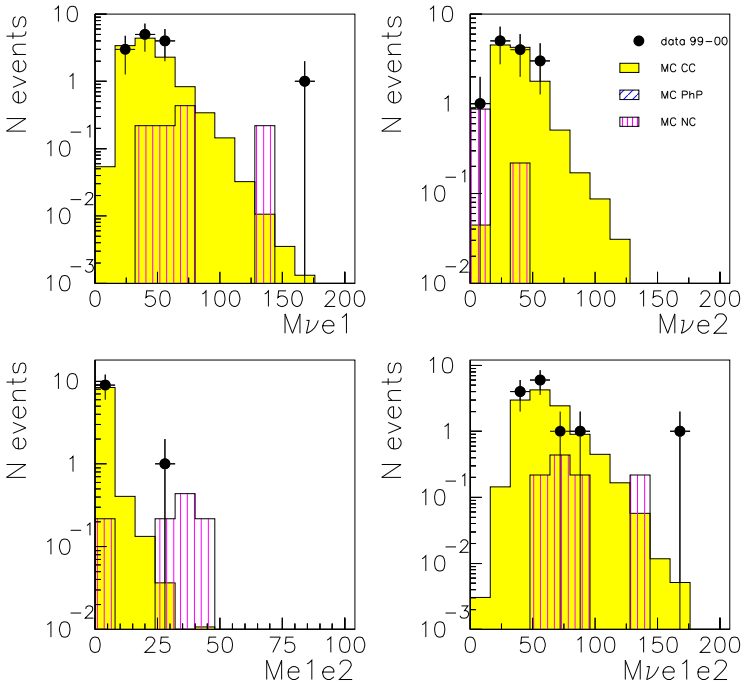

Figure 10.1: All possible combinations of invariant mass distribution of the final state $\nu + e + e$. Symbols denote P_T^{mis} (ν), first electron and second electron, respectively.

$\nu + e + j$

Fig. 10.2 shows all possible invariant mass combinations for the final state $\nu + e + j$. The Monte Carlo distribution is describes well the data points. The principle background comes from neutral current DIS events. In the invariant mass distribution P_T^{mis} + electron (upper left plot) one event is found with mass $\sim$ 170 GeV, whilst 0.8 events are expected from the Standard Model with mass above 120 GeV.

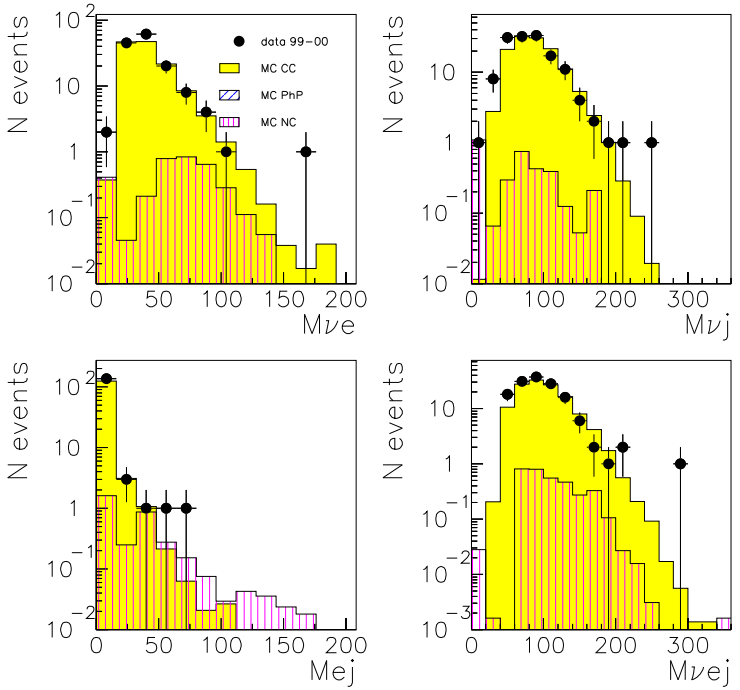

Figure 10.2: All possible combinations of invariant mass spectra of the final state $\nu+e+j$. Symbols ν, e, j denote P_T^{mis} (ν), electron and jet, respectively.

$\nu + j + j$

In the event class $\nu + j + j$, 107 events are found, whilst 100.6 are expected from the Standard Model. The principle background comes from photoproduction events. The shape of the invariant mass distributions are well described by the Monte Carlo. No events with mass above 200 GeV are found.

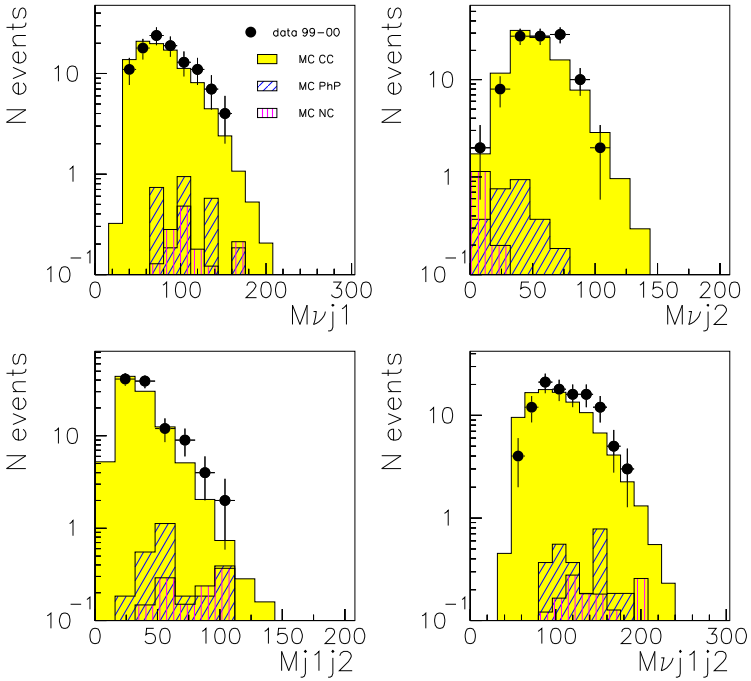

Figure 10.3: All possible combinations of invariant mass spectra of the final state $\nu+j+j$. Symbols denote P_T^{mis} (ν), first jet and second jet, respectively.

$\nu + e + j + j$

The data are well described by the Standard Model Monte Carlo in all invariant mass distributions of the final state with P_T^{mis}, one electron and two jets (Fig. 10.4). 14 events are found and 14.2 events are predicted by the Standard Model. The principle background contribution to this event class comes from neutral current DIS events. One event with $M_{ej1} \sim 70$ GeV is found in the data, see Fig. 10.4, whilst 0.55 events are expected from the Standard Model with $M_{ej1} > 40$ GeV. The observed event is displayed in Fig C.7.

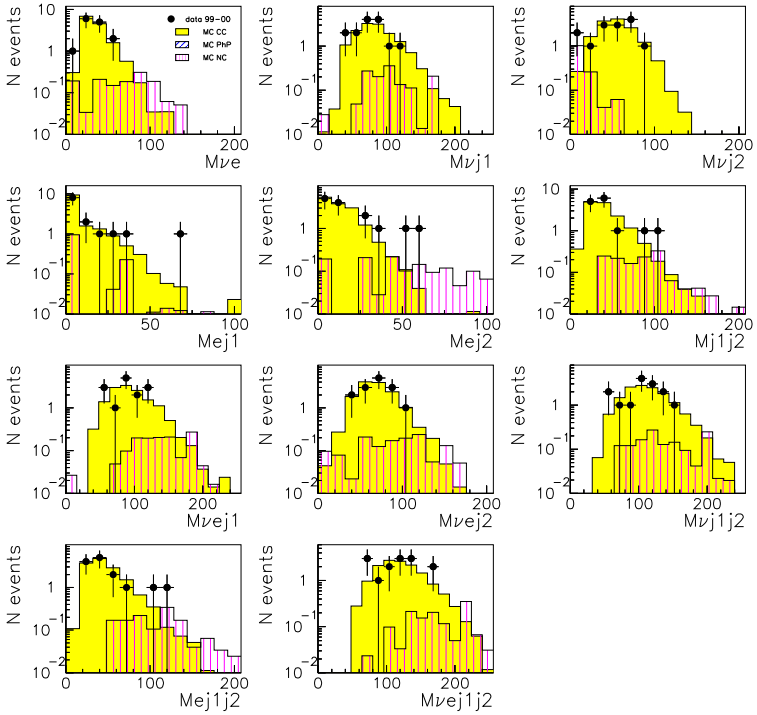

Figure 10.4: All possible combinations of invariant mass spectra of the final state $\nu + e + j + j$. Symbols denote P_T^{mis} (ν), electron, first jet and second jet, respectively.

$\nu + e + e + j$

In the event class $P_T^{mis} + e + e + j$, 13 events are observed, whilst 11.4 are expected from the Standard Model. The data points are in good agreement with the Standard Model Monte Carlo (Fig. 10.5). Neutral current events are the principle background to the event class. One event with invariant mass of $M_{\nu e1} \sim 170$ GeV is observed, whilst 1.4 events are expected with $M_{\nu e1} > 60$ GeV and 0.2 events are expected with $M_{\nu e1} > 100$ GeV (upper left plot in Fig. 10.5). The data event, which also contributed to the event class $\nu + e + j + j$ mentioned above, is displayed in Fig. C.7.

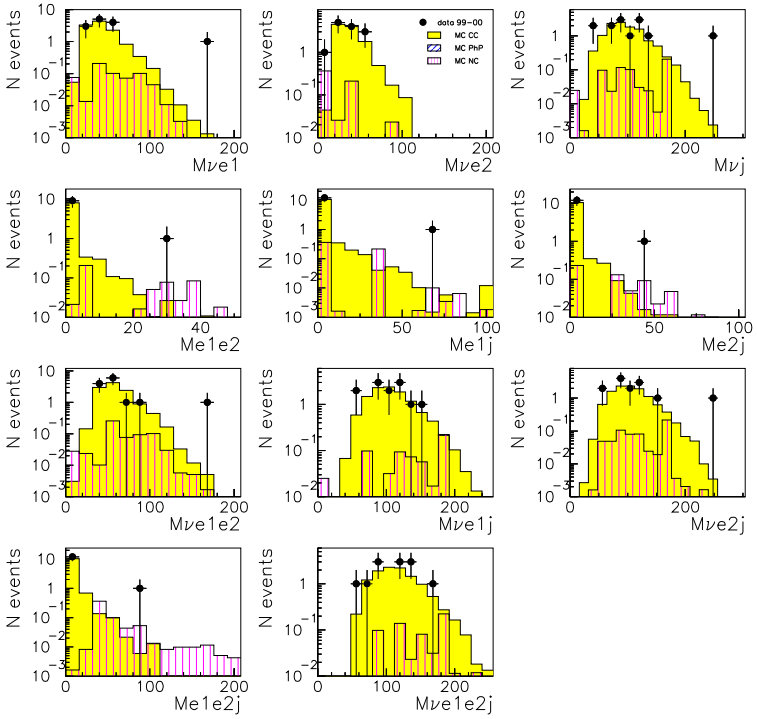

Figure 10.5: All possible combinations of invariant mass spectra of the final state $\nu + e + e + j$. Symbols denote P_T^{mis} (ν), first electron, second electron and jet, respectively.

$\nu + e + e + e$

One event is observed in events with missing transverse momentum and 3 electrons in the final state, whilst 0.7 are expected from the Standard Model (Fig. 10.6). The event is identical to the one mentioned above and is shown in Fig. C.7. Neutral current DIS backgrounds are the dominant background to this event topology. All invariant masses are below ~ 120 GeV.

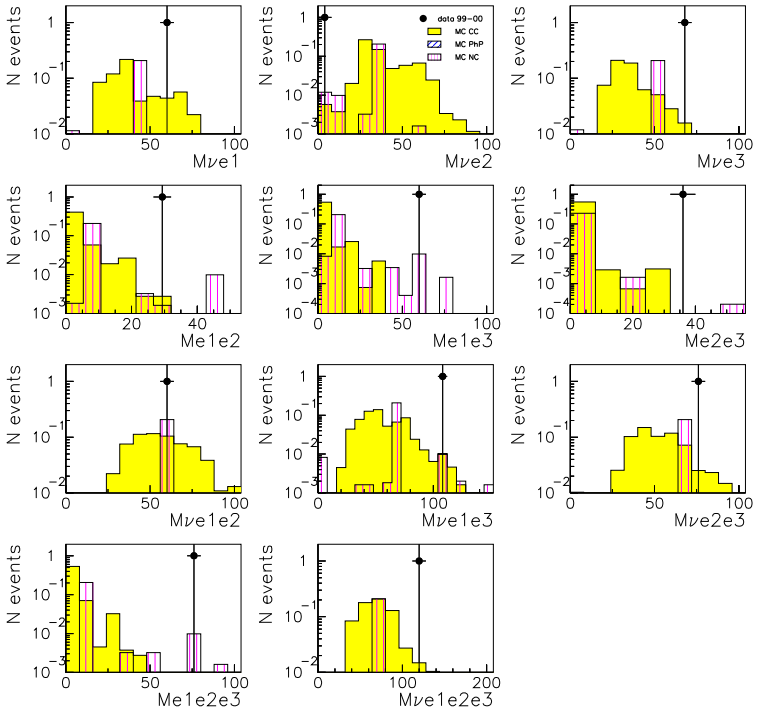

Figure 10.6: All possible combinations of invariant mass spectra of the final state $\nu + e + e + e$. Symbols denote P_T^{mis} (ν), first electron, second electron and third electron, respectively.

$\nu + j + j + j$

Good agreement between data and Monte Carlo is observed in the event class with P_T^{mis} and 3 jets in the final state where 4 events are observed, whilst 5.1 are expected from the Standard Model. Photoproduction DIS background is the dominant background to this event class. All masses are below 210 GeV.

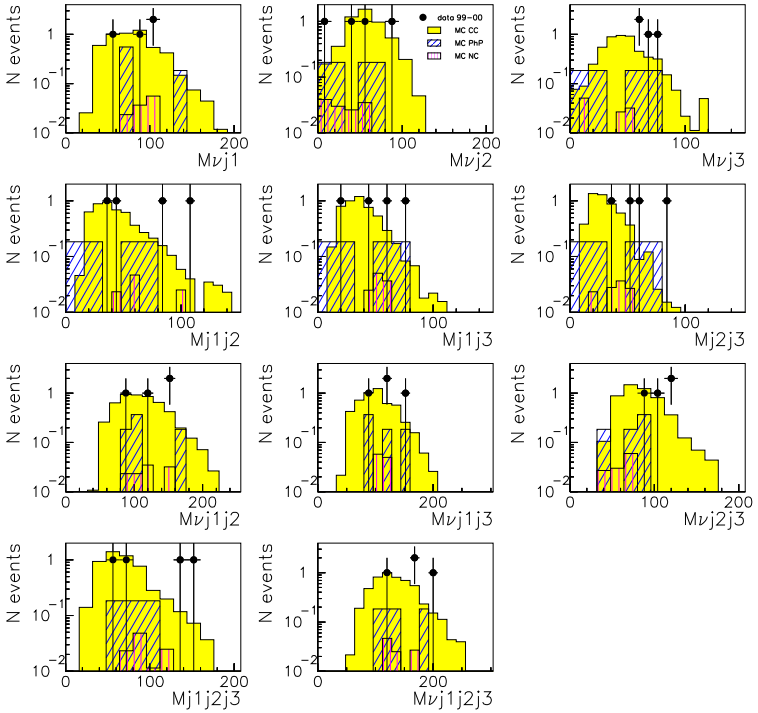

Figure 10.7: All possible combinations of invariant mass spectra of the final state $\nu + j + j + j$. Symbols denote P_T^{mis} (ν), first, second and third jet, respectively.

$\nu + e + e + j + j$

One event is observed in the event class $\nu + e + e + j + j$, whilst 1.7 Standard Model events are expected. All invariant masses are below 200 GeV.

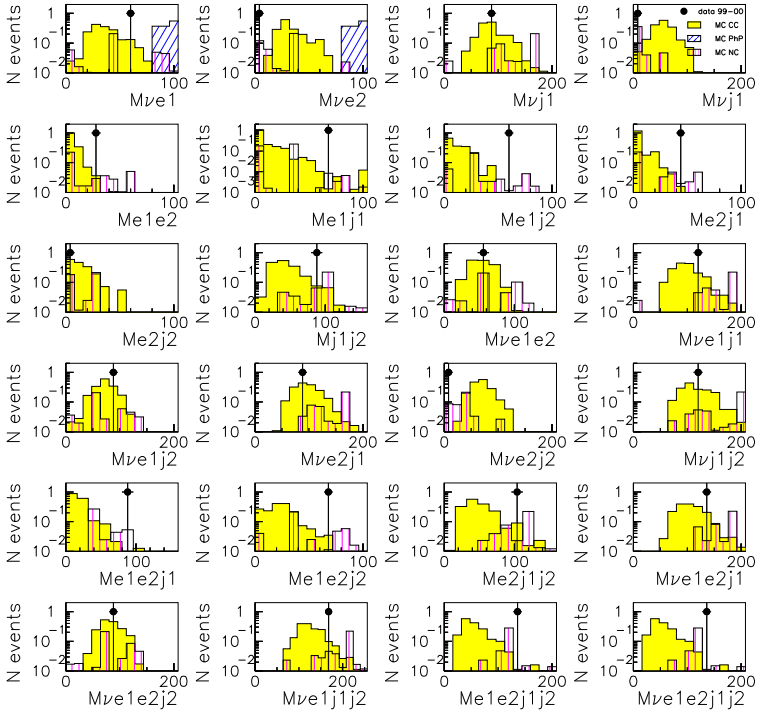

Figure 10.8: All possible combinations of invariant mass spectra of the final state $\nu + e + e + j + j$. Symbols denote P_T^{mis} (ν), first electron, second electron, first jet and second jet, respectively.

$\nu + e + j + j + j$

Good agreement between data and Standard Model Monte Carlo is observed in the final state topology $\nu + e + j + j + j$. One event is observed and 1.0 events are expected from the Standard Model. All invariant masses are below 200 GeV.

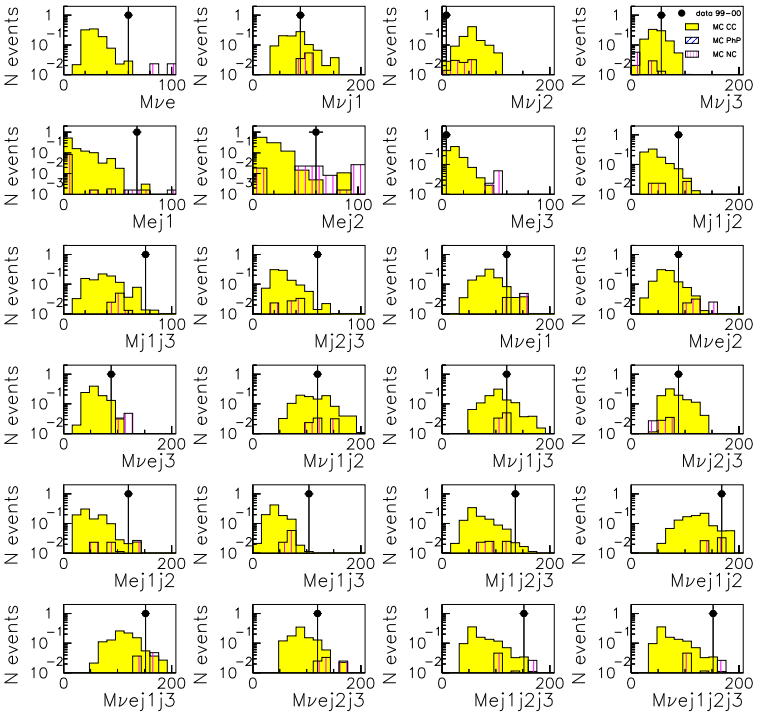

Figure 10.9: All possible combinations of invariant mass spectra of the final state $\nu + e + j + j + j$. Symbols denote P_T^{mis} (ν), electron, first jet, second jet, third jet, respectively.

Chapter 11

HERA-II Operation

The results presented in this thesis are derived from datasets collected by ZEUS during the last two years of HERA-I operation. During the $2001-2002$ shutdown an ambitious upgrade program was completed which enhanced physics capabilities by

- producing a $5-7$ total increase in the instantaneous luminosity, through the use of additional beam focussing magnets closer to the IP, and
- allowing rotation of the electron beam's transverse polarization into longitudinal polarisation at the IP, via spin rotator magnets.

Unfortunately HERA-II operation, which began in 2002, proved extremely difficult for both ZEUS and H1 due to large background rates from synchrotron radiation, beam gas and off momentum particles entering the detectors. An additional three month shutdown, in spring of 2003, corrected these problems by modifications of the collimation system which, in conjunction with improved vacuums, have allowed both experiments to take data efficiently.

An initial analysis of 1 pb^{-1} of pre 2003 shutdown e^+p HERA-II data has been performed, whereby additional visual scanning was necessary to remove the increased number of background events, which shows that the HERA-I and -II e^+p data sets have comparable properties, notably:

- The number of charged current events per 1 pb^{-1} are 15.0 ± 3.8 and 18.4 ± 0.5 for HERA-II and -I, respectively.
- The distributions for γ_h and $E-P_z$ of the hadronic system for two different gamma regions are shown in Fig. 11.1.
- The expected shift in vertex position from HERA-I to HERA-II are well understood (Fig. 11.2).

- The P_T distribution of the hadronic system and Q^2_{JB}, X_{JB} and Y_{JB} distributions, see Fig. 11.3 and Fig. 11.4, respectively, agree well.

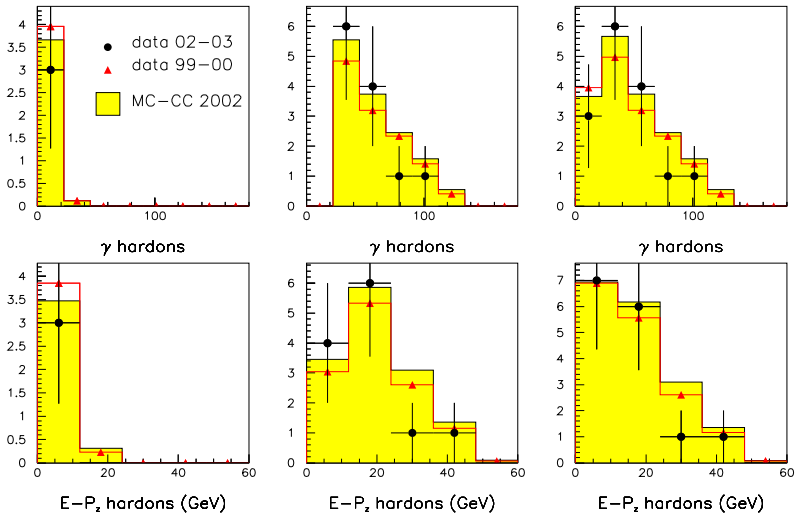

Figure 11.1: The distribution of γ_h and $E - P_z$ of the hadronic system for 2002 data, for 99-00 data and charged current Monte Carlo for all data (right), for high γ_h events (middle) and for low γ_h events (left).

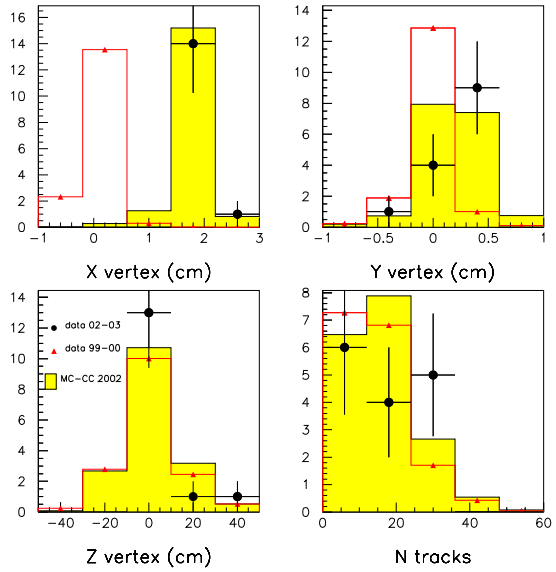

Figure 11.2: The distribution of vertex position and number of tracks compared to MC for 2003 and 99-00 e^+p data sets.

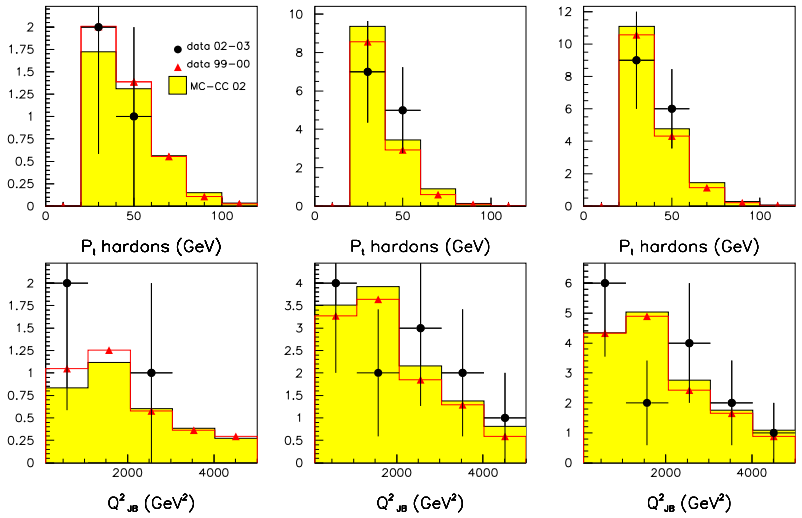

Figure 11.3: The distribution of P_T of the hadronic system and Q^2_{JB} for 2002 and 99 − 00 e^+p data compared to charged current Monte Carlo for all data samples (right), for high γ_h events (middle) and for low γ_h events (left).

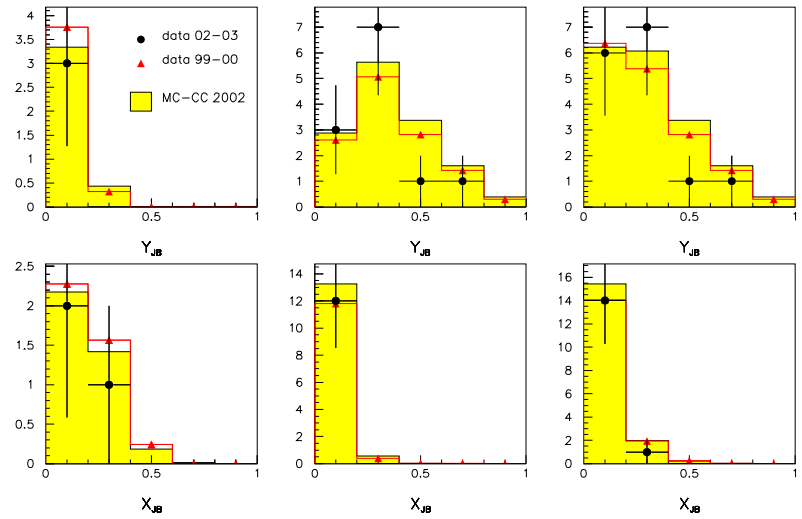

Figure 11.4: The distribution of X_{JB} and Y_{JB} for 2002 and 99 − 00 e^+p data compared to charged current Monte Carlo for all data samples (right), for high γ_h events (middle) and for low γ_h events (left).

Chapter 12

Conclusion

This thesis has presented a search for leptoquark resonant states that decay to (anti)neutrino and a quark. Data from 16.7 pb^{-1} of $e-p$ collisions and 65.0 pb^{-1} of $e+p$ collisions at center-of-mass energy of 318 GeV collected by the ZEUS detector at HERA were analyzed.

Two different techniques were applied to select leptoquark events. One is the standard charged current selection using cuts on event properties. The second one uses Artificial Neural Network technologies which leads to a 10% increase in signal efficiency while at the same time the background from Standard Model processes is significantly reduced. No signal is observed and event properties, including the mass spectrum, are in good agreement with the Standard Model. Limits have been placed on the leptoquark production cross-section and coupling constant using the narrow width approximation method and a two-dimensional likelihood analysis. The later was also used to place limits on the coupling strengths of Buchmüller -Rückl-Wyler leptoquarks with masses beyond the HERA center-of-mass energy.

The data collected by the ZEUS experiment during the years $99-00$ has been examined for deviations from the Standard Model prediction for events with large missing transverse momentum in the final state. All possible event topologies with P_T^{mis}, several electrons and/or jets have been investigated. Good agreement between data and Standard Model expectation has been found in all channels.

After the HERA upgrade in 2002 $\sim 15\ pb^{-1}$ of data was collected. The first picobarn of new data has been investigated and is in a good agreement with Monte Carlo predictions.

A number of new detectors were installed into ZEUS during the $2000-2001$ HERA upgrade shutdown. One of these, the C5 detector, is used to monitor and veto beam related background events. The C5 detector and the authors contribution to its development have been described.

The prospects for discoveries at HERA continue to improve as the luminosity delivered by the HERA accelerator continues to increase. The goal is to collect 1000 pb^{-1} of

integrated luminosity, thereby enhancing the sensitivity for the search for leptoquarks, excited leptons, squarks and other exotic processes, before HERA operation ends in 2007.

Appendix A

C5 DAQ

A.1 Position of C5 detector

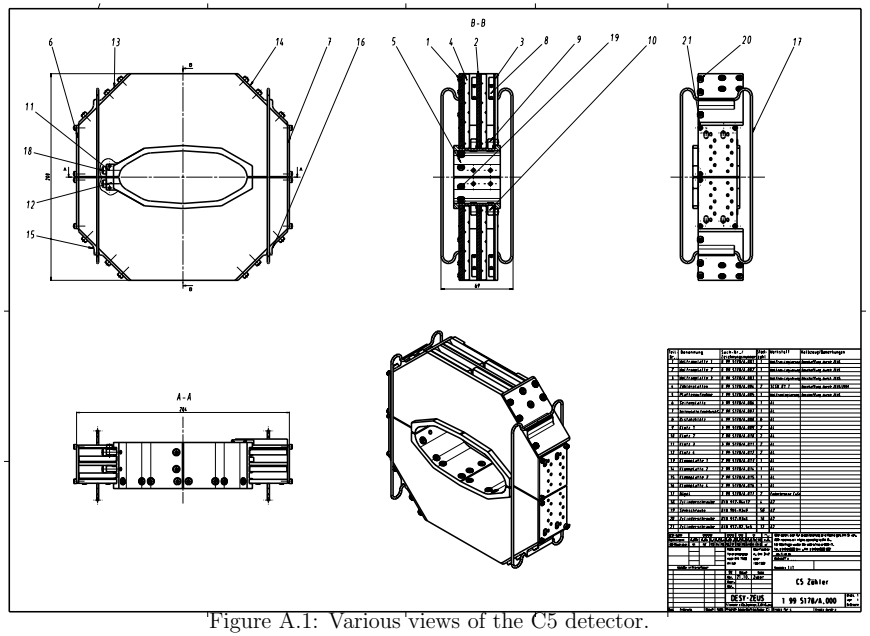

Figure A.1: Various views of the C5 detector.

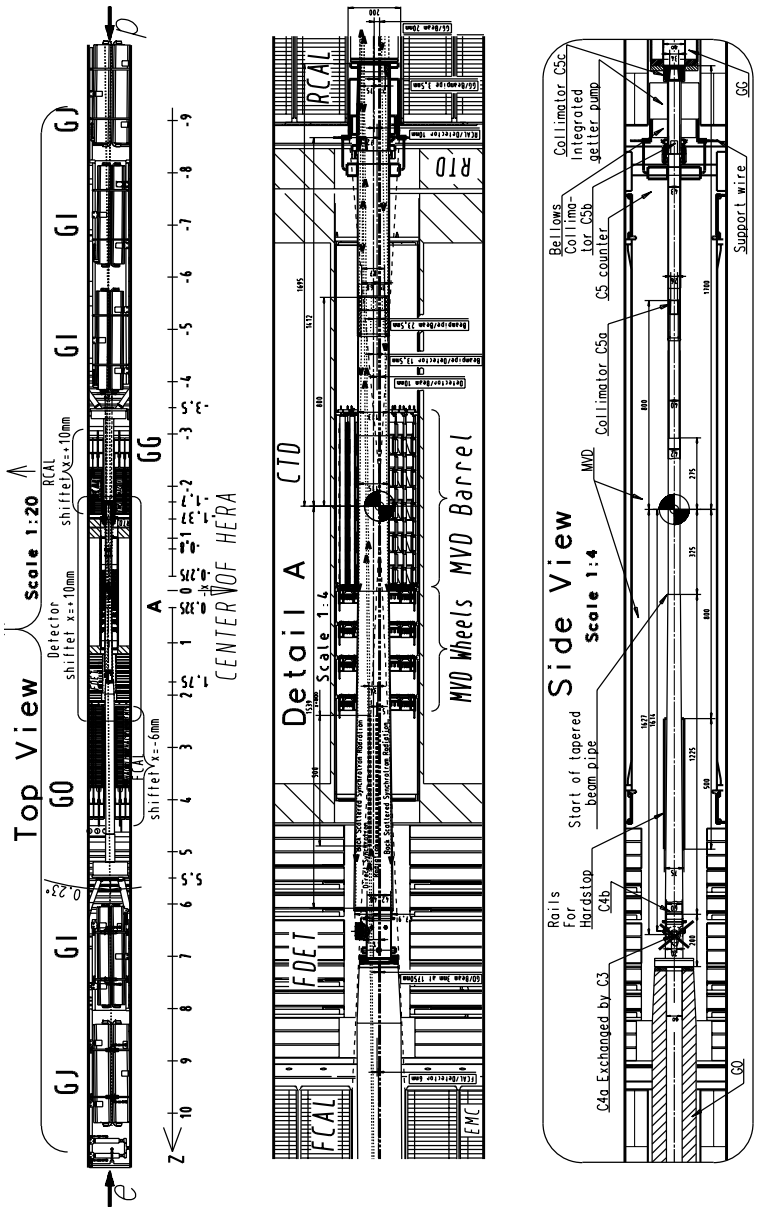

Figure A.2: Configuration of the beamline region in the ZEUS detector. The new position of the C5 detector is near the front face of RCAL.

A.2 C5: readout diagram

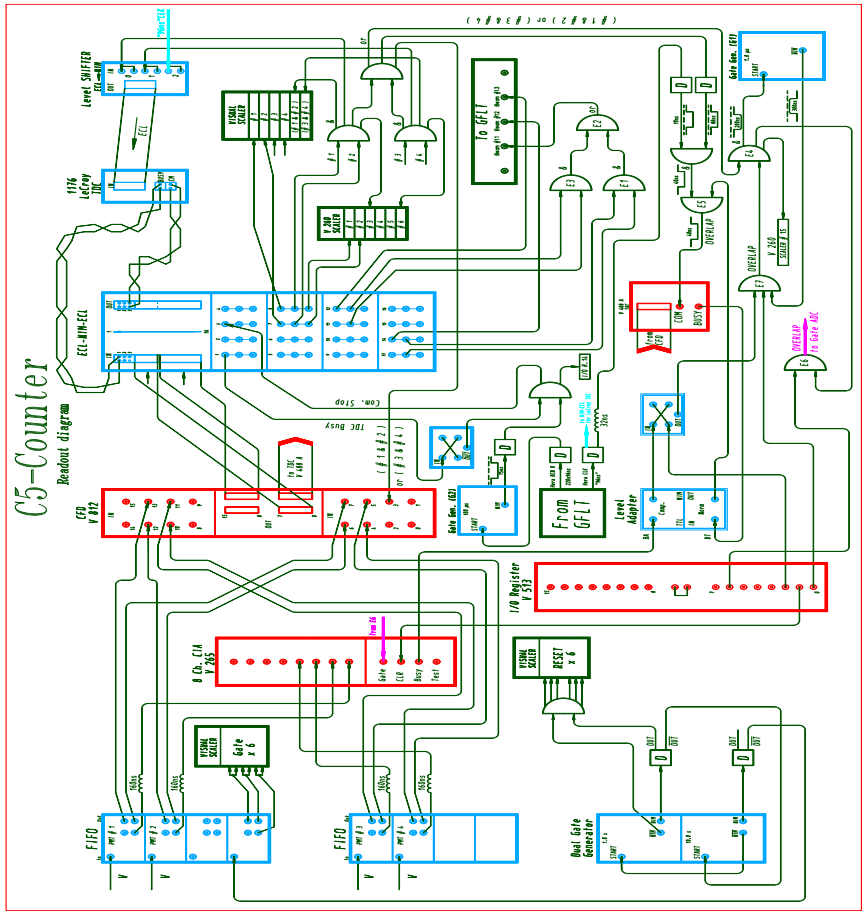

Figure A.3: Readout diagram.

A.3 Read out system

The C5 DAQ system occupies two racks (C-3-10 and C-3-11) in the ZEUS electronics rucksack. The rack contents are shown schematically in Fig. A.4.

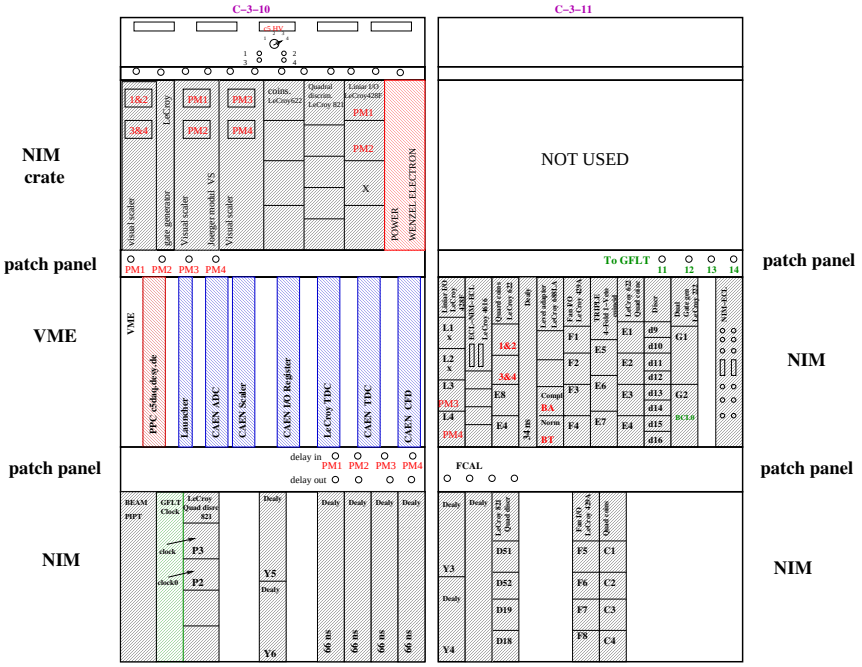

Figure A.4: Racks with C5 front-end and DAQ electronics.

A.3.1 VME single board computer

A Motorolla MVME 2600 PowerPC computer running LynxOS (Real Time system) is mounted in the VME crate (IP name *c5daq* and address 131.169.32.105)

A.3.2 VME modules

The VME crate accommodates the following readout modules:

- *Constant Fraction Discriminator(CFD C.A.E.N. V812),*
- *Scaler (C.A.E.N. V260),*
- *Input-Output Register (C.A.E.N. V513),*
- *Analog-to-Digital Converter (ADC C.A.E.N. V265),*
- *Time-to-Digital Converter (TDC C.A.E.N. V488),*
- *Time-to-Digital Converter (TDC LeCroy 1176).*

Constant Fraction Discriminator (CFD C.A.E.N. V812) has 16 NIM input channels and 16 differential ECL outputs with two fan-outs (Fig. A.5).
The CFD is designed to work with negative polarity input signal. Programmable threshold values can be set in a range from -5 mV to -255 mV with 1 mV step size. The channel thresholds are individually settable (see Table: A.1).

For GFLT the threshold is currently set to $-20\ mV$.

The output signal width is also programmable by software in a range from 15 ns to 250 ns as common for a group of 8 channels. The dead time is also common for a group of 8 channels and can be set between 150 ns and 2 μs.

The default value for the width is 40 ns and 157 ns for the dead time for all discriminator channels.

Table A.1: Discriminator thresholds.

Ch	Threshold	Description	Ch	Threshold	Description
0	x	not used	8	x	not used
1	x	not used	9	x	not used
2	-10 mV	HERA BCN0	10	-20 mV	GFLT PM4
3	-100 mV	HERA clock	11	-20 mV	GFLT PM3
4	-10 mV	PMT4	12	-20 mV	GFLT PM2
5	-10 mV	PMT3	13	-20 mV	GFLT PM1
6	-10 mV	PMT2	14	-10 mV	FCAL
7	-10 mV	PMT1	15	-10 mV	RCAL

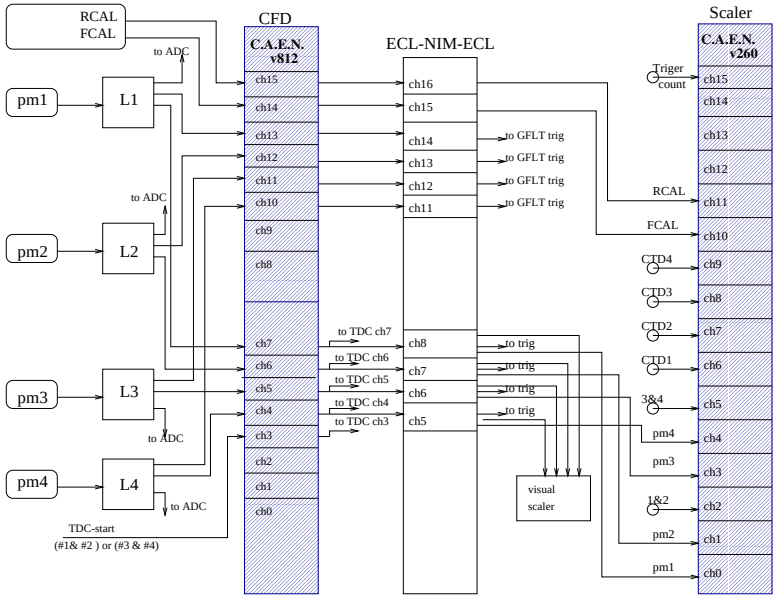

Figure A.5: Hardware setup.

Scaler(C.A.E.N. V260): has 16 independent 24-bit long counters (See: Fig. A.5 and Table A.2).

We are measuring a single rate from all C5 photo-multipliers and also a coincidence rate for pairs 1, 2 and 3, 4. In addition to the C5 rate information the data acquisition software is used for measurements of background rates from some other components, for example CAL, CTD. In the year 2003 new scintillator detectors were installed inside ZEUS for background and synchrotron radiation measurements. Rates from those scintillator detectors are also measured by the C5 system.
All scaler channels are read-out with 0.2 sec period ($\sim$ 5 Hz frequency).

Table A.2: Scaler inputs (see Fig. A.5).

Ch	Description
0	C5 PMT 1 [1]
1	C5 PMT 2 [1]
2	C5 coincidence of PMT 1 and PMT 2
3	C5 PMT 3 [1]
4	C5 PMT 4 [1]
5	C5 coincidence of PMT 3 and PMT 4
6	CTD1
7	CTD2
8	CTD3
9	CTD4
10	FCAL [1]
11	RCAL [1]
12	C5 electron beam gated rate
13	C5 proton beam gated rate
14	LeCroy TDC trigger rate
15 [2]	C.A.E.N. ADC and C.A.E.N. TDC Trigger rate

Analog-to-Digital Converter (ADC C.A.E.N. V265): has 8 charge-integrating ADC channels (See Fig. A.6 and Tab. A.3).

The FIFO memory can store up to 256×16 bit words. Two ADC dynamic ranges (120 pC and 800 pC) are selectable via software. The GATE width can be in the range from 100 ns to 5 μs and the input signal should be delayed for $\geq$ 65 ns after the gate's front.

The C5 ADCs are used with a dynamic range of 120 pC and a GATE width of 200 ns. All analog signals from photo-multipliers are delayed by $\sim$ 65 ns with respect to the GATE signal to fulfill the ADC requirement.

[1] Since Nov.2003 replaced by new scintillator (SR 3.6, SR 6.0, SR 8.0, SR 11.0, FSY 1 and 2, RSY 3 and 4 respectively)
[2] used by DAQ program

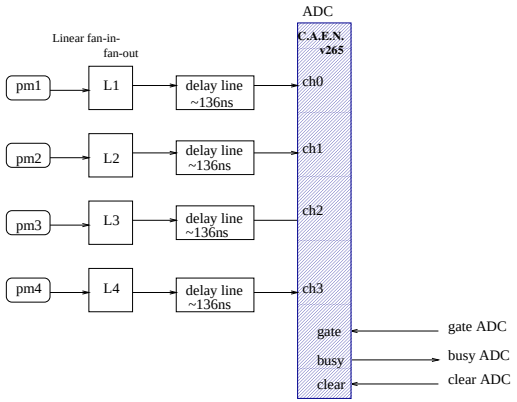

Figure A.6: Setup for ADC.

Table A.3: ADC inputs.

Channel	Description	Channel	Description
0	PMT1	4	not used
1	PMT2	5	not used
2	PMT3	6	not used
3	PMT4	7	not used

An example of ADC spectrum from one of the scintillator plates of C5 detector is shown in Fig. A.7.

Time-to-Digital Converter (TDC C.A.E.N. V488):

This module has 8 independent 12-bit Time to Digital Conversion channels (See Fig. A.8 and Tab. A.4). The Full Scale Time Range (common for all channels) is programmable from 90 ns to 770 ns, with resolution from 25 to 200 psec respectively. The output buffer is arranged as FIFO logic 512×16 bit.
The module is operating in Common STOP mode. As STOP signal the HERA 96 ns bunch clock is used and as START signal the signal from the coincidence of photomultipliers 1 and 2 (see Fig. A.9) is used. The time difference between the HERA 96 ns clock and the coincidence signal is measured in channel 3 of TDC.

Time-to-Digital Converter (TDC LeCroy 1176): This module has 16 independent 16-bit Multihit Time to Digital Conversion channels (See Fig. A.10 and Tab. A.5). The Full Scale is 65 μs with $1ns$ resolution (time bin). The digital data memory can store the

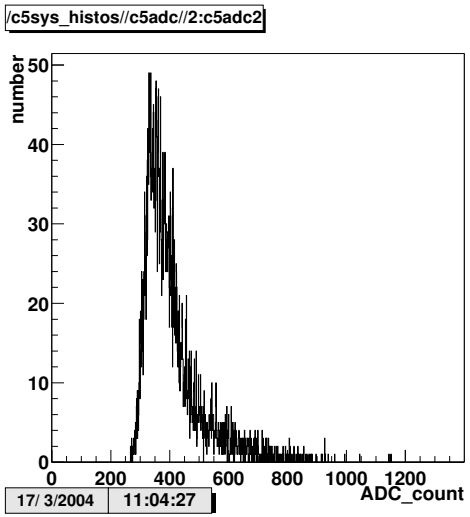

Figure A.7: ADC spectrum from one of the scintillator plates of C5 detector.

results of up to 32 events.

The module is operating in Common STOP mode. START signals are a coincidence of photo-multipliers 1 and 2 in TDC channel 0, and a coincidence of photo-multipliers 3 and 4 in channel 1. For STOP the HERA Bunch Crossing number 0 signal is used.
Defined parameters for the LeCroy TDC can be found in Table A.6. Note that the LeCroy TDC can measure the time of the leading and trailing edge of the input signal.

Input-Output Register (V513):
16 independent channels programmable as inputs or outputs are used to control and

Table A.4: TDC C.A.E.N. inputs.

Channel	Description	Channel	Description
0	not used	4	PMT4
1	not used	5	PMT3
2	not used	6	PMT2
3	coincidence signal of PMT1 and PMT2	7	PMT1

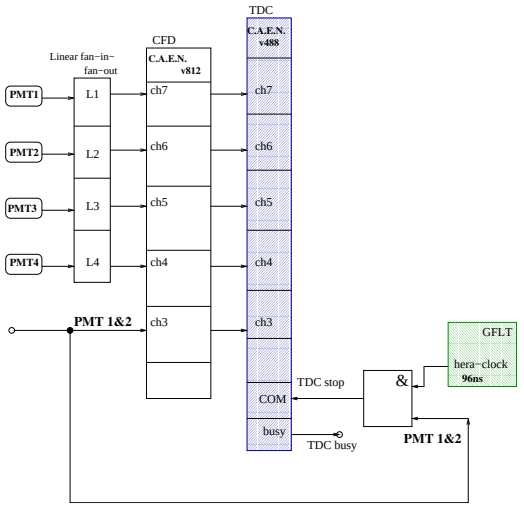

Figure A.8: C.A.E.N. TDC setup.

Table A.5: LeCroy TDC inputs.

Channel	Description
0	Coincidence of PMT 1 and PMT 2
1	Coincidence of PMT 3 and PMT 4

monitor the C5 DAQ hardware (See Fig. A.3). The channel 1 of the Input-Output Register is used to clear the ADC.

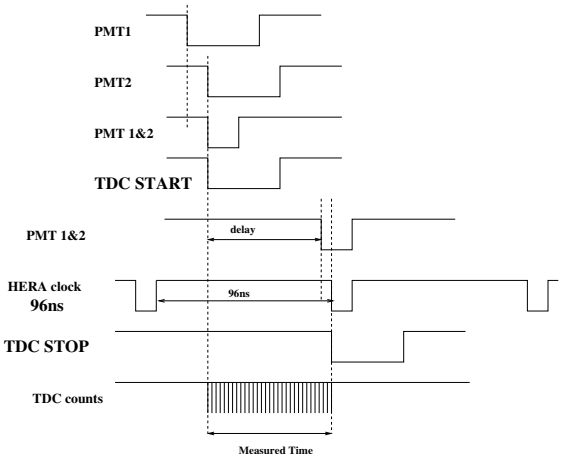

Figure A.9: Measurements of time using the C.A.E.N. TDC in C5 readout system.

Table A.6: Defined parameters for LeCroy TDC.

Parameter	Value	Description
CSR1	0x20	acquisition enable
CSR2	0x04	com-stop, leading + trailing edge, aux disable if (com-start) timeout: 1=1us, 2=2us, 3=4us, 4=8us
CSR2	0x24	com-stop, leading edge
CSR3	0x98	T-hit=500ns, 2-hit, 8=Odd, 4=Even, c=O+E

Table A.7: Input-Output Register.

Channel	Description	Mode
0	Enable trigger for ADC and CAEN TDC	output
1	Clear ADC	output
2	Busy ADC	input
3	Busy TDC	input
4	x	
5	Enable TDC trigger	output
6	Enable ADC trigger	output

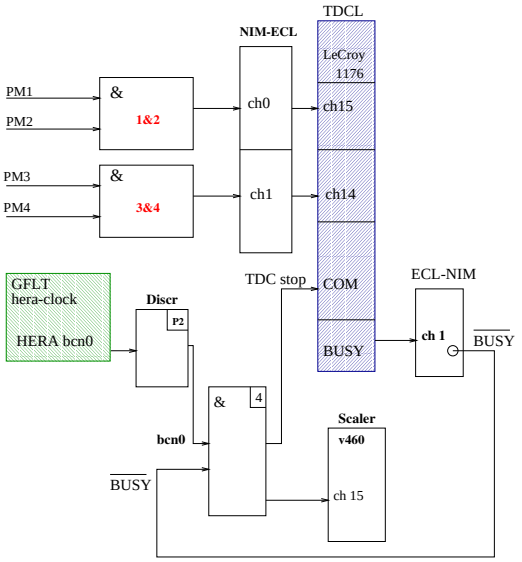

Figure A.10: LeCroy TDC setup.

A.3.3 DAQ configuration files and shared memory usage

The Data Acquisition Program for the C5 detector(*"run.exe"*) uses several configuration files. Note that the DAQ program can be run in *"background"* or *"interactive"* mode. In the *"background"* mode configuration files are read only at the start of the program. In *"interactive mode"* there is a possibility to reread the configuration files.

- "vme.conf" file gives the VME crate configuration (See Tab. A.8). Each line consists of a VME modules label, addressing mode (e.g. A24D16), the module VME address, and the space of the module inside the DATA space.
- "C5config.conf" file gives the configuration of the VME modules and the values which are used for operation of the DAQ program. Each line consist of a label and several parameters. In this way values for discriminator threshold, ADC dynamic range, TDC full scale range, time for rate update, settings for I/O register inputs, debug level and some other value are defined (See Tab. A.9).

  Parameters which are described in "C5config.conf" (see Tab. A.9) are stored also in shared memory $SMEM - ID$: 70002 on LynxOS/Power PC. These parameters used by the main C5 DAQ processes and can be overwritten during data taking. Using the program "DAQcontrol.exe" one can temporary change thresholds on the Constant Fraction Discriminator and reset current histograms without stopping data taking.

Table A.8: Configuration file "vme.conf".

```
#########################################################
#           VME crate configuration                     #
#                                                       #
# Name     VME Space       Address        Space       #
#                                                       #
#########################################################
  V812:      A24D16        0xFF010000     0x100
  V260:      A24D32        0x00020000     0x100
  ADC:       A24D16        0x00030000     0x100
  ADC2:      A24D16        0x00090000     0x100
  V513:      A24D16        0xFF040000     0x100
  TDCA:      A24D16        0xFF050000     0x100
  TDCL:      A24D32        0x00980000     0x100
#########################################################
```


Table A.9: Configuration file "C5config.conf".

```
#################################################################
#           Discriminator V812 Section                          #
#===============================================================#
#        Chan:  THR:   Comment
D_THRESH:  -1   20    # all channels; Thr=20mV;
D_THRESH:   4   20    # PM4; Thr=20mV;
D_THRESH:   1   10    # new det; Thr=30mV;
D_THRESH:   3   100   # 1&2-NIM;  Thr=100mV;
D_THRESH:  10   20    # GFLT PM4; Thr=20mV;
D_THRESH:  11   20    # GFLT PM3; Thr=20mV;
D_THRESH:  12   20    # GFLT PM2; Thr=20mV;
D_THRESH:  13   20    # GFLT PM1; Thr=20mV;
#===============================================================#
#        Chan:  WIDTH:   Comment                                #
#  width for two (0,1) section for channel (0-7) and (8-15)    #
D_WIDTH:  -1     200  # both section; pulse Width=64nsec;
#===============================================================#
#        Chan:  DTIME:   Comment                                #
#  dead time for two (0,1) section for channel (0-7) and (8-15)#
#D_DTIME:  -1    10   # both section; dead time=222ns;          #
D_DTIME:  -1     1    # both section; dead time=157ns;
#===============================================================#
#                ADC V265  Section                              #
#===============================================================#
ADC_RANGE:  0         # 0- low resolution, 1-high resolution
#===============================================================#
#                TDC V488  Section                              #
#===============================================================#
TDC_RANGE:  0xe0      # 0xe0 TDC_770ns; (for  TDC_90ns 0x0)
TDC_HTHR:   0xc0      # high threshold ( < 0xc7)
TDC_LTHR:   0x02      # low threshold
#===============================================================#
#                TDCL LeCroy 1176  Section                      #
#===============================================================#
#===============================================================#
#                 SCALER V260 Section                           #
#===============================================================#
RATE_UPDATE: 200000         # read rate every 0.2 second
#===============================================================#
#               IO/registre V513 Section                        #
#===============================================================#
#            Chan: Value:   Comment                             #
IO_REG_SETS:   0      1     # Enable Triggers
#                              (disable triggers val=0)        #
IO_REG_SETS:   5      1     # Enable Trigger for TDC
#                              (disable triggers val=0)        #
IO_REG_SETS:   6      1     # Enable Trigger for ADC
#                              (disable triggers val=0)        #
#===============================================================#
#               RUN Section                                     #
#===============================================================#
DEBUG_LEVEL:     0  # debug level
RESET_HIST:  10000  # recet histograms every 10,000 events
#################################################################
```

A.3.4 DAQ "background" and "interactive" operation modes

As was mentioned above the main Data Acquisition Programm *"run.exe"* can be started in *"background"* or *"interactive"* mode of operation. In *"background"* mode all parameters from configuration files are readout only once at the start. One can temporary overwrite default values of parameters, which are described in Tab. A.9, using the program *"DAQcontrol.exe"* during data taking. In *"interactive mode"* it is possible to control the DAQ program manually. First of all it is possible to start and stop reading from VME modules. Without stopping a run it is possible to plot and reset ADC and TDC histograms, initialize and clear all VME modules, change the ADC dynamic range and software debug level and a lot of other features useful for DAQ system testing and debugging.

If necessary, the DAQ program can be started by:

```
> run.exe & (‘‘background’’ mode )
or > run.exe -i (‘‘interactive’’ mode)
```

A CRON process running on VME/Power PC "c5daq.desy.de" checks the presence of the DAQ program "run.exe" every 5 minutes and restarts if necessary. To stop or to start the program manually in *"background"* mode one can login on "c5daq.desy.de" computer (user: c5) and use the following commands:
-cd STARTUP
-sh STOP.sh
-sh START.sh

A.3.5 How to recover after power failure

All NIM crates and VME crates which are shown in Fig. A.4 in racks C-3-10 and C-3-11 have to be switched on. The DAQ program "run.exe" will restart automatically in case of rebooting "c5daq.desy.de' computer .
All servers running on LinuxPC "zenc5.desy.de" (Tab. A.10) have to be started.

A.4 C5 data flow

Tab. A.10 shows the list of all servers which distribute C5 data to the clients (LUMI-display, gplotter, NETMEX, etc.) How to start C5 servers:
One can login on "zenc5.desy.de' computer (user: c5) and execute the startup scripts:
-cd STARTUP
-sh STOP.sh

-sh START.sh

Table A.10: Main processes which have to be started on zenc5.desy.de.

Process (server)	TCP port	User (client)	Description
c5daq-srv.exe	30005	LynxOS "run.exe"	Main DAQ server, collect all information from C5 DAQ programm in shared memory SHMEM-ID 3002
srv-hip.exe -p 3001	3001	gplotter and HIP	sends C5 rate information, ADC and C.A.E.N. TDC histograms; it also sends all LeCroy TDC histograms and rates from the second scaler
srv-lumi.exe -p 3002	3002	LUMI display	sends C5 rate information, ADC and C.A.E.N. TDC histograms
srv-netmex.exe -p 3004	3004	NETMEX	sends C5 rate information, ADC and C.A.E.N. TDC histograms
srv-hera.exe -p 3005	3005	HERA	sends C5 rate information, ADC and C.A.E.N. TDC histograms
srv-netmex.exe -p 3006	3006	ZEUSMEX	sends C5 rate information, ADC and C.A.E.N. TDC histograms; in addition sends rates from the second scaler
srv-netmex.exe -p 3007	3007	ZEUSMEX	sends C5 rate information, ADC and C.A.E.N. TDC histograms; in addition sends rates from the second scaler
srv-multiuser.exe -p 3003	3003	Other users	can accept multiple users connected to this port; sends C5 rate information, ADC and C.A.E.N. TDC histograms

A.5 Energy and current of HERA beam and HERA beam-pipe vacuum information

New process was implemented into the C5 system. It is called "*mexcln*" and it is running on LinuxPC (zenc5.desy.de). This process is a client of the NETMEX system and it receives information about current HERA parameters, for example electron and proton beam energy and current, beam-pipe vacuum information etc., and stores this information into the shared memory SHM-ID 6002 (0×00001772).

The information about e beam-pipe vacuum [1] from the right and left side of the interaction point are filled into the ZEUS run summary.

Information about HERA e and p beam energy and current and beam-pipe vacuum information (SR:HPR06.0, SR:HPR08.3, SL:HPL0.81, SL:HPL05.8) together with the corresponding C5 rate are stored for future investigation.

A.6 Useful programs

The program "*rate_c5.exe*" running on LinuxPC (zenc5.desy.de) reads rate information from the shared memory $SHMEM - ID$: 3002 and prints it on the terminal. The program updates the information on the terminal as soon as new data appear in the shared memory.

The program "*rate_3003.exe*" is similar to the process just mentioned above. But instead of reading data from the shared memory this process receives data from network (TCP/IP port 3003). This process can be started on any LinuxPC.

[1] in NETMEX vacuum information (VAC-E[185]-VAC-E[200]), where VAC-E[194],VAC-E[195],VAC-E[190],VAC-E[191] corresponds to SR:HPR06.0, SR:HPR08.3, SL:HPL0.81, SL:HPL05.8 respectively.

Appendix B

Control Plots for $e^{-}p$ Data

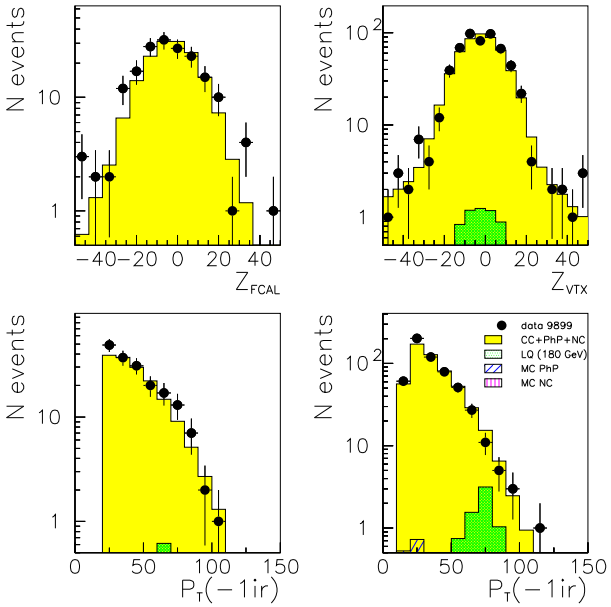

Figure B.1: The distribution of the $z-$ position of the vertex measured using FCAL timing (upper left plot) and Z-vertex measured by CTD tracking (upper right plot) for low and high gamma events respectively. $P_T[-1ir]$ distributions for low and high gamma events are shown in the lower left and lower right plots.

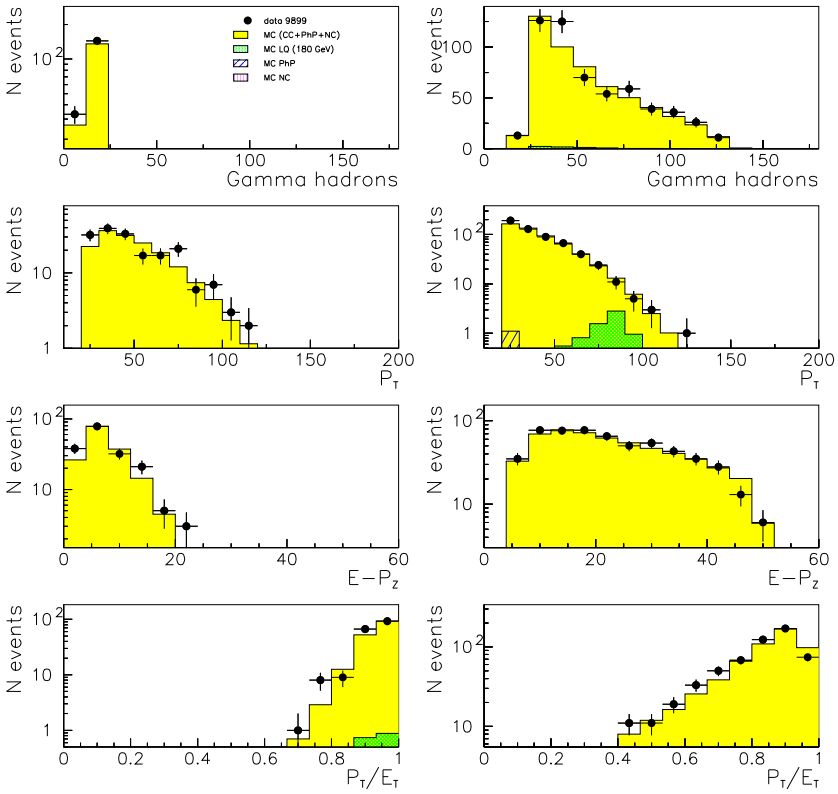

Figure B.2: γ^h, P_T^{mis}, $E-P_z$ and $\frac{P_T^{mis}}{E_T}$ for only low gamma events (left column) and only high gamma events (right column) for $e^{-}p$ data after all cuts are applied.

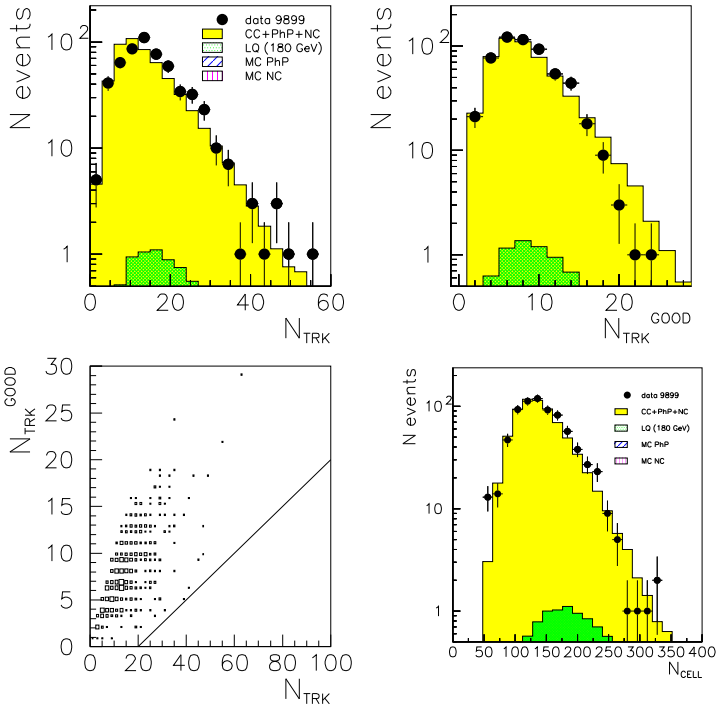

Figure B.3: Distributions of N_{trk} (upper left), N_{Good} (upper right) and N_{trk} vs N_{Good} (lower left), where N_{trk} is the total number of CTD tracks and N_{good} is the number of "good" CTD tracks. For these plots only high gamma events are selected. The N_{cells} distribution (lower right) for e^-p data and MC after all other cuts have been applied except the cut on $N_{cells} > 50$.

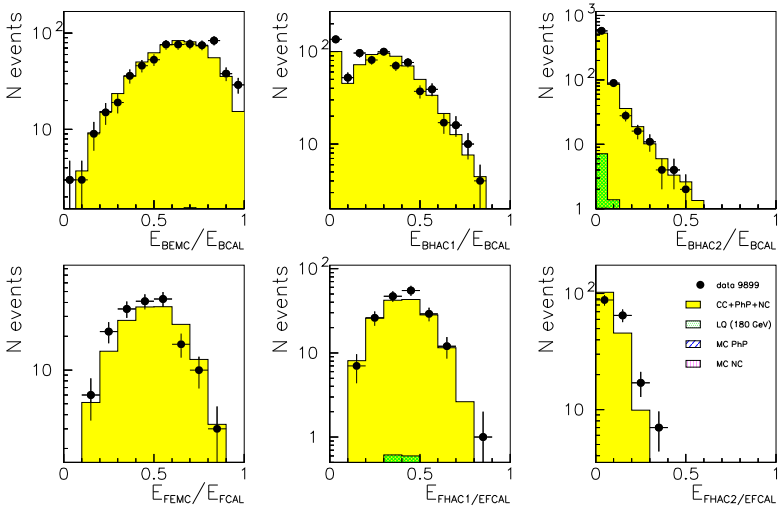

Figure B.4: The E_{Bemc}/E_{Bcal},E_{Bhac1}/E_{Bcal}, E_{Bhac2}/E_{Bcal} , E_{Femc}/E_{Fcal},E_{Fhac1}/E_{Fcal} and E_{Fhac2}/E_{Fcal} distributions for e^-p data and MC only for low gamma events after all cuts are applied.

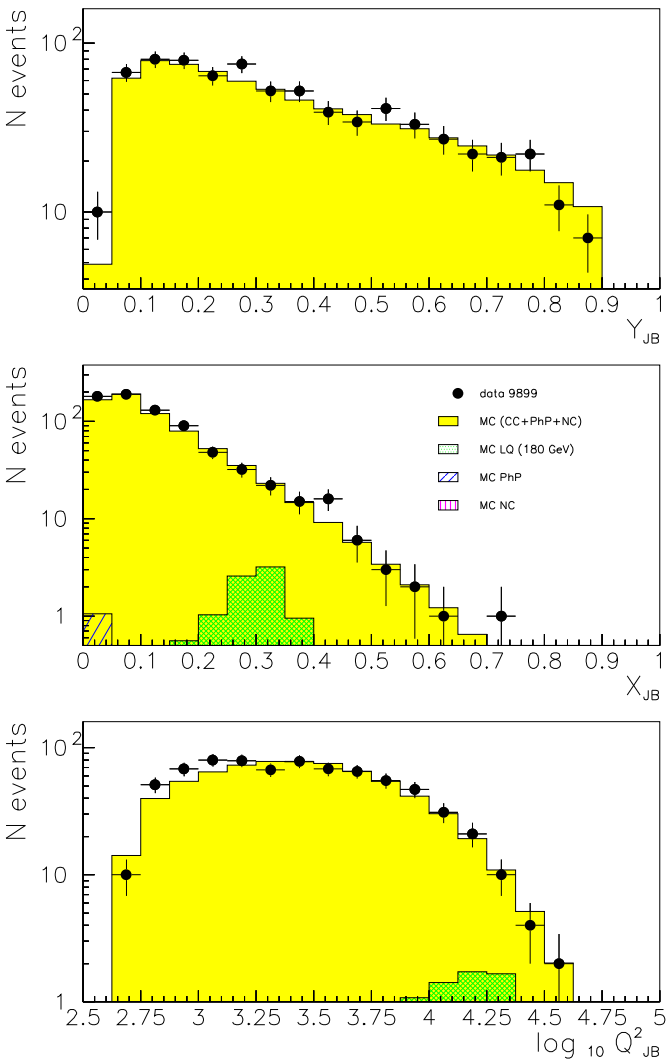

Figure B.5: The Y_{JB},X_{JB},$log_{10}(Q^2_{JB})$ distributions for e^-p data and Monte Carlo samples.

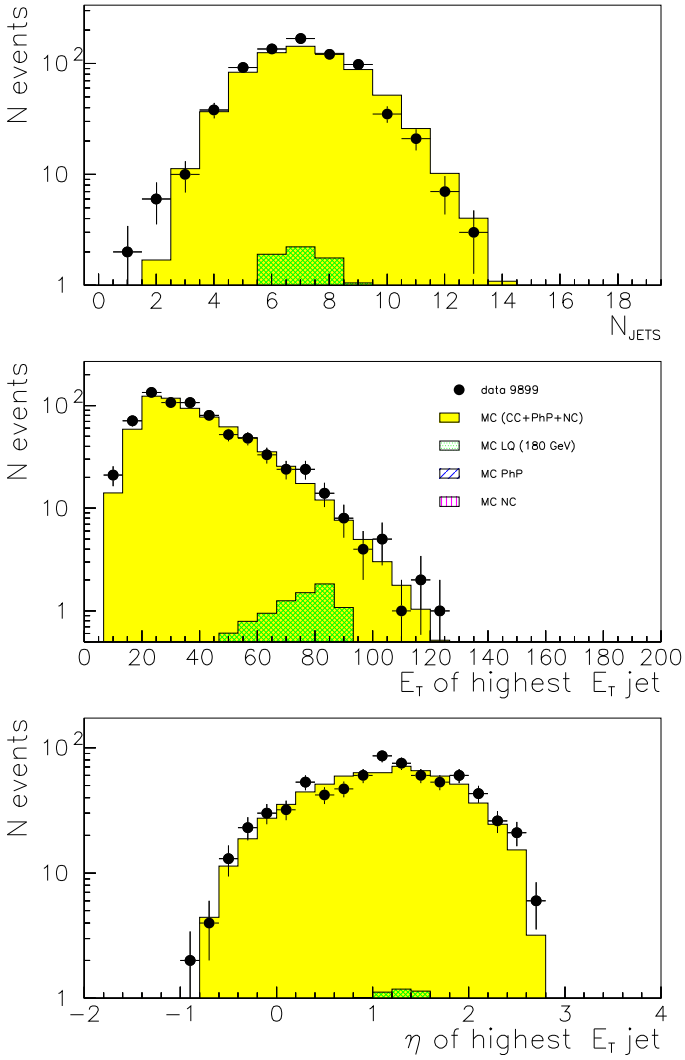

Figure B.6: Jet variables for only low gamma events (left column) and only high gamma events (right column) in e^-p data after all cuts are applied.

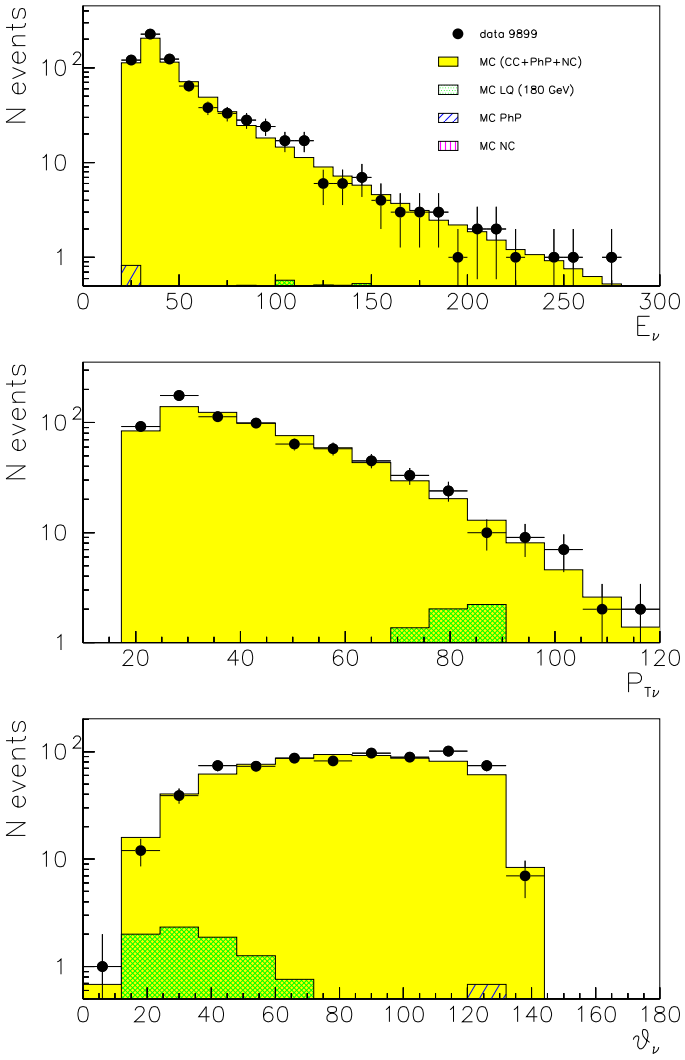

Figure B.7: Neutrino variables total energy E_ν, P_T^ν and θ_ν for selected events in e^-p data sample after all selection cuts are applied.

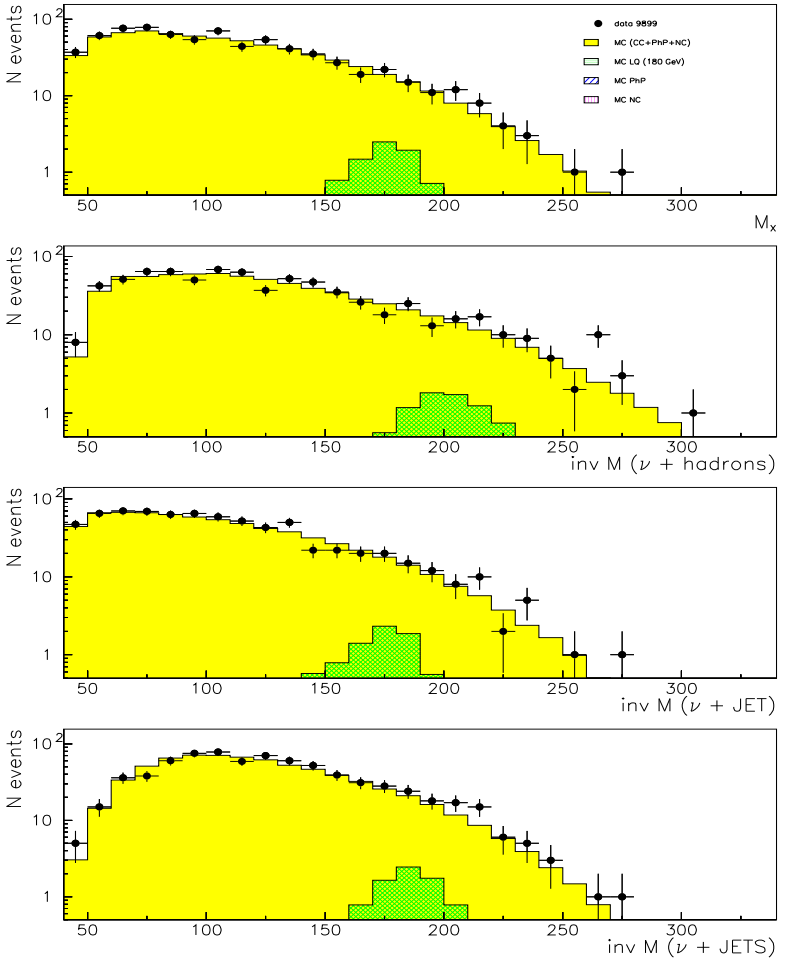

Figure B.8: Mass spectra for e^-p data for four different methods of mass reconstruction.

Appendix C

Event display

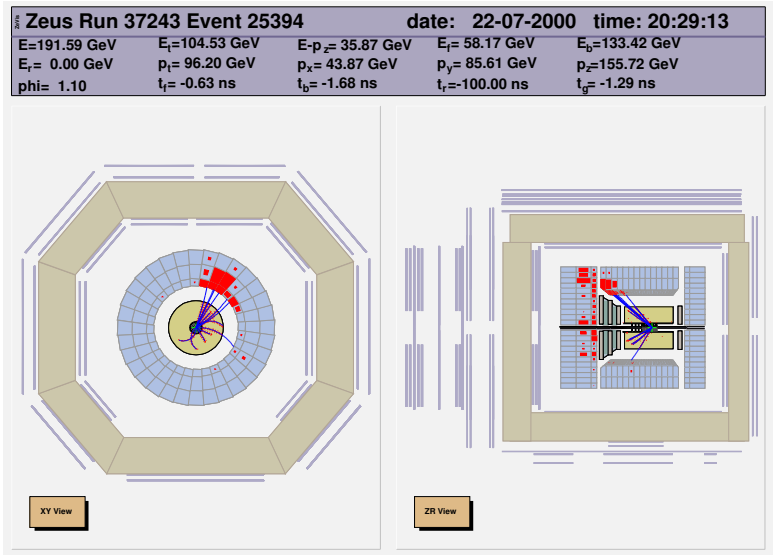

Figure C.1: One interesting event was found in e^+p data. This event has $Q^2 \sim 50166.5$ GeV^2 and $\cos\theta^* \sim -0.49$. The invariant mass of ν and jet gives the value $M_{\nu j} \sim 246$ GeV.

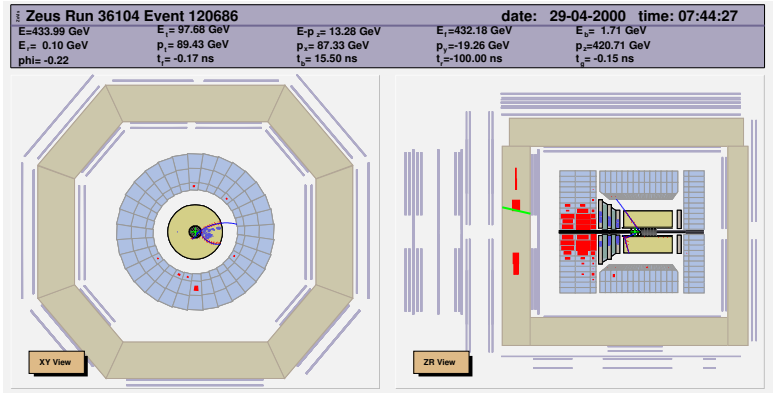

Figure C.2: This event found in e^+p data and has $M_{\nu j} > 250$ GeV ($Q^2 \sim 13500$ GeV^2 and $\cos\theta^* \sim 0.567$).

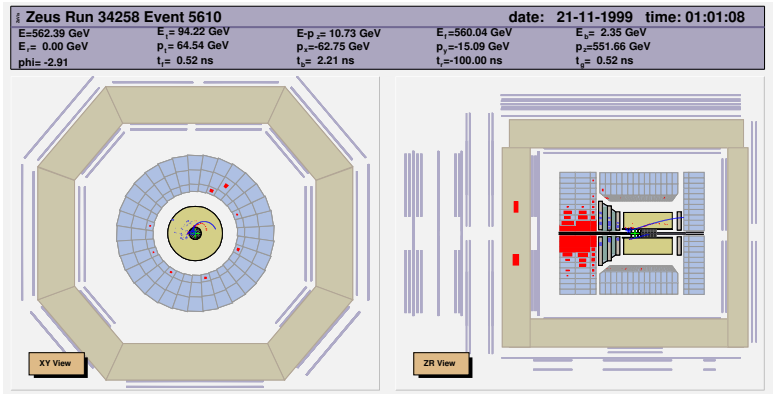

Figure C.3: A typical high-$M_{\nu j}$ event with $M_{\nu j} = 247$ GeV.

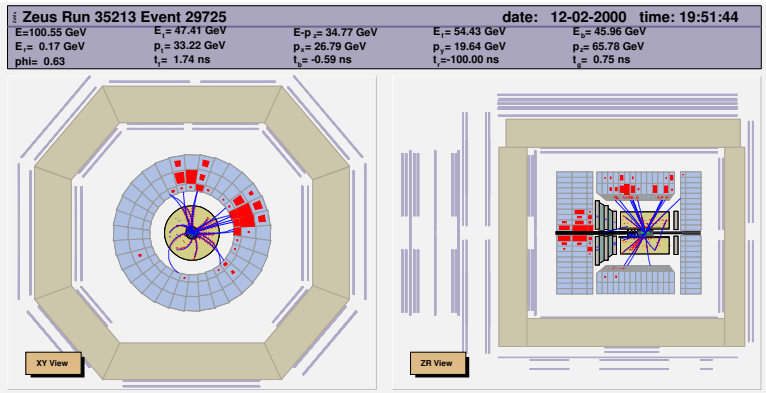

Figure C.4: Example of an event with P_T^{mis} + 3(4) jets in the final state.

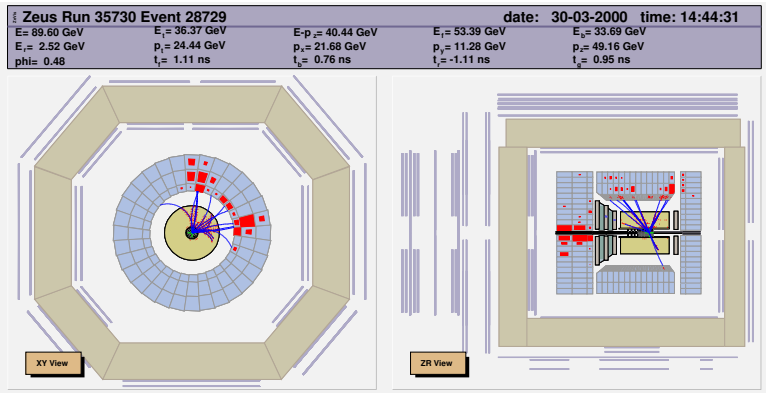

Figure C.5: Example of an event with P_T^{mis} + electron + two jets in the final state.

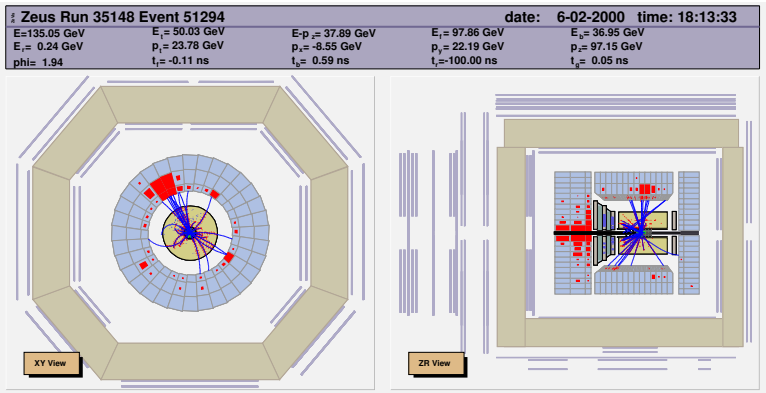

Figure C.6: Example of an event with P_T^{mis} + two electrons + jet in the final state.

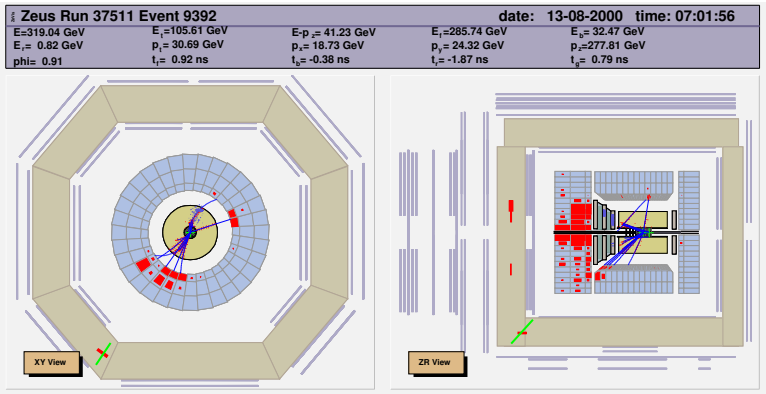

Figure C.7: High mass event selected with the signature $\nu + e + j + j$, $\nu + e + e + j$ or $\nu + e + e + e$.

Acknowledgements

This is the right place and time to thank everybody, who gave me help and support on my way.

I would like to thank Prof. Dr. Robert Klanner for making this thesis possible and for his continuous support.

I would like to thank my supervisor Prof. Dr. Peter Schleper for his continuous scientific advice and guidance during my work at the ZEUS experiment. His suggestions had an important role in my success. I would also like to thank him for his support and vivid interest for reading and correcting the draft.

I owe special thanks to Prof. Dr. Boris Dolgoshein. His advice and suggestions were very helpful when I was a student in Moscow Engineering and Physics Institute (MEPhI). I would like to thank him for giving me the opportunity to work within the HERA-B collaboration under his supervision where I worked for 5 years and for his continuous support during my work at the ZEUS collaboration.

The results presented here has been realized within the framework of the ZEUS experiment and could not been achieved without the combined efforts of the ZEUS collaboration members and many others.

I am most grateful to Dr. Wolfram Zeuner for his continuous support, great attention and trust in my work.

Many thanks to my colleagues at ZEUS especially the DESY group . I am very grateful to Dr. Uli Koetz, Dr. Uwe Schneekloth, Dr. Yuji Yamazaki, Dr. Christopher Youngman, Dr. Wladimir Hain, Dr. Alessandro Polini, Dr. J. Crittenden and Damir Lelas for their contributions, help and advice concerning C5 detector.

Many many thanks to Dr. Christopher Youngman for his valuable contribution in correcting the draft version of the thesis.

I also could not forget to thank my colleagues at Bonn, York and Toronto Universities. Special thanks to Prof. Dr. Sampa Bhadra for fruitful discussions.

I would like to thank my colleagues from Hamburg University and also the management of the University for organization of very helpful student seminars.

I also would like to thank the members of the ZEUS Exotic and Rare Phenomena Group for their help and suggestions. Many thanks to Dr. Elisabetta Gallo without whose warm support and help I could not have achieve my goal. Thanks to Dr. Katarzyna Klimek and Dr. Bruce Straub as coordinators of the Exotic Group for the friendly and productive working atmosphere in the group. I would like to thank Dr. Rainer Mankel for his advice concerning computing. Many thanks to Dr. Leonid Gladilin for advises and fruitful discussions. Thanks to Xiang Liu for his help and advice. I would especially like to thank Jola Sztuk for showing me various analysis techniques and for her great help.

Many thanks go to the High Energy Physics Department at the Moscow Engineering and Physics Institute (MEPhI) and the wonderful people I had work with: Dr. Sergey Smirnov, Dr. Anatoli Romaniouk, Dr. Valerij Sosnovtsev, Dr. Sergey Konovalov, Dr. Viktor Egorytchev, Alexei Antonov, Alexander Kaoukher, Sergey Semenov and Elena Andreeva. Special thanks to Alexei Stifoutkin for his experienced advice and help which were very helpful in the realization of this thesis.

And thanks to all people who have come or will come to my office to drink tea, for seeing the new update of our photo exhibition, for looking into the photo slides and for discussing problems.

Big thanks to my parents for their support and love over the many years of my education. I could not forget to thank all our family (Betcher, Mordueva, Frolova,.....), which is scattered around the world, for warm support and guidance, especially at difficult times. I truly wish all the best for all of you!!!

And finally a special thanks to my lovely husband Sergey Fourletov for his continuous support, for strategic advises and great help. He is always there when I need him most. I also to our 1 year old son Denis. He sleeps well at night and gave me the opportunity to finish this thesis. ;-)

Bibliography

[1] Perkins, Introduction to High Energy Physics.

[2] Quigg, Gauge Theories of the Strong, Weak, and Electromagnetic Interactions.

[3] http://pdg.lbl.gov/

[4] http://www-zeus.desy.de/physics/sfew/PUBLIC/sfew_results/preliminary/eps03/

[5] ZEUS Collaboration, Measurement of high-Q2 e-p Neutral Current Cross Sections at HERA and the Extraction of xF3, DESY 02-113

[6] PLUTO Collaboration, C. Berger et al, Nucl. Phys. **B 281**, 365 (1987)

[7] ZEUS Collaboration; The dependence of dijet production on photon virtuality in ep collisions at HERA. The European Physical Journal C,Vol. 35 No. 4 (July 2004), p. 487;DESY-04-053 (March 2004)

[8] ZEUS Collaboration; J. Breitweg et al, Phys. Lett. **B 479**, 37 (2000)

[9] H1 Collaboration; C. Adloff et al, Eur. Phys. J. **C 13**, 397 (2000)
H1 Collaboration, A. Aktas et al., Measurement of Dijet Production at Low Q^2 at HERA, Hep-ex/0401010

[10] Pati and Salam Unified Lepton-Hadron Symmetry and a Gauge Theory of the Basic Interactions, Phys. Rev. D 8, 1240-1251 (1973)
Pati and Salam, Lepton number as the fourth "color", Phys. Rev. D 10, 275-289 (1974)

[11] F. Halzen, A. Martin. Quarks and Leptons: An Introductory Course in Modern Particle Physics.

[12] W. Buchmüller, R. Rückl, D. Wyler, Leptoquarks in lepton-quark Collisions, Phys.Lett.B191:442,1987
W. Buchmüller, D. Wyler, Constraints on SU(5)-type leptoquarks, Phys.Lett.B177:377,1986

[13] A.Dobado, C Munoz. Production of Leptoquarks from superstring models in $e-p$ colliders. Physics Letters B191(87) 449.

[14] J. Wudka. Composite Leptoquarks. Phys.Lett. B167(86) 337;
B.Schrempp and F. Schrempp. Light Leptoquarks. Phys. Lett. B153(85) 101;

[15] S.Dimopoulos, L.Susskind. Mass without Scalars;
Review by K.Lane, lectures given at Theoretical Advanced Study Institute (TASI93) in Elem. Part.Physics, Boulder, CO, Jun 93, hep-ph/9401324.

[16] L. Hall, M. Suzuki. Explicit R-parity breaking in Supersymmetric Modeles.
N. Sakai T. Yanagida Proton Decay in a class of Supersymmetric Grand Unified Models. Nucl. Phys B197(82) 533-542.
R.Farrar, P.Fayet. Phenomenology of the Production, Decay, and Detection of new Hadronic States Associated with the Supersymmetry. Phys.Lett. B76(78)575.
P.Fayet Spontaneously broken Supersymmetric Theories of Weak, Electromagnetic and Strong Interactions. Phys.Lett B69(77)489.

[17] Xiang Liu, A search for resonance decays in e-jet in ep collisions at HERA , PhD thesis, Columbia, March 2003.

[18] The OPAL Collaboration. Search for Single Leptoquark and Squark Production in Electron-Photon Scattering at $\sqrt{s_{ee}}$ = 189 GeV at LEP.CERN-EP-2001-040;The European Physical Journal C Vol. 23 No. 1 (March 2002) p. 1

[19] D0 Collaboration, Search for Scalar Leptoquark Pairs Decaying to Electrons and Jets in pbarp Collisions, hep-ex/9707033,Phys. Rev. Lett. 79, 4321-4326 (1997)

[20] D0 Collaboration, Search for First Generation Scalar Leptoquark Pairs in ppbar Collisions at sqrt(s)=1.8 TeV, hep-ex/9710032, Phys. Rev. Letters 80, 2051 (1998).

[21] D0 Collaboration, Search for Leptoquark Pairs Decaying to neutrino neutrino + jets in p anti-p Collisions at s**(1/2)=1.8 TeV, hep-ex/0111047, Phys. Rev. Lett. 88, 191801 (2002)

[22] J. Ohnemus, S. Rudaz, T.F. Walsh, P.M. Zerwas, Single Leptoquark Production at Hadron Colliders, hep-ph/9406235, Phys.Lett. B334 (1994) 203-207

[23] Zeus Collaboration, Search for leptoquarks in ep collisions at HERA, hep-ex/0304008, Phys.Rev. D68 (2003) 052004
Zeus Collaboration, A search for resonance decays to antineutrino-jet in e^+p scattering at HERA, hep-ex/0009059, Phys.Rev. D63 (2001) 052002.

[24] H1 Collaboration, A Search for Leptoquark Bosons and Lepton Flavor Violation in Positron-Proton Collisions at HERA, hep-ex/9907002, Eur.Phys.J. C11 (1999) 447-471.

[25] D0 Collaboration, B. Abbott et al., Phys. Rev. Lett. 80 2051 (1998).

[26] OPAL Collaboration, Search for Leptoquarks in Electron-Photon Scattering at sqrt.(s_ee) up to 209 GeV at LEP, CERN-EP-2001-093, Phys. Lett. B526 (2002) 233-246.
OPAL Collaboration, G. Abbiendi et al., Eur. Phys. J. C6 1 (1999).

[27] C. Goy, Search for exotic physics at LEP,LAPP-EXP 2003-06
Straub, P. Bruce, Minireview of Leptoquark Searches, Amsterdam 2002, ICHEP* 792-795, hep-ex/0212023

[28] H1 Collaboration, C. Adloff et al., Observation of Events at Very High Q^2 in ep Collisions at HERA, Z. Phys. C74 (1997) 191

[29] ZEUS Collaboration, J. Breitweg et al., Z. Phys. C74 (1997) 207;
H1 Collaboration, C. Adloff et al, Z. Phys. C74 (1997) 191.

[30] D0 Collaboration, Search for New Physics in e mu X Data at D0 Using Sleuth: A Quasi-Model-Independent Search Strategy for New Physics, Phys.Rev. D62 (2000) 092004, hep-ex/0006011
D0 Collaboration, Search for New Physics Using Quaero: A General Interface to D0 Event Data, Phys.Rev.Lett. 87 (2001) 231801,hep-ex/0106039
D0 Collaboration, A Quasi-Model-Independent Search for New High p_T Physics at DZero, Phys.Rev.Lett. 86 (2001) 3712-3717, hep-ex/0011071

[31] H1 Collaboration,General Search for New Phenomena in ep scattering at HERA. EPS2003, July 2003, H1prelim- 03-063.

[32] ZEUS Collaboration, A Search for Excited Fermions in e^+p Collisions at HERA, DESY-97-112; Z.Phys.C76:631-646,1997; hep-ex/9708007

[33] Valerie A. Noyes, Search for new physics at HERA, hep-ex/9707037

[34] ZEUS Collaboration, Search for Selectron and Squark Production in e^+p Collisions at HERA, DESY-98-069, Phys.Lett.B434:214-230,1998

[35] H1 Collaboration, S. Aid et al., Z. Phys. C71 (1996) 211.

[36] Zeus Collaboration, The ZEUS Detector, Status Report 1993,DESY,1993.

[37] By ZEUS Luminosity Group (J. Andruszkow et al.), Luminosity Measurement in the ZEUS experiment, DESY-01-041, ZEUS-NOTE-01-004-REV, Mar 2001. 32pp

[38] S.M. Fisher, P. Palazzi, The ADAMO System Programmers Manual. CERN ECP and RAL.

[39] J.Cruttenden, W.Hain, U.Schneekloth, U.Wollmer, C.Youngman. The C5 Upgrade. ZEUS note 01-002.
W.Hain, U.Schneekloth, U.Wollmer, C.Youngman. The new C5 Counter Readout.ZEUS note

[40] ZEUS Background Working Group. Study of beam-induced backgrounds in the ZEUS detector from 2002 HERA running. ZEUS-02-018.
ZEUS Background Working Group. Study of beam-induced backgrounds in the ZEUS detector from 2002 HERA running. Addendum . ZEUS-02-020.
ZEUS Background Working Group. Study of beam-induced backgrounds in the ZEUS detector from 2002 HERA running. Addendum . ZEUS-02-027.

[41] R. Hall-Wilton, M. Sutton, Experience with the ZEUS Central Tracking Detector, Proceedings of IEEE NSS04 Conference, Rome(2004)

[42] http://www-mpy.desy.de/netmex/

[43] http://www-zeus.desy.de/components/offline/offline.html

[44] ZGANA, ZEUS trigger simulation library.

[45] GEANT3. R. Brun et. al., CERN DD/EE/84-1 (1987)

[46] H. Spiesberger, HERACLES and DJANGON. An Event Generator for ep Interactions at HERA Including Radiative Processes, http://www.desy.de/∼hspiesb/manual.ps.gz

[47] G. Ingelman , A. Edin , J. Rathsman , LEPTO 6.5 -A Monte Carlo Generator for Deep Inelastic Lepton-Nucleon Scattering, DESY 96-057

[48] L. Lönnblad, A program for simulation of QCD cascades implementing the colour dipole model, Comput. Phys. Commun. 71 (1992) 15, http://www.thep.lu.se/∼leif/ariadne/ariadne.ps.gz

[49] H. Spiesberger, A. Kwiatkowski and H.-J. Moehring, HERACLES. An Event Generator for ep Interactions at HERA Including Radiative Processes, http://www.desy.de/∼hspiesb/hsmanual.ps.gz

[50] Torbjörn Sjöstrand, Leif Lönnblad, Stephen Mrenna, Peter Skands, PYTHIA. Physics and Manual.hep-ph/0308153

[51] H. Plothow-Besch, PDFLIB Proton, Pion and Photon Parton Density Functions, Parton Density Functions of the Nucleus, and α_s Calculations. Users's Manual, CERN-ETT/TT W5051 PDFLIB 2000.04.17

[52] HERWIG 5.9; G. Marchesini et al., Computer Phys. Comm. 67 (1992) 465.

[53] J. Grosse-Knetter, Corrections for the Hadronic Final State, 1998.

[54] S. Catani, Yu.L. Dokshitzer, M.H. Seymour, and B.R. Webber. Longitudinally-Invariant $k_\perp$-Clustering Algorithms for Hadron-Hadron Collisions. Nucl. Phys. B406 (1993) 187.

[55] S.D. Ellis and D.E. Soper, Successive combination jet algorithm for hadron collisions. Phys. Rev. D 48 (1993) 3160.

[56] S.Bentvelsen, J.Engelen and P.Kooijman, Reconstruction of (x, Q2) and extraction of structure functions in neutral current scattering at HERA, in Proc. Workshop on Physics at HERA, Oct. 1991, eds. W. Buchm"uller and G. Ingelman, Vol. 1, p. 23. Hamburg, Germany, DESY, 1992.

[57] F. Jacquet and A. Blondel, Proceedings of the study for an *ep* facility for Europe, DESY 79-48 (1979) 391.

[58] J.G. Knetter, Zeus note 98-031.

[59] H.Bethe and W.Heitler, Proc.Roy.Soc.Lond.A146,83 (1934)

[60] G.Ross, Grand Unified Theories, Benjamin-Cummings Publishinf Co.(1995), London;A.D.Collins and E.J.Squires, Particle Physics and Cosmology, John Wiley and sons (1989) ????

[61] http://www-zeus.desy.de/ brummern/exotrig/exotrigger.html

[62] A. Kruse, A. v. Sighem, MUFFINCUP - A Wrapper for MUFFIN User Manual and Documentation, ZEUS note 98-025.

[63] Alex Tapper, Measurement of charged current deep inelastic scattering cross sections using the ZEUS detector at HERA, Ph.D. Thesis, Department of Physics, Imperial College London.

[64] Lpez-Durn Viani and S. Schlensted, Electron finder efficiencies and impurities. a comparison between SINISTRA95, EM and EMNET, ZEUS-Note 99-077.

[65] Zeus Collaboration, Measurement of high-Q2 charged current cross sections in e?p deep inelastic scattering at HERA, Phys. Lett. B539, 197 (2002).

[66] Wuyi Liu, Search for Resonances Decaying to e+jet and Limits on First Generation Leptoquarks in e^+p Interactions at HERA,

[67] Scott Sampson, A Search for Positron-Quark Resonances with Antineutrino Decays at HERA Using the ZEUS Detector, Ph.D. Thesis, Columbia University, 2000.

[68] G.V. Velev, Recent CDF and D0 run-I results, hep-ex/0205018

[69] Columbia University Group, Leptoquark Fits to ZEUS $94-97e^+$ and $98e^-$ Data. ZEUS-Note-00-003.

[70] http://neuralnets.web.cern.ch/NeuralNets/nnwInHep.html

[71] Christos Stergiou and Dimitrios Siganos, NEURAL NETWORKS. http://www.doc.ic.ac.uk/ nd/surprise_96/journal/vol4/cs11/report.html
John Conway, Separating Signal and Background - Optimally, http://www-cdf.fnal.gov/physics/statistics/recommendations/selection.html

[72] NNW In HEP References Subset: Reviews, Conference Proceedings:
http://neuralnets.web.cern.ch/NeuralNets/nnwInHepRef.html
http://neuralnets.web.cern.ch/NeuralNets/nnwInHepRefRev.html

[73] E.K. Blum and L.K.Li, Neural Networks 4, 511 (1991)

[74] D.W. Ruck *et al.,* IEEE Trans. Neural Networks 1, 296 (1990)

[75] C. Peterson, T. Rögnvaldsson and L. Lönnblad JETNET 3.0 – A Versatile Artificial Neural Network Package, LU TP 93-29 CERN-TH.7135/94, December 1993